Compressed Sensing on Terahertz Imaging

Thesis submitted in accordance with the
requirements of the University of Liverpool for the
degree of Doctor of Philosophy

by

Hao Shen

June 2012

Department of Electrical Engineering and Electronics

Abstract

Most terahertz (THz) time-domain (pulsed) imaging experiments that have been performed by raster scanning the object relative to a focused THz beam require minutes or even hours to acquire a complete image. This slow image acquisition is a major limiting factor for real-time applications. Other systems using focal plane detector arrays can acquire images in real-time, but they are too expensive or are limited by low sensitivity in the THz range. More importantly, such systems cannot provide spectroscopic information of the sample.

To develop faster and more efficient THz time-domain (pulsed) imaging systems, this research used random projection approach to reconstruct THz images from the synthetic and real-world THz data based on the concept of compressed/compressive sensing/sampling (CS). Compared with conventional THz time-domain (pulsed) imaging, no raster scanning of the object is required. The simulation results demonstrated that CS has great potential for real-time THz imaging systems because its use can dramatically reduce the number of measurements in such systems.

We then implemented two different CS-THz systems based on the random projection method. One is a compressive THz time-domain (pulsed) spectroscopic imaging system using a set of independent optimized masks. A single-point THz detector, together with a set of 40 optimized two-dimensional binary masks, was used to measure the THz waveforms transmitted through a sample. THz time- and frequency-domain images of the sample comprising 20×20 pixels were subsequently reconstructed. This demonstrated that both the spatial distribution and the spectral characteristics of a sample can be obtained by this means. Compared with conventional THz time-domain (pulsed) imaging, ten times fewer THz spectra need to be taken.

In order to further speed up the image acquisition and reconstruction process, another hardware implementation - a single rotating mask (i.e., the spinning disk) with random binary patterns - was utilized to spatially modulate a collimated THz. After propagating through the sample, the THz beam was measured using a single detector, and a THz image was subsequently reconstructed using the CS approach. This demonstrated that a 32×32 pixel image could be obtained from 160 to 240 measurements. This spinning disk configuration allows the use of an electric motor to rotate the spinning disk, thus enabling the experiment to be performed automatically and continuously. To the best of our knowledge, this is the first experimental implementation of a spinning disk configuration for high speed compressive image acquisition.

A three-dimensional (3D) joint reconstruction approach was developed to reconstruct THz images from random/incomplete subsets of THz data. Such a random sampling method provides a fast THz imaging acquisition and also simplifies the current THz imaging hardware implementation. The core idea is extended in image inpainting to the case of 3D data. Our main objective is to exploit both spatial and spectral/temporal information for recovering the missing samples. It has been shown that this approach has superiority over the case where the spectral/temporal images are treated independently. We first proposed to learn a spatio-spectral/temporal dictionary from a subset of available training data. Using this dictionary, the THz images can then be jointly recovered from an incomplete set of observations. The simulation results using the measured THz image data confirm that this 3D joint reconstruction approach also provides a significant improvement over the existing THz imaging methods.

Acknowledgments

This thesis could not be finished without the help and support of many people who are grateful acknowledged here. At a very first, I would like to express my deepest gratitude to my supervisor, Dr. Yaochun Shen. He has always given me valuable ideas, suggestions and comments with his profound knowledge and rich research experience and guided me in the right direction. He was easily available and accessible and willing to discuss whenever I needed his guidance and support. Then, I owe special thanks to Dr. Lu Gan and Dr. Vahid Abolghasemi for supporting part of this research. I could not accomplish my thesis without their kind support and valuable suggestions. I also would like to thank Prof. Yi Huang for supporting and guiding me in my research. I have learnt from them a lot not only about research, but also about the professional ethics.

In additional, I wish to extend my thanks to the Department of Electrical Engineering and Electronics for its support of this study. I would like to thank Mr. Alan Edwards for manufacturing the power supplier for BWO THz source. And I owe special thanks to Mr. Alan Roby, Mr. John Lynch and Miss Jill Anson of the core services for their help and guidance in making experimental equipments. Also, I would like to thank Prof. Peter Weightman and Mr. Paul Harrison, from Department of Physics, for providing the BWO THz source used in this work.

Thanks are also due to Engineering and Physical Sciences Research Council (EPSRC), UK Technology Strategy Board (TSB), and my university, for their support during this work. Part of my work were accomplished by their funding (EP/H02235X/1, EP/I038853/1, EP/E048811/1, and AB293H).

I would like to thank my postgraduate colleagues, who never failed to give me great encouragement and suggestions. Special thanks should go to Mr. Yue Dong, Mr. Lin

Liu and Miss Chen Li for their kindly supports and suggestions. I am also indebted to Mr. Lei Wang for his helps.

Last but not least, I would like to thank my family members, especially my wife, Lin Xu, and my parents. My wife has to live alone for such a long time when I was busy in doing research at University. This would not be possible without her encouragement. Without my parents' support during my whole research duration, I also could not be able to achieve my goals.

Table of Contents

List of Figures

List of Tables

List of Publications and Conference Presentations

Journal Paper:

[1] H. Shen, L. Gan, N. Newman, Y. Dong, C. Li, Y. Huang and Y. C. Shen, "Spinning disk for compressive imaging," *Opt. Lett.*, vol. 37, no. 1, pp. 46-48, 2012.

[2] S. C. Zhong, H. Shen, and Y. C. Shen, "Real-time monitoring of structural vibration using spectral-domain optical coherence tomography," *Optics and Lasers in Engineering*, vol. 49, no. 1, pp. 127-131, 2011.

[3] S. C. Zhong, Y. C. Shen, H. Shen, and Y. Huang, "FDTD study of a novel terahertz emitter with electrical field enhancement using surface Plasmon resonance," *Progress in Electromagnetics Research Symposium* (*PIERS) Online*, vol. 6, no. 2, pp. 153-156, 2010.

[4] Y. C. Shen, L. Gan, M. Stringer, A. Burnett, K. Tych, H. Shen, J. E. Cunningham, E. P. J. Parrott, J. A. Zeitler, L. F. Gladden, E. H. Linfield, and A. G. Davies, "Terahertz pulsed spectroscopic imaging using optimized binary masks," *Appl. Phys. Lett.*, vol. 95, no. 23, 231112, 2009.

Conference Presentations:

[5] H. Shen, V. Abolghasemi, L. Gan and Y. C. Shen, "Compressive three-dimensional (3D) terahertz imaging," *accepted by Institute of Physics' conference in optics and photonics, Photon12*, 2012.

[6] H. Shen, L. Gan, N. Newman, and Y. C. Shen, "Fast compressive terahertz imaging," *Signal Processing with Adaptive Sparse Structured Representations (SPARS)*, Edinburgh, Scotland, UK, 2011.

[7] H. Shen, N. Newman, L. Gan, S. C. Zhong, Y. Huang and Y. C. Shen, "Compressed terahertz imaging system using a spin disk," *35th IEEE International Conference on infrared, millimeter, and terahertz waves*, Rome, Italy, 2010.

[8] S. C. Zhong, Y. C. Shen, H. Shen, R. K. May, M. Evans, J. A. Zeitler, and I. Warr, "Near-Infrared Spectroscopy for Non-destructive coating analysis calibrated by terahertz pulsed imaging," *35th IEEE International Conference on Infrared, Millimeter, and Terahertz Waves*, Rome, Italy, 2010.

[9] H. Shen, N. Newman, L. Gan, S. C. Zhong, Y. Huang and Y. C. Shen, "Compressive Terahertz imaging system using single rotating mask," *3rd Annual Meeting on THz measurement techniques, Institute of Physics ISAT Group & Dielectrics Group*, London, UK, 2010.

[10] S. C. Zhong, H. shen, Y. C. Shen, J. A. Zeitler, L. Ho, M. Evans, P. T. Taday, M. Pepper, T. rades, K. C. Gordon, R. Muller and P. Kleinebudde, "Noninvasive 3D characterization of Layered samples using Terahertz pulsed imaging and infrared optical coherence tomography," *34th IEEE International Conference on Infrared, Millimeter, and Terahertz Waves*, Busan, Korea (South), 2009.

[11] S. C. Zhong, H. Shen, J. A. Zeitler, R. K. May, M. Evans, P. T. Taday, D. Dey and Y. C. Shen, "Non-destructive characterization of pharmaceutical tablet coating by terahertz and infrared spectroscopy and imaging," *American Association of Pharmaceutical Scientists Annual Meeting and Exposition (AAPS),* Los Angeles, USA, 2009.

Abbreviations

2D: two-dimensional
3D: three-dimensional
ADC: analog-to-digital converter
API: active pharmaceutical ingredient
AR(1): autoregressive model of order 1
ATR: attenuated total reflection
BS: beam splitter
BWO: backward wave oscillator
CCD: charge-coupled device
CMOS: complementary metal-oxide semiconductor
CS: compressed/compressive sensing/sampling
CW: continuous wave
DAQ: data acquisition
DCT: discrete cosine transform
DFG: difference-frequency generation
DMD: digital micro-mirror device
DSP: digital signal processing
EO: electro-optic
FEL: free electron laser
FET: field-effect transistor
FIR: far infrared
FOCUSS: focal underdetermined system solver
FRO: full random operator
FTIR: Fourier transform infrared
FWHM: full width at half maximum
KLT: Karhunen-Loeve transform
LED: light emitting diode
LTG: low-temperature-grown
MMSE: minimum mean square error
MMV: multiple measurement vector
MRI: magnetic resonance imaging
MSE: mean square error
NEP: noise equipment power
NM: number of measurements
NP: non-deterministic polynomial-time
NSP: null space property
OMP: orthogonal matching pursuit
PCA: photoconductive antenna
PCB: print circuit board
PD: photodiode
PM: parabolic mirror
PSNR: peak signal-to-noise ratio
QCL: quantum cascade laser
RGB: red-green-blue
RIP: restricted isometry property
RNG: random number generator
SDC: spinning disk configuration
SFG: sum-frequency generation
SMV: single measurement vector
SNR: signal-to-noise ratio
SOCP's: second order cone programs
SR: sampling rate
SVD: singular value decomposition
TDS: terahertz time-domain spectroscopy
THz: terahertz
TPI: terahertz time-domain (pulsed) imaging
TV-min: total-variation minimization

Chapter 1

Introduction

1.1 Motivation of the Work

As shown in Figure. 1.1, terahertz (THz) radiation refers to electromagnetic waves at frequencies in the THz range, which lie between the high-frequency edge of the microwave band and the long-wavelength edge of far-infrared light. Many crystalline substances possess sharp characteristic spectral features in this frequency range, which are associated with both inter- and intra-molecular vibrational modes [1, 2]. This, when coupled with the ability of THz radiation to propagate through common barrier materials, such as clothing and packaging, makes THz imaging and spectroscopy a potentially powerful tool for nondestructive determination of the chemical composition and physical structure of a concealed sample [3]. Indeed, over the past decade THz time-domain (pulsed) imaging has been demonstrated in applications areas as diverse as the medical diagnosis of human tissue, the detection and chemical mapping of illicit drugs and explosives, and pharmaceutical tablet inspection [4-7].

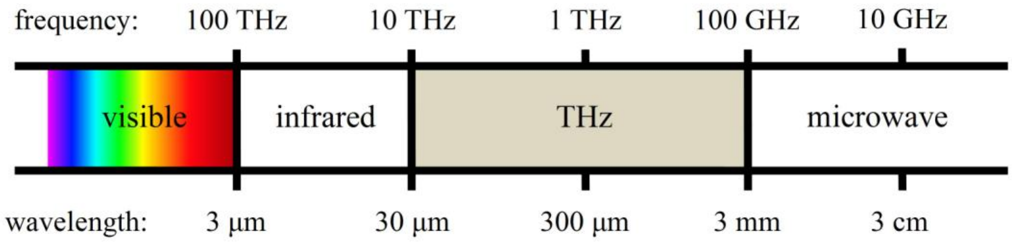

Figure. 1.1 The THz range of the spectrum lies between high-frequency edge of the microwave band and the long-wavelength edge of far-infrared light.

THz time-domain (pulsed) imaging (TPI) systems have been studied and developed rapidly since 1995. However, because of the relatively modest power levels available from the photoconductive sources commonly used in THz time-domain spectroscopy (THz-TDS) and imaging systems, and the lack of compact and sensitive multi-element THz detectors, most TPI experiments have been performed by raster scanning the object relative to a focused THz beam, and by using a single-point detector. Consequently, a complete image usually takes minutes or even hours to acquire, depending on the total number of pixels and the required spectral range/resolution. This is a major limiting factor for real-time applications such as in vivo medical and security imaging, or for on-line industrial process monitoring. Other approaches, such as those using focal plane detector arrays, single-shot electro-optic sensing using crossed polarizers and a charge-coupled device (CCD) camera, the Radon transform, and interferometric imaging [8-12], respectively, have certain limitations in speed, resolution or hardware requirement. Therefore, it is necessary to improve the current techniques to achieve a fast, cost-effective THz imaging system.

Fortunately, a novel theory in signal processing called compressed/compressive sensing/sampling (CS) [13, 14] has emerged over the past decade. An advantage of CS is to sense sparse signals by reducing the sampling rate and storage of acquisition devices. Recently Chan *et al.* [15, 16] reported a new THz imaging procedure, based on CS. The proposed CS-THz imaging system can solve problems such as no conventional CCD and complementary metal-oxide semiconductor (CMOS) imagers in the THz range and the slow data acquisition using the raster scanning approach. The free-space time-domain (pulsed) THz wave front travelling from an object to a single-point detector was spatially modulated by the insertion of a series of planar two-dimensional (2D) masks. Each mask comprised a random checkerboard pattern of 32×32 pixels which could each either transmit or block the THz radiation. By recording the THz field in the presence of each mask, a 2D image of the object was reconstructed [15]. This approach not only eliminates the need to raster scan the object or THz beam, but also reduces the number of measurements required [15]. This is a significant improvement in speed compared with the traditional raster scanning used for THz imaging (assuming that the masks can be changed automatically, for example, by using the newly developed THz spatial modulator [17]).

To date, current CS-THz systems still have much room for improvement. A major advantage of TPI is that the transient electric field, rather than the radiation intensity, is measured as a function of time. This coherent detection scheme not only yields a THz signal with excellent signal-to-noise ratio (SNR) and a high dynamic range, but also preserves the important phase information. Therefore, the first problem is that such a CS-THz system has not been proved to obtain the spectral information of the desired sample. Secondly, as each row of sensing matrix Φ is independent, the imaging speed is limited by the slow translation of one random pattern to another [18]. We noted that a THz spatial modulator could, in principle, be used for automatic CS-THz imaging [17]. However, this first generation THz spatial modulator has only 4×4 pixels, limiting its practical imaging applications. The second generation 32×32 pixels THz spatial modulator is still underdeveloped. Thirdly, a fully random binary operator incurs high computational complexity and huge memory, especially for high-resolution imaging [16]. For example, to get a 512×512 image with 64k measurements (i.e., 25% sampling rate), it requires several to tens of gigabytes of storage and giga-flop operations, which is unrealistic in practice.

The motivation for this research is to further improve the performance of current CS-THz systems. The aim is to achieve the following goals: firstly, to obtain both the spatial distribution and the spectral characteristics of a sample using the CS-THz system; secondly, to design specific sampling operators to minimize the sampling rate and the computational complexity; and thirdly, to achieve high speed compressive image acquisition.

1.2 Organization of the Thesis

Chapter 2 introduces the background of two main aspects of this work: THz imaging and CS. Section 2.1 discusses the sources and detectors of THz radiation, THz-TDS system, THz imaging and the corresponding applications. Following a brief introduction to CS, section 2.2 continues with a discussion of the sparse signal model. After this, the classical properties of sensing matrices and various constructions for structured CS matrices are reviewed. The chapter then focuses on the theory and algorithms for sparse recovery; and concludes with a discussion of some extensions of the sparse recovery framework.

Chapter 3 presents the simulation results for random projection on synthetic and real-world THz data. A linear random projection procedure will be demonstrated in this chapter. The minimum mean square error (MMSE) linear estimation was used as the reconstruction algorithm. The reconstructed THz images from both the synthetic and real-world THz data were subsequently acquired to obtain the desired image. Some key aspects of compressive THz imaging, including the effect of signal-to-noise ratio (SNR), the effect of number of measurements, and the limit of spatial resolution etc., were investigated and will be presented in this chapter.

Chapter 4 reports on the development of a THz time-domain (pulsed) spectroscopic imaging system using a set of independent optimized masks. The coherent detection scheme not only yields a THz signals with excellent SNR and high dynamic range, but also preserves the important phase information. This enabled us to measure a THz spectrum at each pixel in the image. Such a THz spectrum can be reconstructed and obtained by using CS. In the experiment, two well-defined absorption features were observed in the lactose spectrum; this result agrees well with the published data. To the best of our knowledge, this is the first time that a CS-THz system has been used to obtain both the spatial distribution and the spectral characteristics of a sample. Also, the design of these optimized masks (these binary masks are optimized to approximate the Karhunen-Loeve transform (KLT)) enables the sampling rate to be extremely small (only 10% of the pixels are required for reconstructing an image). The corresponding results have recently been published [18].

Chapter 5 further develops a faster and more efficient THz imaging system, based on a single spinning disk configuration, which allows the use of an electric motor to rotate the spinning disk, thus enabling the experiment to be performed automatically and continuously. In the THz imaging experiment, it took about 80 seconds to measure one THz image. We showed for the first time, to our knowledge, that a continuously spinning disk can be used for fast compressive TPI. A second generation spinning disk without substrate was developed to minimize the effect of the disk itself on the THz imaging system. This new generation spinning disk, which has the potential to achieve faster and more efficient THz imaging will be discussed. A brief summary of current CS-THz systems is reported at the end of this chapter. The results of this research into single spinning disk configuration have recently been published [19, 20].

Chapter 6 describes a three-dimensional (3D) joint reconstruction approach which has been applied to reconstruct THz images from random/incomplete subsets of THz data. Such a random sampling method provides a fast THz imaging application which can minimize the current THz imaging hardware implementation. We first propose to learn a spatio-spectral/temporal dictionary from a subset of available training data. Using this dictionary, the THz images can then be jointly recovered from an incomplete set of observations. The corresponding results have been accepted for publication [21].

Chapter 7 summarises the current achievements, i.e., random projection (Chapters 4 and 5) and random sampling (Chapter 6) on THz imaging. Compared with the current CS-THz techniques, the proposed CS-THz systems have been further developed to be faster and more efficient. Additional, this chapter includes suggestions for future work.

We anticipate achieving compact design, fast computation, and easy implementation with potential video rate THz imaging speed.

References:

[1] M. Walther, B. Fischer, M. Schall, H. Helm, and P. U. Jepsen, " Far-infrared vibrational spectra of all-trans, 9-cis and 13-cis retinal measured by THz time-domain spectroscopy," *Chem. Phys. Lett*. vol. 332, no. 3-4, pp. 389-395, 2000.

[2] Y. C. Shen, P. C. Upadhya, E. H. Linfield, H. E. Beere, and A. G. Davies, "Temperature-dependent low-frequency vibrational spectra of purine and adenine," *Appl. Phys. Lett.*, vol. 82, no. 12, pp. 2350-2352, 2003.

[3] A. G. Davies, A. D. Burnett, W. Fan, E. H. Linfield, and J. E. Cunningham, "Terahertz spectroscopy of explosives and drugs," *Mater. Today*, vol. 11, no. 3, pp. 18-26, 2008.

[4] B. B. Hu and M. C. Nuss, "Imaging with terahertz waves," *Opt. Lett*. vol. 20, no. 16, pp. 1716-1718, 1995.

[5] E. Pickwell, B. E. Cole, A. J. Fitzgerald, M. Pepper and V. P. Wallace, " In vivo study of human skin using pulsed terahertz radiation," *Phys. Med. Biol*. vol. 49, no. 9, pp. 1595-1607 , 2004.

[6] K. Kawase, Y. Ogawa, Y. Watanabe, and H. Inoue, "Non-destructive terahertz imaging of illicit drugs using spectral fingerprints," *Opt. Express*, vol. 11, no. 20, pp. 2549-2554, 2003.

[7] Y. C. Shen and P. F. Taday, " Development and application of terahertz pulsed imaging for non-destructive inspection of pharmaceutical tablet," *IEEE J. Sel. Top. Quantum Electron*. vol. 14, no. 2, pp. 407-415, 2008.

[8] A. W. M. Lee, Q. Qin, S. Kumar, B. S. Williams, Q. Hu, and J. L. Reno, "Real-time terahertz imaging over a standoff distance (>25 meters)," *Appl. Phys. Lett.*, vol. 89, no. 14, 141125, 2006.

[9] Z. Jiang and X. C. Zhang, "Terahertz imaging via electrooptic effect," *IEEE Trans. Microwave Th. Tech.*, vol. 47, no. 12, pp. 2644-2650, 1999.

[10] J. Pearce, H. H. Choi, D. M. Mittleman, J. White, and D. Zimdars, "Terahertz wide aperture reflection tomography," *Opt. Lett.*, vol. 30, no. 13, pp. 1653-1655, 2005.

[11] S. Wang and X. Zhang, "Pulsed terahertz tomography," *J. Phys. D: Appl. Phys.*, vol. 37, no. 4, pp. 964 (R31-R36), 2004.

[12] A. Bandyopadhyay, A. Stepanov, B. Schulkin, M. D. Federici, A. Sengupta, D. Gary, J. F. Federici, R. Barat, Z. H. Michalopoulou, and D. Zimdars, "Terahertz interferometric and synthetic aperture imaging," *J. Opt. Soc. Am. A*, vol. 23, no. 5, pp. 1168-1178, 2006.

[13] D. L. Donoho, "Compressed sensing," *IEEE Trans. Inf. Theory*, vol. 52, no. 4, pp. 1289-1306, 2006.

[14] E. J. Candès, J. Romberg, and T. Tao, "Robust uncertainty principles: Exact signal reconstruction from highly incomplete frequency information," *IEEE Trans. Inf. Theory*, vol. 52, no. 2, pp. 489-509, 2006.

[15] W. L. Chan, K. Charan, D. Takhar, K. F. Kelly, R. G. Baraniuk, and D. M.

Mittleman, "A single-pixel terahertz imaging system based on compressed sensing," *Appl. Phys. Lett.*, vol. 93, no. 12, 121105, 2008.

[16] W. L. Chan, M. L. Moravec, R. G. Baraniuk, and D. M. Mittleman, "Terahertz imaging with compressed sensing and phase retrieval," *Opt. Lett*. vol. 33, no. 9, pp. 974-976, 2008.

[17] W. L. Chan, H. T. Chen, A. J. Tayler, I. Brener, M. J. Cich, and D. M. Mittleman, "A spatial light modulator for terahertz beams," *Appl. Phys. Lett*., vol. 94, no. 21, 213511, 2009.

[18] Y. C. Shen, L. Gan, M. Stringer, A. Burnett, K. Tych, H. Shen, J. E. Cunningham, E. P. J. Parrott, J. A. Zeitler, L. F. Gladden, E. H. Linfield, and A. G. Davies, "Terahertz pulsed spectroscopic imaging using optimized binary masks," *Appl. Phys. Lett.*, 95, no. 23, 231112, 2009.

[19] H. Shen, N. Newman, L. Gan, S. C. Zhong, Y. Huang and Y. C. Shen, "Compressed terahertz imaging system using a spin disk," *35th International Conference on infrared, millimeter, and terahertz waves*, Rome, Italy, 2010.

[20] H. Shen, L. Gan, N. Newman, Y. Dong, C. Li, Y. Huang and Y. C. Shen, "Spinning disk for compressive imaging," *Opt. Lett.*, vol. 37, no. 1, pp. 46-48, 2012.

[21] H. Shen, V. Abolghasemi, L. Gan and Y. C. Shen, "Compressive three-dimensional (3D) terahertz imaging," *accepted by Institute of Physics' conference in optics and photonics, Photon12*, 2012.

Chapter 2

Background

2.1 Terahertz Imaging

Many challenges, such as a lack of suitable sources, sensitive detectors, and other components for the manipulation of radiation in terahertz (THz) range, limited the evolutions in the field of THz in the 1960s-1970s. However, in the 1980s, the development of the femtosecond laser provided an alternative way to conduct spectroscopy in the THz range. This method, which relies on the optical excitation of photoconductive dipole antennas, is so-called THz time-domain spectroscopy (THz-TDS) [1-4]. The first images acquired using THz-TDS, as shown in Figure. 2.1, were reported by Hu and Nuss in 1995 [5, 6]. This is an impressive milestone and leads the subsequent evolutions of THz imaging techniques. The subsequent developments of THz imaging are mainly based on THz-TDS, which is closely linked to the ultrafast laser technology, especially to the development of the Ti:sapphire femtosecond laser [7]. The following sections will discuss THz sources, THz detectors, THz-TDS, THz imaging and its applications.

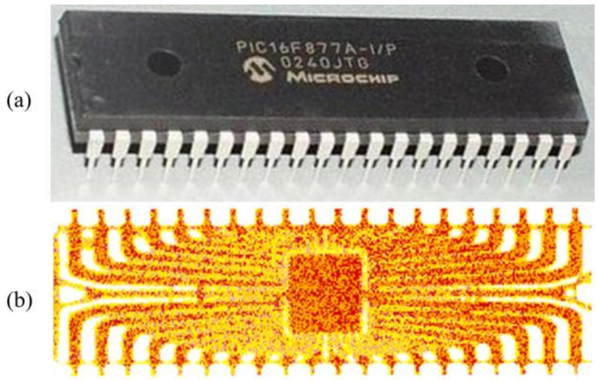

Figure. 2.1 (a) Photograph and (b) THz image of a packaged semiconductor integrated circuit (plastic packaging). This is one of the first images acquired using THz-TDS. Figure adapted from [5].

2.1.1 THz Sources

This section discusses several general sources for THz generation: photoconductive emitter, optical rectification, photomixing sources (continuous-wave (CW) generation), the backward wave oscillator (BWO), the far infrared laser (FIR laser), the quantum cascade laser (QCL), and the free electron laser (FEL).

A. Photoconductive emitter

Currently, the most widely used broadband time-domain (pulsed) THz sources are ultrashort laser driven THz emitters based on frequency down-conversion from the optical region [8]. Photoconduction, one of the most common approaches, is based on a photoconductive switch on a semiconductor substrate excited by a femtosecond laser pulse. The dynamics of the transient current that generated the electromagnetic field determines the frequency content. Therefore, a current transient that evolves on the timescale of a few hundred femtoseconds to a few picoseconds will generate a radiation in the THz range [9]. Figure 2.2 presents the practical implementation of a biased photoconductive switch/antenna for generation of THz pulses [10, 11]. The metallic electrodes provide the bias field to the photoconductive gap between these two electrodes. When impinging the femtosecond laser pulses onto the gap, the current impulses will be generated. High energy photons can excite electrons across the electronic bandgap of the photoconductor into the conduction band. Using femtosecond laser pulses, the resulting current transients will generate the THz pulses that are emitted by a THz dipole antenna structure. More details for generation and detection of THz pulses from biased semiconductor antennas can be found in previous research [12].

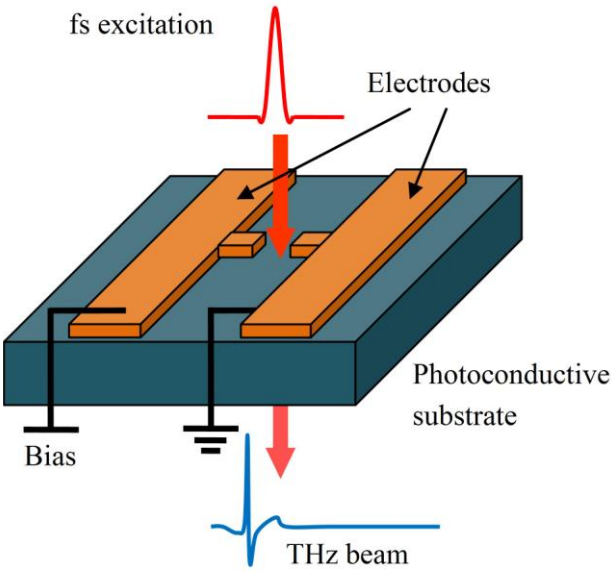

Figure. 2.2 Photoconductive antenna for generation of broadband THz pulses.

B. Optical Rectification

Another common method for generating broadband THz radiation is optical rectification, which is based on an electro-optic crystal by difference-frequency mixing of the frequency components of a femtosecond laser pulse [9]. The generation of THz radiation by nonlinear frequency mixing of laser beams was first demonstrated by mixing in $LiNbO_3$ and quartz in 1969 [13]. Over the past forty years, many papers have proposed this method using various materials, such as $LiNbO_3$ and $LiTaO_3$, GaAs and CdTe, and ZnTe, to achieve ultrabroadband generation of THz pulses [14-21]. The current 'hotspot' of this area is the generation and detection of ultrashort THz transients by four-wave mixing in the focal region of intense laser fields [22-24].

The generation of THz radiation by short laser pulses requires efficient difference-frequency mixing of all the frequency components within the spectrum of the laser pulse. Thus, a distribution of difference frequencies in the time domain appears as an electric field transient with a shape similar to the envelope of the laser pulse. This process has since been referred to as optical rectification. Two factors, the bandwidth of the excitation pulse and the phase matching between the near-infrared pump beam and the generated THz field, determine the bandwidth and temporal shape of the generated THz transient [9]. In the nonlinear crystal, the THz photons interact with the pump photons and create sidebands to the pump frequencies by difference- and sum- frequency generation (DFG and SFG), respectively. Note that this SFG process, which leads to the electro-optic effect, is widely used for optical detection [9].

By using both photoconduction and optical rectification approaches, the typical frequency range of generated THz radiation is from 0.1 to 3 THz or higher, depending on the laser pulse parameters. The average power levels range from nanowatts to hundred microwatts, and pulse energies are typically in the femtojoule to nanojoule range [8].

C. Photomixing Sources

Photomixing is the generation of CW THz radiation from two lasers. Such a THz generation approach delivers an outstanding performance if spectral resolution is the primary concern. It is a complementary method for photoconductive generation. Note that, compared with photoconductive broadband time-domain (pulsed) THz generation, no femtosecond laser is required in the CW systems. The output of two frequency stabilized lasers is spatially overlapped in a photomixer and focused onto a biased photoconductive antenna (PCA) with an optimized electrode geometry [25]. Thus, the mixing of these two incident waves is exploited to generate a CW THz radiation, which oscillates with two different frequencies of two incoming waves [26-28]. After detuning one of the lasers, the emission frequency can be swept in a wide spectral range. Both the amplitude and the phase of the CW THz radiation can be detected coherently with a homodyne detection scheme [26, 29].

The general principle for CW THz generation is similar to that for photoconductive broadband generation. Two CW lasers with identical polarization are required; the lasers with frequency ν_1 and ν_2 are spatial overlapped to generate a THz beat note.

The co-linear lasers are then used to illuminate the photoconductive THz emitter. Subsequently, the desired THz radiation with frequency $\nu_{THz} = \nu_1 - \nu_2$ is generated. A Silicon hyper-hemispherical lens is used to collimate the THz beam. Note that the linewidth and stability of the two lasers determine the spectral resolution of the CW THz generation. Thus, the spectral resolution offered by CW THz spectroscopy is significantly higher than any other techniques in the THz range [9].

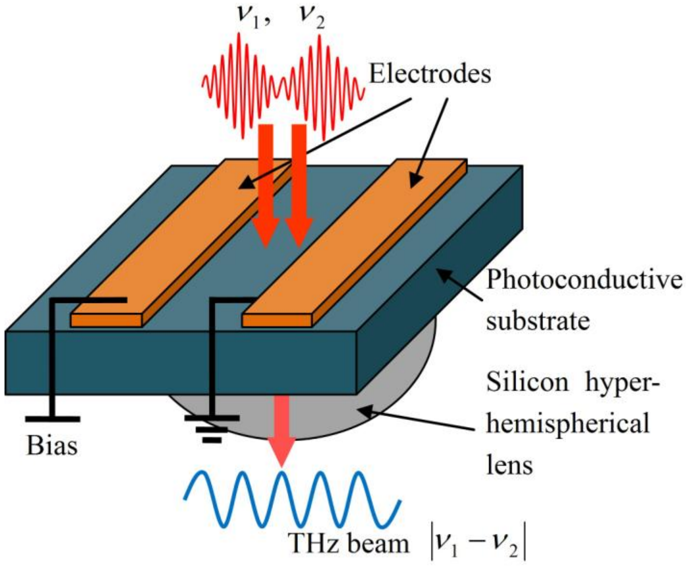

Figure. 2.3 Schematic diagram of two-beam photomixing with a photomixer.

D. Backward Wave Oscillator (BWO)

The BWO, also called backward wave tube, is a vacuum tube that is used to generate THz radiation [30]. An electron gun generates an electron beam that is interacting with a slow wave structure. The generated THz radiation has its group velocity directed opposite to the direction of motion of the electrons (i.e., the phase velocity of the wave is positive and the group velocity is negative). BWOs can operate in the THz region at moderate power levels (1-100 mW). A number of BWOs can be implemented and integrated into a system to generate a wide frequency range of THz radiation. A photo of BWO source which provides electromagnetic radiation at a single frequency is presented in Figure. 2.4.

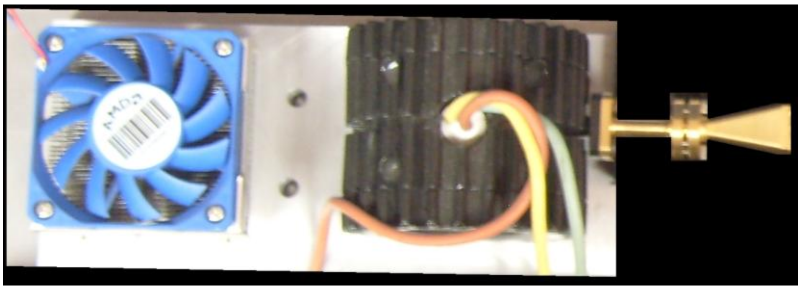

Figure. 2.4 A photo of BWO source (Insight Productive Company, USA) which provides electromagnetic radiation at 0.14 THz.

E. Far Infrared (FIR) Laser

The FIR gas laser is relatively old coherent source developed in the THz region. It is an optically pumped laser which consists of a long waveguide filled with gaseous organic molecules. The most widely used gas is methanol, which provides a powerful (typically 100 mW) emission line at 118 μm [8]. Such FIR laser is line-tuneable in the range of 0.3 to 5 THz. Because it is inefficient, often requires helium cooling, and is only line-tuneable, the FIR laser technology has seen only modest development in recent years.

F. Quantum Cascade Laser (QCL)

QCL is a semiconductor laser that emits in the mid- to far-infrared region. It has been demonstrated as a relatively new source developed in the THz spectrum, but until very recently several significant problems had prevented THz QCLs from being realized. The main problems are caused by the long wavelength of THz radiation. This results in a large optical mode, which results in poor coupling between the small gain medium and the optical field, and in high optical losses, owing to free electrons in the material [31]. The first QCL to operate in the THz region was developed by NEST-Pisa and the Cavendish Laboratory [32]. Such THz QCL emitted at 4.4 THz, providing about 2 mW of average power. They addressed the above and other problems in an innovative design. This system demonstrated pulsed operation at a temperature of 10 K (requires helium cool); however, the optimized fabrication promises to lead to CW operation at a temperature of 70 K (liquid nitrogen temperatures). The QCL-based THz systems have been demonstrated by many research groups, such as MIT and the University of Leeds [33, 34].

G. Free Electron Laser (FEL)

The FEL with energy-recovering linear accelerators provides extremely high-power THz emissions [35]. Unlike gas, liquid or solid-state lasers, in which electrons are excited in bound atomic or molecular states, FELs use a beam of high-velocity bunches of electrons propagating in a vacuum through a strong, spatially varying magnetic field [31]. The magnetic field causes the electron bunches to oscillate and emit photons. The FEL has an extremely wide frequency range and is widely tuneable. Also, it may generate CW or pulsed waves, and provides an average brightness of more than six orders of magnitude higher than typical photoconductive emitters. However, such systems require prohibitive costs, space and a dedicated facility.

Note that both the photoconductive emitter and BWO THz sources were used in our after-mentioned experiments to generate both broadband and single frequency THz radiation.

2.1.2 THz Detectors

Corresponding to the THz sources, several methods for THz detection are discussed here, including photoconductive sampling, free-space electro-optic sampling, thermal detectors (including bolometers), heterodyne detectors, extrinsic germanium detectors, and field-effect transistor (FET) detectors.

A. Photoconductive Sampling

One of the most common methods for broadband time-domain (pulsed) THz detection can be done by photoconductive detector. It has the same structure as the photoconductive emitter, whereas the only difference is that the detector antenna is not biased by any external circuit. A part of the femtosecond laser pulses' train is split and used to excite the detector structure. The detected THz pulses supply the electric field which required driving a photocurrent in the antenna. This photocurrent can be presented as a convolution of the electric field acquired by the antenna and the transient photoconductivity acquired by the gate pulse [9]. When the transient photoconductivity is much faster than the duration of the THz field, the photocurrent is proportional to the THz field strength. Oppositely, with long-live photoconductivity, the photocurrent is proportional to the temporal integral of the THz field. Therefore, the trapping and recombination time of the photoinduced carriers determines the bandwidth of the detector, and the transient photoconductivity can be treated as a low-pass filter function that is applied to the frequency spectrum of the THz pulse incident on the detector [9].

The material of the photoconductive detector is important for acquiring a high bandwidth of the detected THz signal. In 1988, radiation-damaged silicon-on-sapphire was used as photoconductive material [2]. Currently, low-temperature-grown (LTG) GaAs with a few hundred femtosecond carrier lifetimes is popular [36-39]. Other materials with smaller bandgaps, such as LTG-GaAsSb [40], LTG-InGaAs [41], superlattice structures with LTG-InGaAs/InAlAs [42, 43] and ion-implanted InGaAs [44-46], have also been proposed.

B. Free-Space Electro-Optic Sampling

The electro-optic (EO) sampling, another common method for broadband time-domain (pulsed) THz detection, is a coupling between a low-frequency electric field (i.e., THz pulse) and an optical pulse (the laser beam). As shown in Figure. 2.5, the THz electric field modulates the birefringence of the sensor crystal; and this in turn modulates the polarization ellipticity of the laser beam [31]. The probe polarization evolves into an almost circular, but elliptical, polarization after a λ/4 plate. A Wollaston prism splits the probe beam into two orthogonal components, which are sent to a balanced photo-detector. The ellipticity modulation of the laser beam, i.e., the difference between the two orthogonal components of the probe pulse, can then be used to analyze the information on both the amplitude and phase of THz pulse. The materials of such electro-optic method have already been studied in the aforementioned broadband THz sources based on an electro-optic crystal. Note that the noise equivalent power (NEP) of both photoconductive and electro-optic detectors is around 10^{-15} W/Hz$^{1/2}$; and the operating temperatures are both at room temperatures. Such EO sampling approach is used in our after-mentioned experiment to detect the broadband time-domain (pulsed) THz radiation.

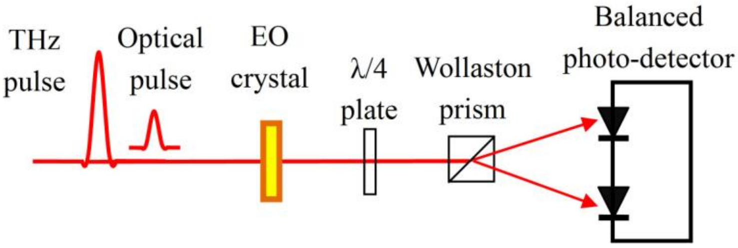

Figure. 2.5 Schematic diagram of a typical setup for free-space EO sampling.

C. Thermal Detectors

Many types of thermal detectors, such as bolometers, Golay cells, and pyroelectric detectors, can be used in the THz region [47]. Due to the low output power of THz sources, most of these systems require cooling to reduce the relatively high levels of thermal background radiation. Such approaches can reach NEP=10^{-17} W/Hz$^{1/2}$ at an extremely low temperature - about 4 K and below. In a specific case, using the hot-electron Titanium nanobolometers, the NEP can reach 3×10^{-19} W/Hz$^{1/2}$ at 0.3 K [48]. The operation principles of thermal detectors have been described in various research [49]. Some of the thermal detectors can operate at room temperature, whereas the NEP is relatively larger. A photo of one of the pyroelectric detectors is shown in Figure. 2.6; and note that this pyroelectric detector is used in our after-mentioned experiment to detect the single frequency THz radiation from a BWO source.

Figure. 2.6 A photo of pyroelectric detector (SPH-49, Spectrum Detector Inc. USA). NEP=3×10^{-9} W/$Hz^{1/2}$.

D. Heterodyne Detectors

Heterodyne detectors are used in applications requiring very high spectral resolution of the detector. A local oscillator source at the THz frequency is mixed with the received THz signal in these systems. The downshifted signal is then amplified and recorded [31]. A Schottky-diode mixer has been reported for sensing applications at 2.5 THz [50]. Cryogenic cooling can be used for higher sensitivity in heterodyne detectors. The most widely used is the superconductor-insulator-superconductor tunnel junction mixer [51]. More details of the heterodyne detectors have been discussed in various research [52].

E. Extrinsic Germanium Detectors

The germanium-based extrinsic photoconductor detector is the first extrinsic photo-detector. Due to the limitation of silicon detectors (i.e., for wavelengths longer than 40 μm there are no appropriate shallow dopants for silicon), the germanium devices are more suitable for detecting long wavelengths. The NEP can reach a few parts 10^{-17} W/$Hz^{1/2}$ in a doped germanium crystal. A general review of extrinsic germanium detectors has been studied in various research [47].

F. Field-Effect transistor (FET) Detectors

FET detectors can be used for both resonant (single wavelength) and non-resonant (broadband) THz detection and can be directly tuneable by changing the gate voltage. They can operate in room temperatures where the achieved NEP is around 10^{-10} W/Hz$^{1/2}$. The operation principle of FET has been discussed in various research [47].

2.1.3 THz Time-Domain Spectroscopy (THz-TDS)

Experimental Setup

The THz-TDS system, which allows a material's far-infrared optical properties to be determined as a function of frequency, has been reviewed in several publications [9, 53-57]. Basically, in THz-TDS systems, the photoconduction and optical rectification can be used for THz generation; correspondingly, the photoconductive sampling and free-space EO sampling can be used for THz detection. The nonlinear optical techniques (optical rectification and EO sampling) are especially advantageous in their broadband properties and well-investigated frequency properties. However, the photoconductive antenna has a number of materials and fabrication techniques and may provide some complementary functions to optical rectification and EO sampling techniques. Figure 2.7 illustrates the THz-TDS system that was used in our experiment, using a photoconductive emitter for THz generation and the EO crystal for THz detection. A Ti:sapphire femtosecond laser provides ultrashort visible/near-infrared pulses. The output is split into two parts: a pump beam is used for THz generation and a probe beam for THz detection. The optical pulse is focused onto a biased PCA. The THz pulse generated from the PCA is collimated by the parabolic mirrors and is finally focused onto the EO crystal. Note that, except for such transmission THz-TDS, other implementations such as reflection THz-TDS and attenuated total reflection (ATR) THz-TDS are also widely used in spectroscopy applications [58-67].

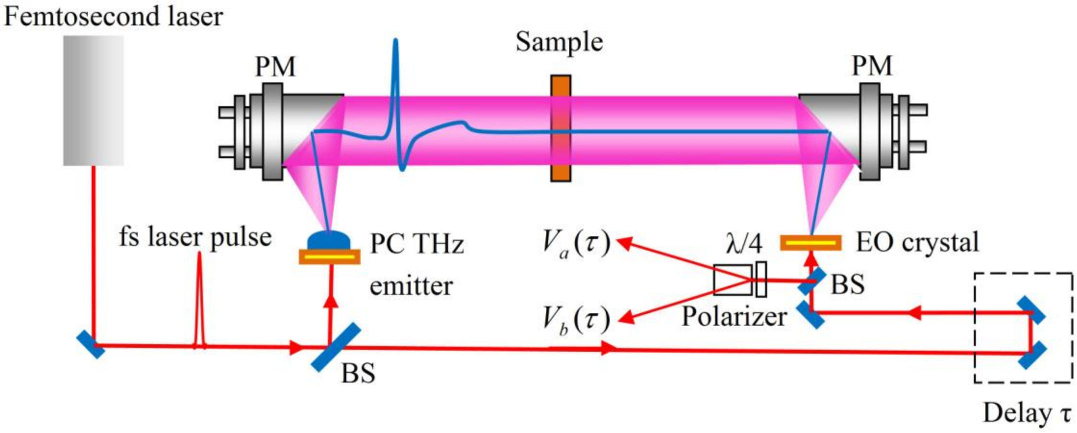

Figure. 2.7 Schematic configuration of a full THz-TDS system for transmission spectroscopy. A photoconductive emitter is used for THz generation and an EO crystal is used for THz detection. (PM: parabolic mirror, BS: beam splitter, PC THz emitter: photoconductive THz emitter, and EO: electro-optic).

Data Analysis

The first application of transmission THz-TDS was proposed in 1989 on water vapour in the ambient atmosphere [4], and subsequently the absorption coefficient and index of refraction of a range of dielectrics and semiconductors were reported [68]. To date, transmission THz-TDS is widely used in most THz spectroscopy measurements. The THz-TDS systems shown in Figure 2.7 are performed in transmission configuration.

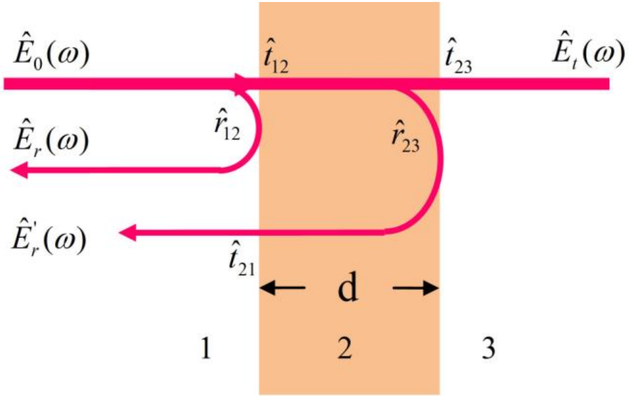

Figure. 2.8 Schematic diagram of the geometries for transmission and reflection THz spectroscopy. $\hat{E}_0(\omega)$ is the incident field, $\hat{E}_t(\omega)$ is the transmitted field, and $\hat{E}_r(\omega)$ and $\hat{E}_r^{'}(\omega)$ are the reflected fields from first and second interface of the sample. Figure adapted from [9].

The general schematic diagram of the geometries for transmission and reflection THz spectroscopy is presented in Figure 2.8. The incident THz pulse can be described by its spectral amplitude and phase $\hat{E}_0(\omega)$, which is obtained by Fourier transformation of the measured THz data in time-domain. Ignoring the multiple reflections within the sample, the transmitted and reflected signals in this geometry can be expressed as [9]

$$\begin{aligned} \hat{E}_t(\omega) &= \hat{E}_0(\omega)\hat{t}_{12}\hat{t}_{23}e^{-\alpha d/2}e^{in\omega d/c}, \\ \hat{E}_r(\omega) &= \hat{E}_0\hat{r}_{12}, \\ \hat{E}_r^{'}(\omega) &= \hat{E}_0\hat{t}_{12}\hat{r}_{23}\hat{t}_{21}e^{-\alpha d/2}e^{in\omega d/c}, \end{aligned} \tag{2.1}$$

where $\hat{t}_{12}$, $\hat{t}_{23}$, $\hat{r}_{12}$, and $\hat{r}_{23}$ are various complex Fresnel field transmission and reflection coefficients. Such transmission and reflection spectroscopy can be used to acquire the complex index of refraction of the sample, $\hat{n}(\omega) = n(\omega) + i\kappa(\omega)$, where $\kappa(\omega)$ is the extinction coefficient which related to the absorption coefficient $\alpha(\omega)$ through $\kappa(\omega) = \alpha(\omega)c/2\omega$. In transmission THz-TDS, two THz pulses, respectively propagating through air and the sample, are recorded and their spectral amplitudes and phases can be compared as [9]

$$\frac{\hat{E}_{sam}(\omega)}{\hat{E}_{ref}(\omega)} = T(\omega)e^{i\varphi(\omega)} = \hat{t}_{12}\hat{t}_{23}e^{-\alpha d/2}e^{i(n-1)\omega d/c}. \tag{2.2}$$

For analyzing the sample materials with low absorption coefficient, the Fresnel transmission coefficients are real-valued, and at normal incidence we find [9]

$$n(\omega) = 1 + \frac{\varphi(\omega)c}{\omega d}, \tag{2.3}$$

$$\alpha(\omega) = -\frac{2}{d}\ln\left(\frac{(n+1)^2}{4n}T(\omega)\right). \tag{2.4}$$

In Figure 2.9, an example of a typical transmission THz-TDS measurement is shown. Figure 2.9 (a) illustrates a time trace of the THz signal, and Figure. 2.9 (b) presents the frequency spectra of this THz signal.

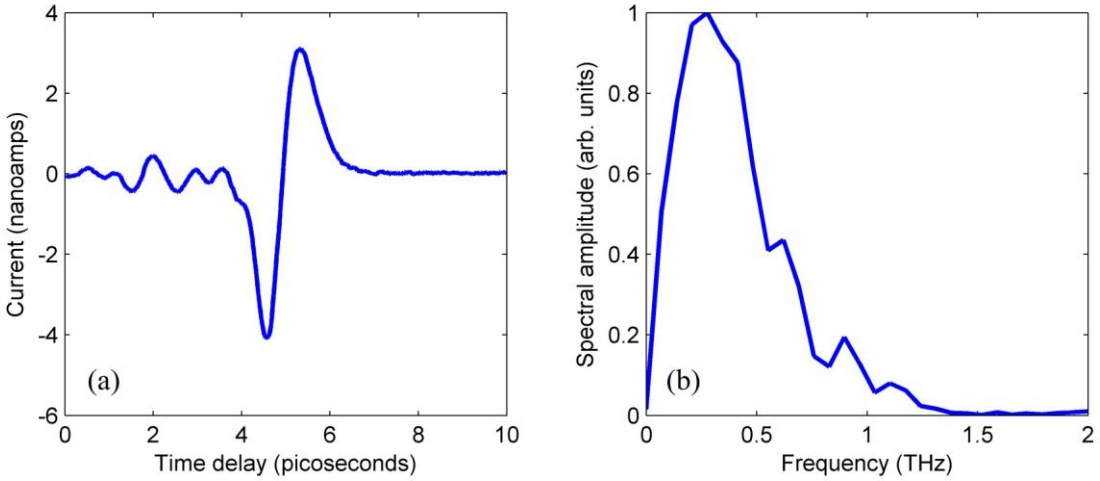

Figure. 2.9 (a) THz bandwidth transient recorded in the time domain and (b) its corresponding frequency spectrum.

Equations (2.3) and (2.4) are only suitable for the sample materials with vanishing absorption and infinite thickness. For thin samples, the multiple reflections of the signal in the sample need to be taken into account. A sequence of signal echoes will appear following the main transmitted pulse in time domain. To solve this problem, Duvillaret *et al.* proposed a general situation including a Fabry-Perot factor $FP(\omega)$ and complex valued Fresnel transmission coefficients [69]. For a sample in air, the generalized transmission function $\hat{T}(\omega)$ is [9, 69]

$$\hat{T}(\omega) = \frac{\hat{E}_{sam}(\omega)}{\hat{E}_{ref}(\omega)} = \frac{4\hat{n}}{(\hat{n}+1)^2} e^{-\alpha d/2} e^{in\omega d/c} FP(\omega)\,, \tag{2.5}$$

where

$$FP(\omega) = \frac{1}{1-(\frac{\hat{n}-1}{\hat{n}+1})e^{-\alpha d} e^{2in\omega d/c}}\,. \tag{2.6}$$

The same authors demonstrated a method based on the presence of multiple signal echoes to calculate the sample thickness [70]. This method improves the determination of the optical constants, such as index of refraction, through simultaneous determination of the sample thickness. The thickness of any material with moderate absorption can be precisely obtained using this method.

Advantages and Disadvantages of the Time-Domain Approach

After the development of the Fourier Transform technique in the 1950s, a well established technique, Fourier transform infrared (FTIR) spectroscopy, became a standard analytical method in the frequency range between 500 to 4000 cm^{-1}. The advantages and disadvantages of the time-domain approach when compared to FTIR spectroscopy will now be discussed.

Firstly, the time-domain approach measures the transient electric field, not merely intensity of the THz radiation. Compared with the FTIR method, time-domain approach enables to obtain the THz spectrum with much better sensitivity and dynamic range [71]. Thus, high-quality THz spectra can be obtained easily and widely.

Secondly, because of the time-gated coherent detection technology used, the measurement is sensitive only to coherent radiation, and moreover only to radiation which is phase-locked to the repetition rate of the femtosecond oscillator. That means the extraneous ambient noise from the incoherent blackbody radiation can be minimized. As a result, the system can operate at room temperature without the liquid cryogens which had previously limited the wide use of THz spectrometers.

Thirdly, as shown in Figure 2.9, the time-domain system provides both a typical waveform and the corresponding spectral amplitude and phase. The waveform in Figure 2.9 (a) is recorded as a function of time delay from a photoconductive sampling measurement. This is approximately proportional to the THz electric field, which contains both the amplitude and phase information.

Fourthly, another benefit is the broad bandwidth of the radiation, which is broader than any other source in the THz range. In THz-TDS, the broadband coverage can be used for chemical mapping, which means locating materials by relying on their unique THz absorption signatures.

It is also worth noting that the THz-TDS have some limitations. As the non-linear optical mixing is inefficient, it makes the power in the THz beam extremely low. Although the dynamic range could be quite high in THz-TDS, which means the detector can filter many common noises [72], the detector still requires a lot of power to operate. Therefore, most of existing THz imaging systems rely on the raster scanning method to scan an object using a single detector. In practice, such a method significant limits the image acquisition time.

Other limitations are inherent in the nature of the time-domain system [57]. In most cases, the spectral resolution is limited by the length of a scanning delay line in a conventional Fourier transform spectrometer. Thus, such a system is inadequate to achieve high-resolution applications. Also, the experiment may require a source to operate in the higher frequency range. THz-TDS system performs well in the low-frequency THz range, such as below 1 THz, whereas it performs less well in comparison to a quantum cascade laser operating at a high-frequency THz range [8]. The expensive femtosecond laser source is another disadvantage for most of the common applications.

Generally speaking, transmission/reflection/ATR THz-TDS not only have the above advantages and disadvantages but also have respective benefits: transmission configuration offers reliable and quantitative THz spectra; reflection configuration can be used to study opaque samples; and ATR configuration is more suitable for rapid screening of many samples.

2.1.4 THz time-domain (pulsed) imaging (TPI)

Since the first TDS imaging system was reported in 1995 [5, 6], most of the THz imaging since then has been based on THz-TDS, so-called THz time-domain (pulsed) imaging (TPI). Such an imaging system has all the previously mentioned advantages of the time-domain approach. This technique will now be briefly discussed, including its imaging modes, experimental setup and data analysis.

Experimental Methods (Transmission/Reflection TPI)

Most of the early studies were based on transmission TPI [5, 6], as shown in Figure 2.3. The THz radiation is generated by pumping a biased THz emitter with an ultrashort laser pulse from a femtosecond laser. This THz radiation is collected, collimated and then focused onto the sample. After penetrating the sample, the THz radiation is then collected and focused onto the THz detector.

In a THz imaging measurement, the THz waveform is taken from each position over the surface of a sample and recorded as function of time delay. Such an imaging system offers three-dimensional information: the vertical and horizontal dimension of the sample and the time-delay (depth) dimension. After measuring the THz waveform for each position of the sample, one can build the image pixel by pixel. Typically, images obtained using different portions of the data contain different types of information about the sample. Peak-to-peak amplitude of the THz time-domain pulse provides the amount of THz absorption at different parts of the image; whereas spectral phase and time delay of the transmitted THz pulse offers the thickness of the sample.

Currently, TPI has been developed for many applications. However, the penetration depth is limited to only a few hundred microns because of the strong absorption of the great number of samples. Therefore, another powerful THz-TDS system, reflection TPI, is more appropriate for some THz imaging applications, as it not only allows opaque samples but also allows the use of the time-of-flight capabilities of the technique [11, 73]. By measuring the time difference of THz pulses reflected from the surface and the inner structures of the sample, the thickness of the sample can be directly determined. This method offers a better performance than other indirect methods such as the near-IR spectroscopy approach [73, 74]. All the thickness information of multilayered samples can be identified using this approach. Figure 2.10 shows the schematic diagram of a reflection TPI system.

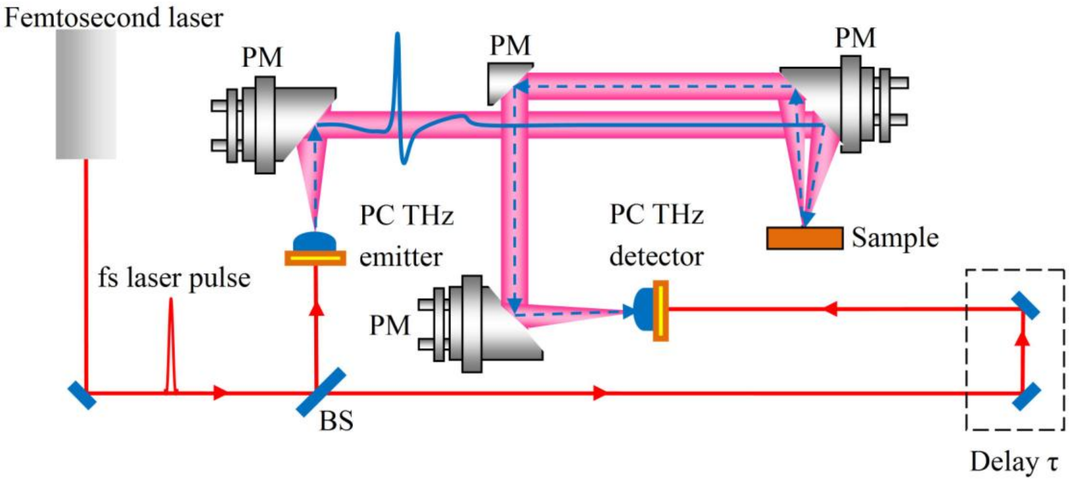

Figure. 2.10 Schematic diagram of a reflection TPI system. (PM: parabolic mirror, BS: beam splitter, PC THz emitter: photoconductive THz emitter, and PC THz detector: photoconductive THz detector).

Data Analysis

Here we studied the data analysis in a reflection TPI system, and the data analysis of transmission TPI system can be studied in a similar way. In order to analyze the THz data, the electromagnetic theory of studying the THz propagation in a multilayered medium is used. The incident THz pulse was first Fourier transformed to frequency domain. Then the transmission and reflection coefficients were calculated at each frequency using a 1-D model [75], together with the complex dielectric function for each layer of sample. The calculated reflection coefficients were finally Fourier transformed back to time domain to obtain a typical THz waveform with sample information. It was assumed that the incident THz radiation is p-polarized (i.e., the component of the electric field parallel to the incident plane) and the M-layered medium is uniform in the transverse. The schematic diagram of this 1-D model is shown in Figure. 2.8. The magnetic field of the THz radiation only has a z-component, which can be expressed as [63, 75]

$$H_z^{(i)}(x,y) = A_i \exp(j(\beta_0 x - \beta_i y)) + B_i \exp(j(\beta_0 x + \beta_i y)) \;\; (i = 1, 2, \ldots, M) \tag{2.7}$$

where

$$\beta_0 = \sqrt{\varepsilon_1(\nu)}k_0 \sin\theta$$

$$\beta_i = \sqrt{\varepsilon_i(\nu)k_0^2 - \beta_0^2} \;\; (i = 1, 2, \ldots, M) \tag{2.8}$$

With k_0 the wavevector in vacuum, θ the incidence angle, and $\varepsilon_i(\nu)$ the dielectric function in the *i*th layer of the sample. The *x*-component of the electric field can be obtained from Maxwell's equation [63, 75]

$$E_x^{(i)}(x,y) = \frac{1}{j\omega\varepsilon_i(\nu)} \frac{\partial[H_z^i(x,y)]}{\partial y}. \tag{2.9}$$

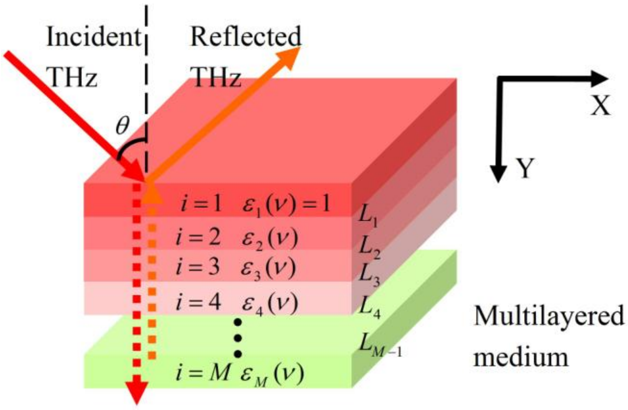

Figure. 2.11 Schematic diagram of 1-D model for simulating THz propagation in a multilayered medium.

According to the continuity of $H_z^{(i)}(x,y)$ and $E_x^{(i)}(x,y)$ at the boundary $y = L_i$, the boundary conditions are [75]

$$H_z^{(i)}(x,L_i) = H_z^{(i+1)}(x,L_i)$$

$$E_x^{(i)}(x,L_i) = E_x^{(i+1)}(x,L_i) \;\; (i = 1, 2, \ldots, M-1). \tag{2.10}$$

Therefore, we can obtain the following iterative formula from equation (2.10) [75]:

$$A_i = \frac{\exp(j\beta_i L_i)}{2}[A_{i+1}(1+\tau_i)\exp(-j\beta_{i+1}L_i) + B_{i+1}(1-\tau_i)\exp(j\beta_{i+1}L_i)]$$

$$B_i = \frac{\exp(j\beta_i L_i)}{2}[A_{i+1}(1-\tau_i)\exp(-j\beta_{i+1}L_i) + B_{i+1}(1+\tau_i)\exp(j\beta_{i+1}L_i)] \quad (2.11)$$

where $\tau_i = \varepsilon_i \beta_{i+1} / \varepsilon_{i+1}\beta_i$. Given arbitrarily, $A_M = 1$ and $B_M = 0$, A_1 and B_1 can be calculated by iterating equation (2.9). The reflection coefficient can be written as $|B_1 / A_1|$, the transmission as $|A_M / A_1|$, and the absorptance as $1-|B_1 / A_1| - |A_M / A_1|$. Note that, in the case of *s*-polarized incident THz (i.e., the component of the electric field perpendicular to the incident plane), we can use the similar way for analysis, but $\tau_i' = \beta_{i+1} / \beta_i$ will be used to replace τ_i [75].

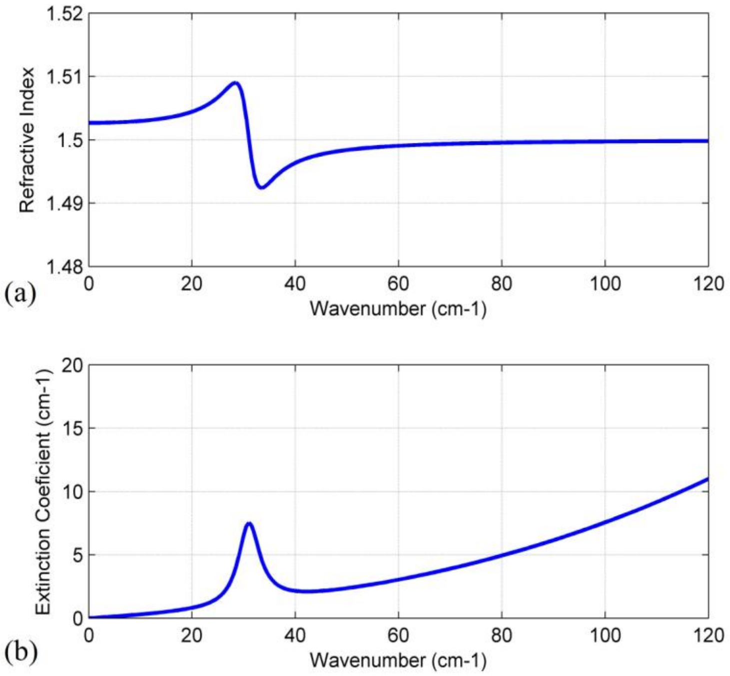

Figure. 2.12 Simulated (a) refractive index and (b) extinction coefficient using a Lorentz model. Here, the center frequency value is 31 cm^{-1} (0.93 THz); the width of oscillator is 5 cm^{-1}; the strength of the oscillator is 8 cm^{-1}; and the C_1=0.2, C_2=0.2, C_3=0.2 and C_4=0.

A Lorentz model with *K*-oscillators is used to express the complex dielectric function in the *i*th layer of the sample [63]:

$$\varepsilon_i(\nu) = [n_i(\nu) + j\frac{\alpha(\nu)c}{4\pi\nu}]^2$$

$$= \sum_{k=1}^{K} \frac{S_k^{(i)}(\nu_k^{(i)})^2}{(\nu_k^{(i)})^2 - \nu^2 - j\nu\Gamma_k^{(i)}} + [n_0^{(i)} - j(C_1^{(i)} + C_2^{(i)}\nu + C_3^{(i)}\nu^2 + C_4^{(i)}\nu^3)]^2 \qquad (2.12)$$

where $\nu_n^{(i)}$, $\Gamma_n^{(i)}$, and $S_n^{(i)}$ are the centre frequency, the width, and the strength of the *k*th oscillator (*k*=1, 2, ..., *K*) for the *i*th layer (*i*=1, 2, ..., *M*). The real part of this equation is the refractive index and the imaginary part, i.e., the second item in the bracket is an empirical expression for the extinction coefficient. Figure. 2.12 presents an example to simulate refractive index and extinction coefficient using a Lorentz model with one oscillator, which has one spectral feature at 31 cm^{-1} (0.93 THz). It is clear that such an oscillator will introduce the spectral feature of sample in both refractive index spectrum and extinction coefficient spectrum. Using the aforementioned equations, we can express a THz waveform reflected from a layered sample under normal incident condition [63]:

$$R(\nu) = \frac{B_1(\nu)}{A_1(\nu)} \equiv r_1(\nu) + \frac{[1 - r_1(\nu)][1 + r_1(\nu)]r_2(\nu)\exp(-j2\beta_2(\nu)D)}{1 + r_1(\nu)r_2(\nu)\exp(-j2\beta_2(\nu)D)} \qquad (2.13)$$

where *D* is the coating thickness, and

$$r_1(\nu) = \frac{1 - \tau_1(\nu)}{1 + \tau_1(\nu)} = \frac{\sqrt{\varepsilon_2(\nu)} - \sqrt{\varepsilon_1(\nu)}}{\sqrt{\varepsilon_2(\nu)} + \sqrt{\varepsilon_1(\nu)}}$$

$$r_2(\nu) = \frac{1 - \tau_2(\nu)}{1 + \tau_2(\nu)} = \frac{\sqrt{\varepsilon_3(\nu)} - \sqrt{\varepsilon_2(\nu)}}{\sqrt{\varepsilon_3(\nu)} + \sqrt{\varepsilon_2(\nu)}}. \qquad (2.14)$$

Taylor expansion is used to rewrite equation (2.13) for understanding the physical meaning [63]:

$$R = r_1 + (1 - r_1^2)r_2[\exp(-j2\beta_2 D) - r_1 r_2 \exp(-j4\beta_2 D) + r_1^2 r_2^2 \exp(-j6\beta_2 D) - \ldots]. \qquad (2.15)$$

Now, it is clear that the first item is the THz reflection from the surface and the second item represents the THz multiple reflections within the sample. The first item in the brackets corresponds to the "fundamental" reflection and the rest of the items correspond to the "parasitic" reflection [63]. After Fourier transforming it back to time domain, all the multiple reflections can be separated because of their phase difference.

Normally, the strength of "parasitic" reflection is much less than that of the "fundamental" reflection unless the change in refractive index at the interface is large. So such "parasitic" reflection can be used to identify the presence of air gap within the multilayered medium.

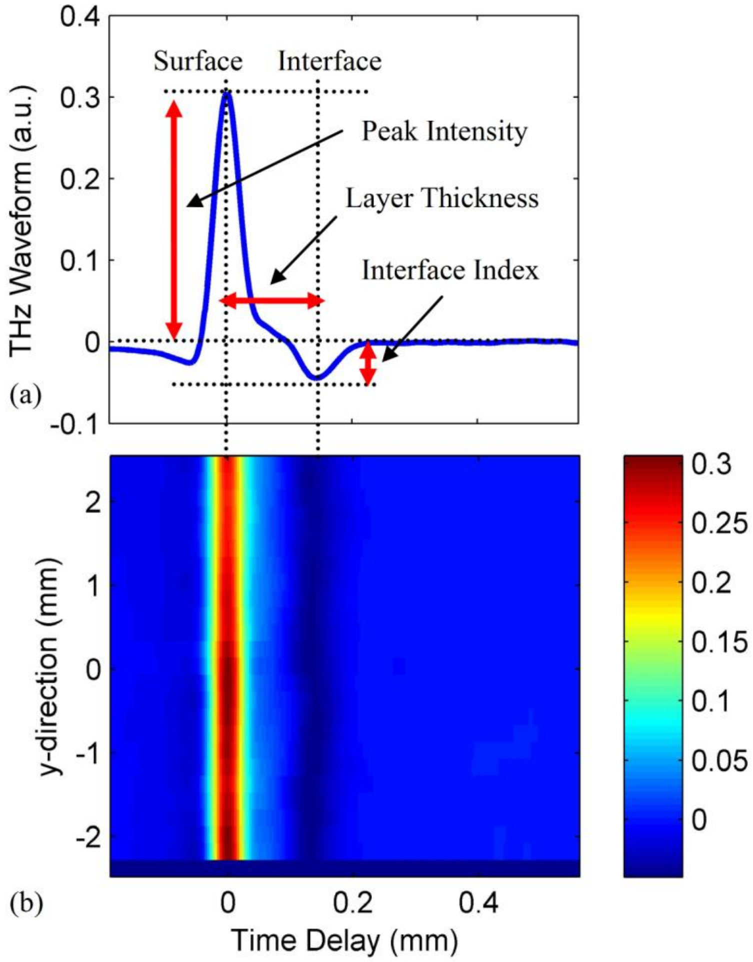

Figure. 2.13 (a) Typical THz waveform measured for a one-layer sample. (b) B-scan of THz waveforms measured for a one-layer sample.

A typical THz waveform, as shown in Figure. 2.13 (a), can be obtained by Fourier transformed back to time domain. Figure. 2.13 (a) shows a one-layer sample, and it is easy to identify the peak intensity, which is an indicator to the refractive index of the surface. The interface index, which gives a measure of the strength of reflection from the interface, can also be obtained. Between these two peaks, the surface reflection and the interface reflection, the layer thickness can be consequently calculated. It is noted that the absolute layer thickness can be determined by the value of refractive index of each layer. n_1, which is the refractive index of air, is equal to 1. Then, according to the THz waveform and aforementioned equations, n_2 and n_3 can be estimated one after another. Finally, the layer thickness can be calculated. Basically, with the knowledge of any two of the THz waveform, the refractive indices and the layer thickness, the other one can be easily determined. More details about the reflection TPI, such as a discussion about the oscillation-like features caused by resonance absorption, etc., can be found in other research [63]. From Figure. 2.10 (b), the B-scan of the one-layer sample is shown after measuring a row of THz waveforms from Figure. 2.10 (a). It is easy to identify the surface in red and the interface in dark blue, respectively. A whole image of the sample can be obtained by raster scanning it.

As discussed, the TPI system offers three-dimensional information: the vertical and horizontal dimension of the sample and the time-delay (depth) dimension. We can use different portions of the data to obtain an image of the sample. To demonstrate this point, Figure. 2.14 illustrates the THz transmission images of a chocolate bar obtained by two different portions of the THz data [77]. Figure. 2.14 (a) shows the image obtained by the peak-to-peak amplitude of the time-domain THz pulse. From this image it can be found that: firstly, the middle part is thicker than the top and bottom part of the sample – this is because of the sample’s plano-convex structure. Secondly, considering the scattering effects of the sample, the embossed letters are visible but rather difficult to read. Thirdly, the inner materials, almonds, can be easily identified because they absorb more THz radiation than chocolate. Figure. 2.14 (b) presents the image obtained by a different method, based on the transit time of the THz pulse through the sample, rather than the amplitude that used in Figure. 2.14 (a). Because the thicker sample delays the THz pulse to a greater extent, using this method, the image contains the information of thickness of sample. As a result, the embossed letters, which are thicker than other parts of the sample, are more easily distinguished. It is noted that, the primary source of noise in the THz-TDS system comes from the instability of the femtosecond laser source. These noise sources have much more effect on the peak-to-peak THz pulsed amplitude compared to that on the path length delay corresponding to the phase of the THz pulse. Therefore, images obtained using the time delay or phase of the pulse can offer better quality than those which depict the amplitude transmission. More details about the transmission TPI system have been proposed in other research [77].

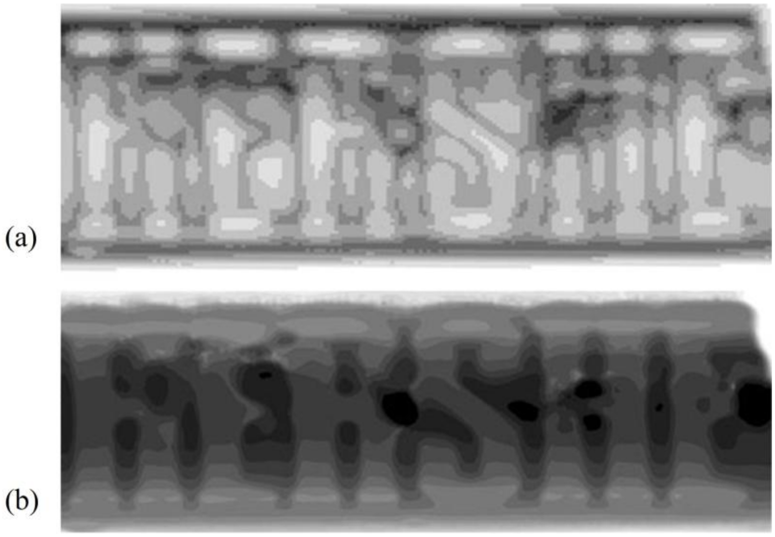

Figure. 2.14 THz transmission images of a chocolate bar obtained by using (a) peak-to-peak amplitude of the transmitted time-domain pulse and (b) variation in transit time of the THz pulse through the sample. Figure adapted from [77].

Most TPI systems rely on the raster scanning method to form an image pixel by pixel. Other more approaches, such as THz tomography and interferometric imaging, single-shot electro-optic sensing using crossed polarizers and a CCD camera, chirped-pulse technique, and a parallel method with the time-domain techniques, CW THz systems, are not further discussed here but details about them can be found in other research [78-85].

2.1.5 Applications of THz Imaging

The applications of THz imaging exploit the unique properties of THz radiation, which include the transparency of common packaging materials; and many desired materials exhibit unique spectral fingerprints in the THz range, which can be used for chemical mapping. Since the first image with a THz-TDS system was obtained in 1995 [5] and the first CW image obtained with a photomixer based system was reported in 2001 [86], many applications have used THz imaging, due to its non-destructive nature. Currently the THz imaging research has expanded into the fields of security screening [87-91], plastics industry [92-96], pharmaceutical industry [11, 63, 97-101], and art conservation [102-106].

A. Security Screening

The THz systems have considerable marketing potential in the field of security, such as body scanner, mail and luggage inspection, and hand-held optoelectronic THz system [87-91]. Some of the so-called body scanners have been recently used at airports, where most of them operate at a few tens of GHz; and other THz receiver arrays under development are based on highly developed microwave technology at one or a few hundred GHz [9]. These will not be discussed further here because, strictly speaking, these systems do not operate in the classic optoelectronic THz range.

As many crystalline substances possess sharp characteristic spectral features in the THz range, together with the ability of THz radiation to propagate through common barrier materials, optoelectronic THz systems have been developed for explosives' or illicit drugs' detection within an envelope, a parcel or a suitcase. As an impressive example, Picometrix developed a QA-1000 THz imaging system for transmission imaging [91]. The transmission image through an attaché case is presented in Figure. 2.15. All the desired inner objects, such as a knife, a bottle and a gun, can be identified easily. In this case, the pixel intensity was logarithmically proportional to power integrated from 0.2 to 2 THz. Sixty-six pixels can be obtained per second and each pixel has a size of 1.5 mm×1.5 mm. The raster scan speed was 0.1 m/s in continuous motion. At this rate and resolution, it took approximately 100 minutes to scan a 1 m^2 area of the object. It is worth noting that any metal-made (such as aluminium) suitcase is not transparent to THz radiation. Because of this problem and the long scanning time, THz imaging can be used as a supplement to current X-ray scanners but is unlikely to replace them.

While bulk explosives like RDX have already been spectroscopically analyzed in the THz region [87, 88], liquid explosives still need to be characterized. Currently, some research groups in Marburg and at DTU are working on the hand-held optoelectronic THz systems for the detection of liquid explosives.

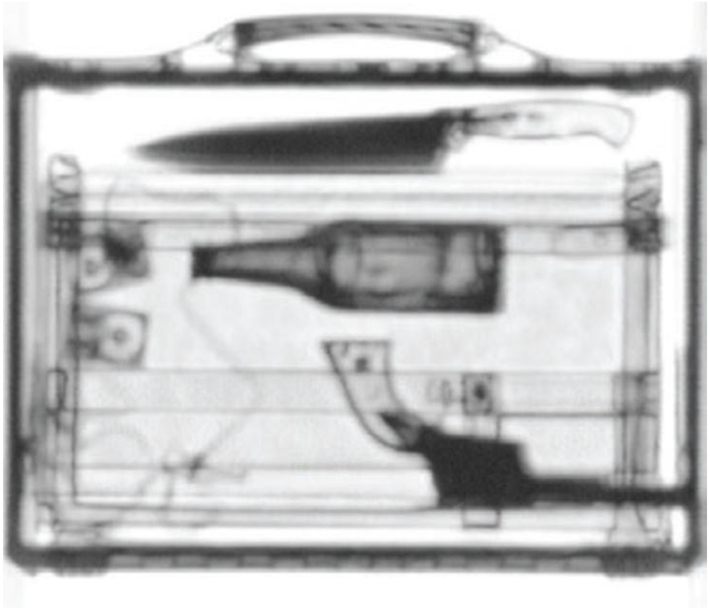

Figure. 2.15 Transmission image through an attaché case using QA-1000 THz imaging system. All the inner objects, such as a knife, a bottle and a gun, are clearly identified. Figure adapted from [91].

B. Plastics Industry

Several applications regarding the THz system in the plastics industry, such as inline monitoring of polymeric compounding processes, the quality control of plastic weld joints, and fibre orientation, have previously been discussed [92-96].

This research looks at one of the applications: the determination of additive content in polymeric compounds with THz-TDS [92]. Polymeric compounds are mixtures of polymeric-based materials and various additives. These various added substances are used to improve the properties of standard polymers for a variety of applications. In plastics industry, it is important to guarantee the precise composition of the materials with respect to their additive content.

THz-TDS was shown to identify a variety of additive-polymer combinations with differing additive contents [92]. It was found that standard polymers are transparent at low THz frequencies; when processed into compounds, their THz properties are distinctively affected by additives. In any case, the additive content can be deduced from the measured refractive index. Thus, THz-TDS was involved to measure the refractive index. In Figure. 2.16, the refractive indices are presented as a function of the volumetric additive content for different polymeric compounds, i.e., polyethylene and $Mg(OH)_2$, polypropylene and chalk, and polyamide and glass fibres. The measured refractive indices provide a reliable determination of the additive content of the material combination. Thus, THz-TDS has great potential in quality control in compounding processes.

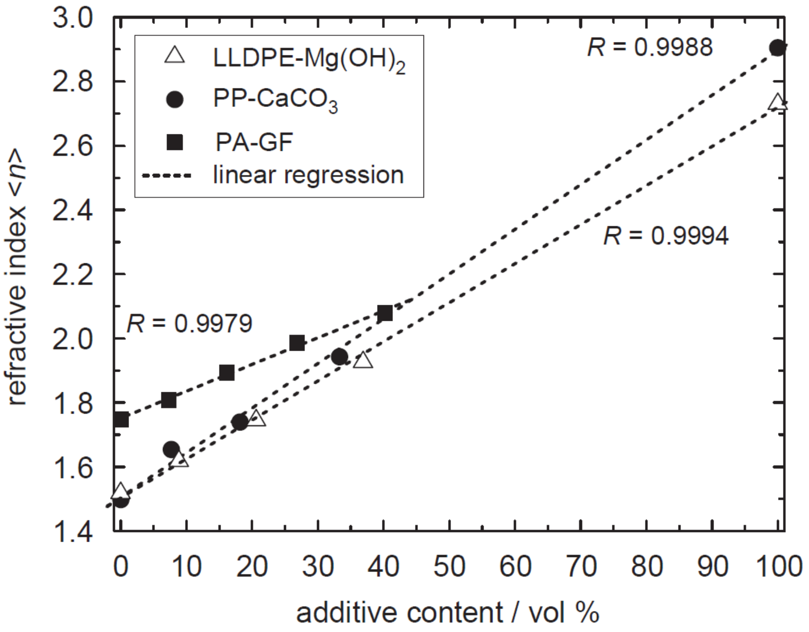

Figure. 2.16 Refractive index as a function of the volumetric additive content for different polymeric compounds. Figure adapted from [92].

C. Pharmaceutical Industry

In the pharmaceutical industry, the coating thickness and the inner structures of the solid dosages forms determine the release kinetics of the active pharmaceutical ingredient (API). If the coating is non-uniform or has any defects, then the desired dose delivery and bioavailability can be compromised [63]. Consequently, there is a critical need for measuring the coating thickness precisely and mapping and characterizing the inner structures non-destructively.

THz systems have been found to have many advantages in the pharmaceutical industry: THz waves can propagate through most of the pharmaceutical materials; many excipients and active ingredients have spectral features in the THz range; and the THz radiation is relatively safe because it is nonionizing. Therefore, based on these benefits, the potential of THz systems in the pharmaceutical industry was recently proposed by Teraview [97-101].

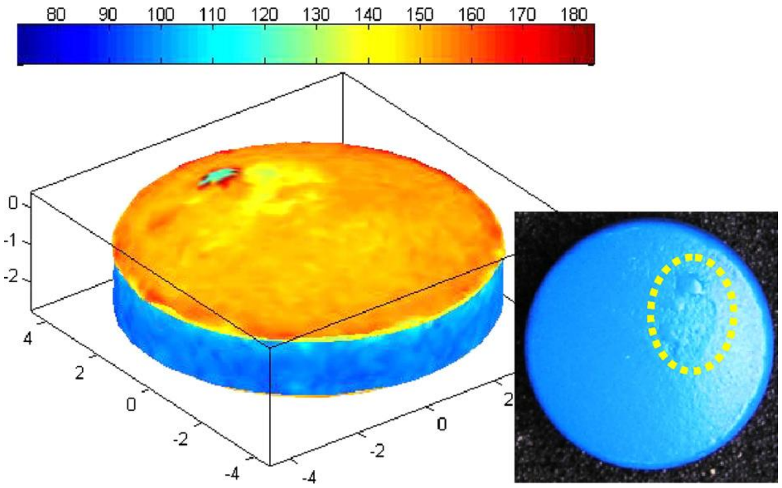

Figure. 2.17 Three-dimensional TPI false color image showing the coating thickness map of the two tablet surfaces and the central band. Color represents coating thickness, and the scale is in µm. The scales in the x, y and z directions are in mm. The inset shows the optical photograph of the same tablet where the defect areas are highlighted by a yellow ellipse. Figure adapted from [11].

As a sample, Figure. 2.17 shows the intra-tablet variation of coating thickness. Obviously, the coating thickness of the central band was thinner than that on the top and bottom surface of the tablet. Also, the coating defects, together with corresponding site, depth and size, were identified clearly. In the development of coating technology, weight gain data during coating is normally used. This approach assumes that the coated film is uniformly distributed, and evaluates the coating thickness by coating time. In Figure. 2.18, the inter-tablet variation of the coating thickness of eight tablets with the same coating time is demonstrated. Such results demonstrate that the weight gain method is not always an appropriate assumption [11]. THz systems provide a potential method to precisely measure the coating thickness and monitor the coating processes.

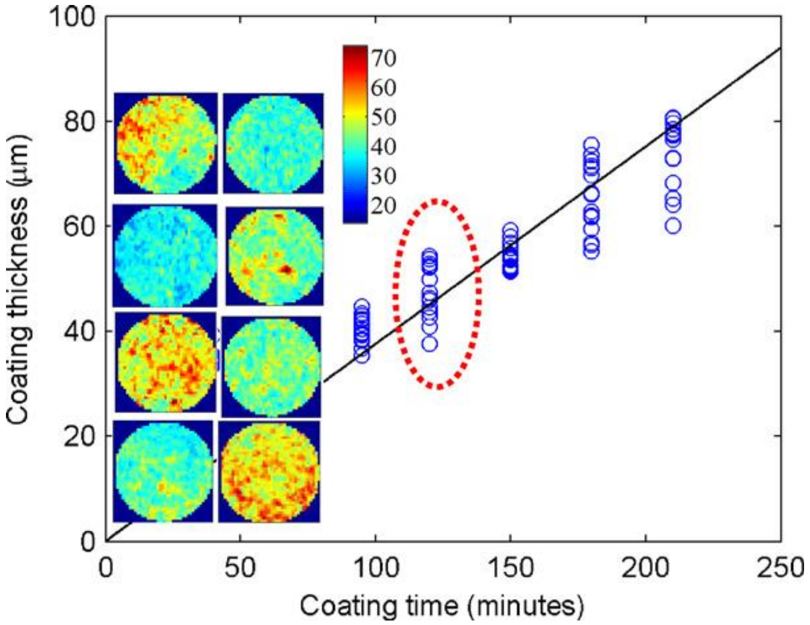

Figure. 2.18 The averaged coating thickness of each individual tablet against the coating time. The inset shows the coating thickness map (in μm) of eight tablets with the same coating time of 120 minutes. Figure adapted from [11].

D. Art Conservation

Both paintings and murals are valuable cultural heritage of mankind; they often consist of several layers as they have been painted and repainted over time. Each layer represents an artwork of a particular era. In order to discover the different layers' images, some non-destructive approaches have been used, but these have limitations such as resolution and penetration depth. Thus THz systems were developed as another potential method to use in art conservation [102-106].

Figure. 2.19 shows the first results of transmission measurements on painting [102]. The THz images were obtained using two methods: the pulse delay of the transmitted THz pulse maximum, and power transmission integrated over the different frequencies interval. This preliminary study showed that different absorption coefficients of different paints are revealed by light and dark areas, which means that, in principle, different paints can be identified. Further study, including the detection of mural paintings, was then proposed [103-106].

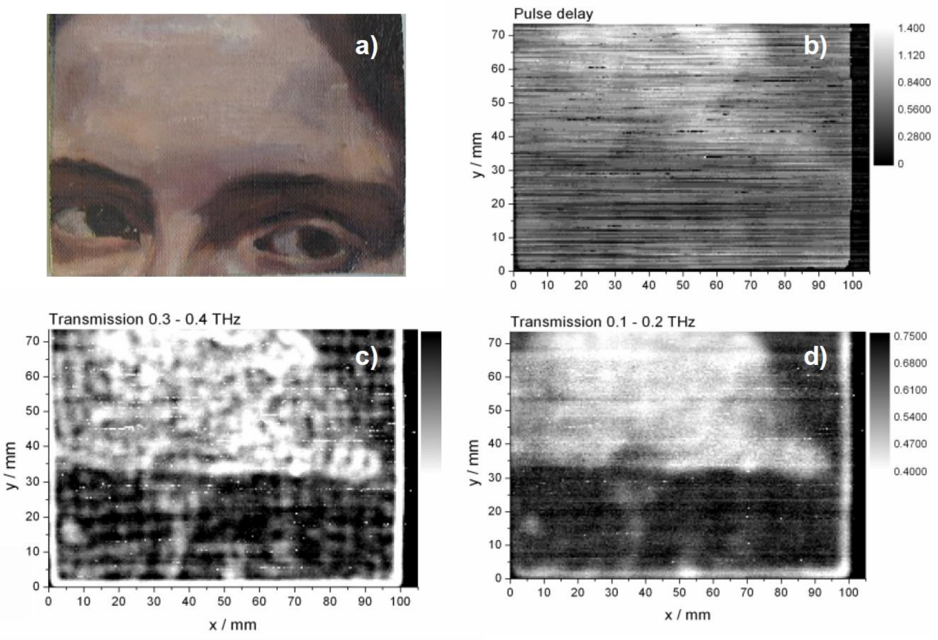

Figure. 2.19 (a) Photograph of the painting sample and corresponding THz images: (b) delay of the transmitted THz pulse maximum, and power transmission integrated over the frequency interval covering (c) 0.3-0.4 THz and (d) 0.1-0.2 THz. Figure adapted from [102].

In summary, a large variety of practical applications have been discussed for THz systems. They provide a potential and powerful method for non-destructive detection and inspection. For image acquisition in THz-TDS, the rate at which THz waveforms can be acquired is one of the key considerations because it directly determines the time for obtaining an image. Typically, a motorized stage is used to move the sample through the THz beam focus, so the image can be pixel-by-pixel required. A complete image usually takes minutes or even hours to acquire, depending on the total number of pixels and required spectral range/resolution. In both transmission TPI and reflection TPI systems, there is a trade-off between the scan range and the scan rate, which means, to a certain extent, the high scan rates limit the scan range. A short scan range not only limits the spectral resolution of measurement but also limits the range of penetrating depths through a material. Considering the need of commercial and real-time THz applications, THz systems still have some limitations, such as the slow data acquisition and high cost of hardware implementation. Therefore, there is a critical need to improve the current THz systems and develop a fast, cost-effective one to fill the industry requirements.

2.2 Compressed Sensing

Over the past few years, compressed/compressive sensing/sampling (CS) has attracted considerable attention in the research fields of applied mathematics, computer science, and electrical engineering because it can outstrip the traditional limits of sampling theory. Based on CS theory, we can represent the sparse signals using only a few non-zero coefficients in a suitable basis or dictionary. Then non-linear optimizations and algorithms can recover the signals from very few experimental measurements. Since it was introduced by Candès, Romberg, and Tao and of Donoho in 2006 [107-109], thousands of papers have been dedicated to this growing research field, including some excellent tutorials and review articles [110-118]. More references and software are listed on the website from Rice University [119].

This section reviewed the basic theory underlying CS. A brief introduction to and background of CS was followed by a discussion of the sparse signal model. After that, alternative constructions for structured CS matrices were reviewed. Then we focused on the theory and algorithms for sparse recovery; and concluded with a discussion of some extensions of the sparse recovery framework. In subsequent chapters, the CS fundamentals presented in this section will be extended to the specific emerging application, i.e., THz imaging system.

2.2.1 Background of CS

Analog to digital conversion plays a fundamental role in the digital world, and analog-to-digital converters (ADC) translate the analog information into a digital stream of numbers. These ADC devices must hold a snapshot of a fast-varying input signal for signal processing. Since the measurements are spaced in time, in general it is hard to recover the analog signal perfectly unless some prior on its structure is incorporated. After sampling, a huge amount of data has to be stored and then processed. Consequently, this requirement imposes unprecedented strains on ADC devices, powerful processors and sufficient storage devices. All conventional compression techniques are developed to discard most of the useless data we acquire without much perceptual loss. However, this still does not alleviate the numerous strains on data acquisition devices and processors. Under these circumstances, CS is proposed to merge compression and sampling, i.e., to directly measure the part that will not end up being thrown away [107].

A. Shannon-Nyquist Theorem

A common way for transferring an analog signal to a discrete representation is to assume that the signal is bandlimited, so the spectral contents are limited to a maximal frequency B. Bandlimited signals have limited time variation and can be reconstructed from equispaced samples with rate at least $2B$; this is often attributed to Shannon-Nyquist theorem [120, 121].

Such theorem can be defined as followed: If a function $x(t)$ contains no frequencies higher than B hertz, then it is completely determined by giving its ordinates at a series of points spaced $1/(2B)$ seconds apart [121]. Processing at the Nyquist rate provides a clear relation between the spectrum of $x(t)$ and that of its samples $x(nT)$; that enables the digital operations which can be substituted for their analog counterparts.

This basic principle underlies many DSP applications for estimating and detecting the analog signals. While the signal acquisition devices have been developed rapidly in the last half century, the increasingly higher rates still cannot be met constantly using available hardware. Consequently, it becomes more difficult to obtain twice the maximum frequency present in the signal. Structured analog signals can be processed more efficiently than non-structured analog signals using Shannon-Nyquist theorem. However, this reconstruction requires knowledge of the structure of the signals. Also, in many emerging applications, the rates dictated by the Shannon-Nyquist theorem are so high as to impose severe challenges on the acquisition hardware, the subsequent storage and the DSP processors. So we are interested in finding a method to recover the unknown structured signals at rates much below Nyquist.

B. Compressed Sensing

Recently, Candès, Romberg, Tao and Donoho [107-109, 111] showed the concept of CS: a signal having a sparse representation can be recovered exactly from a small set of linear measurements. An advantage of CS is to sense sparse signals by reducing the sampling rate and storage of acquisition devices. It is noted that CS differs from conventional sampling in three respects, as follows. Firstly, classical sampling theory considers continuous-time signals with infinite length. However, CS is focused on measuring finite-dimensional vectors. Secondly, in the spirit of modern sampling methods [122, 123], CS systems acquire signals by more general linear measurements, rather than sampling signals at specific points in time. Thirdly, signal recovery in the Nyquist-Shannon framework is achieved through a linear process. In contrast, signal recovery in CS is typically achieved using nonlinear methods.

CS offers a mathematical framework for simultaneous sensing and compression of finite-dimensional vectors. In CS we do not acquire this signal $x_{N\times 1}$ directly but rather acquire $M \ll N$ linear measurements $y_{M\times 1} = \Phi_{M\times N} x_{N\times 1}$ using an $M \times N$

CS sampling matrix Φ. The actual information contents of the signal determine the sampling rate, i.e., the number of M, rather than the dimensions of the space in which the signal resides. The fact that $M \ll N$ renders the solution is undetermined, but if we know $x_{N\times 1}$ is compressible by transform coding with a know transform, the data of this signal still can be acquired by M measurements. If the sample matrix Φ is well-chosen (i.e., it satisfies some properties and conditions, which will be discussed below) and a degree of reconstruction error is allowed, the number of M can dramatically smaller than N, which is usually required.

In recent years, considering CS has been developed in practical implementations for numerous applications [124-129], it is necessary to further discuss the basics of CS. Two major research areas exist [117], as follows: one area includes theory and applications related to CS sampling operators that are not random matrices and often exhibit considerable structure. The random sampling operators, which are fundamental in conventional CS theory, largely need to be optimized or replaced by other structured measurement operators that correspond to the practical application, such as imaging, sampling hardware, wireless channels and sensor networks. The other area consists of signal representations that exhibit structure beyond sparsity, such as continuous-time signals with infinite-dimensional representations. For many signals, such structure allows a higher degree of signal compression. Infinite-dimensional signal representations also show that the standard sparsity cannot easily describe the rich structure. Because reducing the sampling rate is one of the primary impetuses behind CS, it is significant to build theory that can accommodate low-dimensional signal in arbitrary Hilbert spaces (typical infinite-dimensional function spaces which are indispensable tools in the theories of Fourier analysis). Both of these areas are motivated by practical CS applications.

2.2.2 Sparse Signal Model

Signal processing focuses on acquiring, processing and extracting information from the signals. Accurate models for the signals need to be built in order to design algorithms for a particular problem. Generally, models can help distinguish the classes of interesting signals from the uninteresting signals, so the signals can be operated or analyzed efficiently and accurately. For much of classical signal processing, the signals can be modelled as vectors living in an appropriate vector space; however, such simple linear models cannot capture much of the structure present in many signals [116]. Facing these challenges, sparse signal model, one of the traditional low-dimensional models, which has particular geometrical structures, has been involved to enable signal information to be reserved via a simple linear and nonadaptive projection to a much lower dimensional space. The projection dimension is also independent of its ambient dimension [130].

We can define a signal as sparse if it can be well-approximated as a linear combination of a few elements from a proper basis and dictionary. Sparse models provide a mathematical expression for capturing the high-dimensional signals which contain relatively little information compared to their ambient dimension. Sparsity, the most prevalent signal structure used in CS, is the signal structure behind many compression algorithms. Sparsity has been exploited in signal processing applications as diverse as compression, denoising, deconvolution, restoration, and inpainting [131-137].

In general, a proper basis and dictionary can be chosen either by using a sparsifying dictionary based on a mathematical model of the data [138-144] or learning a dictionary to perform best on a training set [145-149]. The evolution of the first approach, predefined transforms, which are characterized by an analytic formulation and a fast implicit implementation, is now briefly described. Analytic dictionaries are typically formulated as tight frames, meaning that $\Phi\Phi^T x = x$ for all x, and therefore the dictionary transpose can be used to obtain a representation over the dictionary [138]. This analytical approach then proceeds by analyzing the behaviour of the filter-set $\Phi^T x$, and establishes decay rates and error bounds.

Such a tight frame approach has several advantages [138]: firstly, it is easier to analyze the behaviour of Φ^T as an analysis operator than to derive sparsity bounds in a synthesis framework. Secondly, the algorithms for both analysis and synthesis operators become reversals, simplifying algorithm design. Thirdly, such an approach produces a useful structure for both the analysis and synthesis frameworks. Due to these advantages, currently, several methods, such as discrete cosine transform (DCT), wavelets, wavelet packets, curvelets, contourlets, and bandelets, are all proposed to exploit one-dimensional and two-dimensional mathematical models for constructing effective dictionaries for signal and images [139-144].

As an example of the sparse models, a typical THz image or a THz waveform can be approximated as a sparse signal under a certain dictionary. For instance, most natural THz images are characterized by large smooth regions and relatively few sharp edges. Signals with such structure are known to be approximately sparse under DCT or wavelet transform. The lowest frequency components provide a rough scale of the image, while the high frequency components offer the details about the edge information [116]. As most of the coefficients are very small, after setting a threshold to let these small coefficients to zero, we can obtain a good approximation of sparse representation. Thus, it has a great potential to develop a CS approach to THz imaging.

2.2.3 Sensing Matrices

As discussed in the previous section, given a signal $x \in R^N$, we can represent the CS process using *M* linear measurements mathematically as

$$y_{M\times 1} = \Phi_{M\times N} x_{N\times 1}, \tag{2.16}$$

where Φ is an $M \times N$ sensing matrix and $y \in R^M$. Sensing matrix Φ aims to reduce the dimension from R^N to R^M ($M \ll N$). In CS, we assumed that the measurements are nonadaptive, that means the sensing matrices are fixed in advance. Consequently, two main questions exist: first, how to design the sensing matrix to ensure the desired information in the signal *x*? Second, how to recover the signal *x* from measurements *y*? This section considers the first question of how to design the sensing matrix. The desirable properties for the sensing matrix are presented, followed by several examples of sensing matrix constructions that satisfy these properties. The second question will be discussed in the next section.

By now, the sensing matrices should satisfy some classical properties and conditions, such as null space property (NSP), restricted isometry property (RIP), and coherence. Here, the RIP is briefly discussed; more details about these three properties and conditions can be found in other research [116].

The Restricted Isometry Property (RIP)

The NSP is sufficient for establishing guarantees; however, it is somewhat difficult to show directly, and these guarantees do not account for noise. The RIP is easier to handle and performs well with noise. Candès, Romberg and Tao introduced the RIP (initially called the uniform uncertainty principle) as a fundamental property of CS matrices [109, 145]. The isometry condition is presented as follows [146]: the restricted isometry constant δ_k of a matrix Φ is the smallest number such that

$$(1-\delta_k)\|x\|_2^2 \le \|\Phi x\|_2^2 \le (1+\delta_k)\|x\|_2^2, \tag{2.17}$$

for all $x \in \sum_k$.

A matrix Φ is said to satisfy the RIP of order *k* if constant $\delta_k \in (0,1)$ exists. By the definition RIP it is assumed that bounds that are symmetric to approximately 1 for convenience. In practice, it could be extended to be

$$\alpha\|x\|_2^2 \le \|\Phi x\|_2^2 \le \beta\|x\|_2^2, \tag{2.18}$$

where $0 < \alpha < \beta < \infty$. Giving such bounds, we can scale Φ and let it satisfy the symmetric bound about 1 in equation (2.17).

Sensing Matrix Constructions

This section will discuss how to construct matrices that satisfy the above conditions and properties. Random matrices are found to be good constructions as sensing matrices. The entries of random matrices Φ of size $M \times N$ are independent and identically distributed (i.i.d.). To a great extent, the random matrices can satisfy the RIP if the entries are chosen as a Gaussian, Bernoulli, or any sub-Gaussian distribution [145, 146]. These random constructions also make the sensing matrices that satisfy the NSP.

Using these random matrices to construct the sensing matrix has several advantages. Firstly, random matrices are democratic so it is possible to recover a signal using any sufficiently large subset of the measurements [147, 148]. Secondly, in practice we focus on the signal *x* which is often sparse to some basis or frame Ψ. That means we actually require ΦΨ to satisfy the RIP. Because the random matrices are almost incoherent with any sparse signals, in most of the cases, ΦΨ must satisfy the RIP whatever the Ψ is. Thirdly, when considered against any sparse signals, the incoherence property of random matrices requires fewer measurements using random matrices than that using other matrices' constructions. However, it also has a number of weaknesses. The full random matrix is impractical to build in hardware. Because of its unstructured property, it requires relatively more complicated computation and large storage. Currently, a number of hardware setups have been implemented to enable random measurements, such as random demodulator [149], random filtering [150], the modulated wideband converter [151], random convolution [152], and the compressive multiplexer [153].

There still exist a number of sensing matrices satisfying the RIP, such as Toeplitz and circulant matrix, Vandermonde matrix, uniform spherical matrix, random signs matrix, partial Fourier matrix, Partial Hadamard matrix, sparse projection matrix and very sparse projection matrix, and structurally random matrices. More details have been discussed in other research [154-164].

2.2.4 Signal Recovery Algorithms

Signal recovery algorithms, which recover the sparse signal $x_{N\times 1}$ from only $M \ll N$ measurements $y_{M\times 1} = \Phi_{M\times N} x_{N\times 1}$, play a fundamental role in CS theory. Basically, the signal *x* can be recovered by solving an optimization problem of ℓ_0 norm:

$$\hat{x} = \arg\min_{z} \|x\|_0 \quad s.t. \quad z \in B(y)\,, \tag{2.19}$$

where $B(y)$ ensures that $\hat{x}$ is consistent with the measurements *y*. For noise-free signals, we can set $B(y) = \{z : \Phi x = y\}$; and for noisy signals, we can instead consider $B(y) = \{z : \|\Phi x - y\|_2 \le \varepsilon\}$. Unfortunately, the function $\|\,.\,\|_0$ is nonconvex and difficult to solve. Solving problem (2.19) is both numerically unstable and non-deterministic polynomial-time (NP) hard, requiring an exhaustive enumeration of all C_N^k possible locations of the nonzero entries [160]. Currently, a minimum mean square error (MMSE) linear estimation and a number of nonlinear algorithmic approaches such as ℓ_1 minimization algorithms, greedy algorithms, and total-variation minimization (TV-min) algorithms, have been proposed to solve this optimization problem.

A. MMSE Linear Estimation

As discussed, the CS process using M linear measurements can be presented mathematically as $y_{M\times1} = \Phi_{M\times N} x_{N\times1}$. Reconstructed images can be obtained by the MMSE linear estimation [165, 166]. MMSE estimation describes the approach which minimizes the mean square error. It refers to estimation in a Bayesian setting with quadratic cost function. The reconstruction matrix $\hat{\Phi}_{N\times M}$ according to $\hat{x}_{N\times1} = \hat{\Phi}_{N\times M} y_{M\times1}$ can be written as

$$\hat{\Phi} = R_{xx}\Phi^T(\Phi R_{xx}\Phi^T)^{-1}, \tag{2.20}$$

where R_{xx} represents the autocorrelation function of the input signal. For nature images, we approximate R_{xx} using the autoregressive model of order 1 (AR(1) model) with correlation coefficient $\rho = 0.95$. MMSE linear estimation is a fast reconstruction algorithm, however it is impossible to achieve high quality image reconstruction by using this algorithm. The reconstructed image is not that clear when recovering the complex image with many sharps. Generally, the natural image can be easily reconstructed and recognized by using the MMSE linear estimation. If we aim to achieve high quality reconstruction, we have to use other nonlinear reconstruction algorithms. The following sections provides a discussion of how to further improve the quality of the reconstructed images by using other nonlinear reconstruction algorithms.

B. l_1 Minimization Algorithms

The use of ℓ_1 minimization first appears in the Ph.D. thesis of B. Logan [167] in connection with sparse frequency estimation. In 1992, the earliest theoretical work on sparse recovery using ℓ_1 minimization was reported by Donoho and Logan. The optimization problem of ℓ_0 norm can be solved more tractable by replacing $\| . \|_0$ with its convex approximation $\| . \|_1$. Thus, we consider the optimization based on the ℓ_1 norm:

$$\hat{x} = \underset{z}{\operatorname{argmin}} \|x\|_1 \quad s.t. \quad z \in B(y)\,. \tag{2.21}$$

From [139, 168], problem (2.19) has been proved to be equivalent to problem (2.21). Surprisingly, optimization based on the ℓ_1 norm can recover the *k*-space signals fully and approximate the compressible signals with high probability using only $M \geq Ck\log(N/k)$ i.i.d. Gaussian measurements [107, 108].

A number of algorithms designed to solve the problem (2.21) are also present, such as interior-point method [169], gradient projection [170] method and homotopy method [171]. Comparatively speaking, the interior-point method provides accurate recovery, whereas its computation speed is slow; gradient projection has relatively great computation speed; and homotopy method is practical for small-scale problems. Furthermore, reweighted ℓ_1 algorithm is proposed to reduce the effect from measurement noise on the reconstruction algorithms [172].

C. Greedy Algorithms

There also exists a variety of greedy/iterative methods for computing sparse representations [173-181]. Greedy algorithms rely on iterative approximation of the signal coefficients and support, either by iteratively recognizing the support of the signal until a convergence criterion is met, or alternatively by acquiring an improved estimate of the sparse signal at each iteration that attempts to account for the mismatch to the measured data [116]. Two of the most common greedy methods are Orthogonal Matching Pursuit (OMP) and iterative thresholding. More details about these two algorithms were presented in various research [116, 182-184].

D. Total-Variation Minimization Algorithms

The use of total-variation minimization (TV-min), which is closely connected to ℓ_1 minimization, first appears in 1990 by Rudin, Osher and Fatemi [185]. Compared with ℓ_1 minimization, which is suitable for one-dimensional signal recovery, TV-min has been proposed to recover two-dimensional images [108]. Briefly, the optimization of TV norm is given as

$$\min \|x\|_{TV} \quad s.t. \;\; y = \Phi x, \tag{2.22}$$

where $\|x\|_{TV}$ is the TV norm of a two-dimensional object *x*. For discrete data $x(t_1, t_2)$, $0 \le t_1, t_2 \le N-1$,

$$\|x\|_{TV} = \sum_{t_1, t_2} \sqrt{\left|D_1 x(t_1, t_2)\right|^2 + \left|D_2 x(t_1, t_2)\right|^2}\,, \tag{2.23}$$

where D_1 is the finite difference $D_1 x = x(t_1, t_2) - x(t_1 - 1, t_2)$ and $D_2 x = x(t_1, t_2) - x(t_1, t_2 - 1)$. The TV-min problem can be recast as special convex programs known as second order cone programs (SOCPs) [108, 186]. Generally speaking, TV-min can offer accurate and robust reconstructed results by recovering two-dimensional images synchronously, with relatively slow computation speed.

Basically, the MMSE linear estimation and the TV-min nonlinear reconstruction algorithm were mainly used in our experiments. The MMSE linear estimation is used in fast compressed imaging as its corresponding computational time is relatively short, so it can be used in real time imaging processing. And the TV-min nonlinear reconstruction algorithm is used for high quality image reconstruction. It is the most popular method for non-linear reconstruction of 2D images. For other methods, like OMP, it is time consuming and the result is not as good as that of the TV-min [116].

2.2.5 CS Imaging Applications

CS has a wide range of applications to imaging, such as the optical single-pixel camera, tomography, digital holography, spectral imaging, geophysical imaging, and medical imaging (including magnetic resonance imaging (MRI)), and photo-acoustic imaging [108, 125, 187-193]. Here we discuss some of these CS imaging application highlights. All these CS imaging systems have impressive advantages, such as great imaging acquisition efficiency and simple hardware implementation.

A. Single-Pixel Camera

The optical single-pixel camera architecture employs a digital micro-mirror array to perform optical calculations of linear projections of an image onto pseudorandom binary patterns [108, 187]. As shown in Figure. 2.20, the incident light is reflected by the sample and then formed on the digital micro-mirror device (DMD) array, whose mirror orientations are modulated in the pseudorandom pattern supplied by the random number generators (RNG). Finally, the light is focused onto the photodiode for reconstruction and processing. An image can be obtained while sampling the image fewer times than the number of pixels. It is noted that this system relies on a single-pixel photodiode for detection rather than a CCD or CMOS array. Thus, CS provides the implementation of such an imaging system with simpler and less expensive hardware.

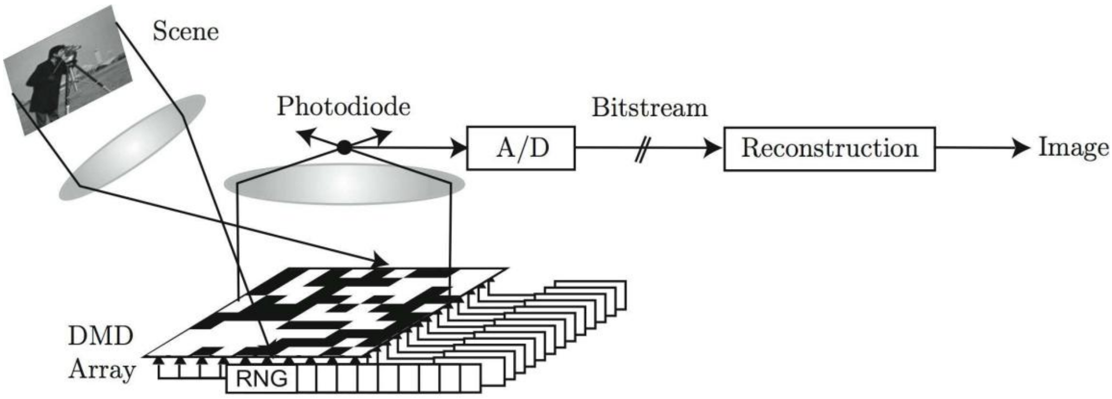

Figure. 2.20 Schematic diagram of single-pixel camera. The incident light is reflected by the sample and then formed on the digital micro-mirror device (DMD) array whose mirror orientations are

modulated in the pseudorandom pattern supplied by the random number generators (RNG). Finally, the light is focused onto the photodiode for reconstruction and processing. Figure adapted from [187].

B. Digital Holography

Digital holography is a computational imaging from electronically recorded holograms using electronic detector arrays [188]. Traditional digital holography is not regarded as a 3D tomographic approach because the 3D object estimation from the data is underdetermined. Using the CS approach, the compressive holography enables 3D tomography from a single 2D monochromatic digital holography. The results and more details were presented in various research [188].

C. Spectral Imaging

Spectral imaging is a powerful tool for a variety of applications because it provides the nature of the materials. Conventional spectral imaging is slow because of a trade-off between spatial resolution, spectral resolution, light collection, and measurement acquisition time. Based on the concept of CS, a novel single-shot compressive spectral imaging system was developed to eliminate this trade-off [189]. The main features of the system design are two dispersive elements, arranged in opposition and surrounding a binary-valued aperture code. Such structure results in spatially-varying, easily-controllable, spectral filter functions with narrow features [189].

D. Magnetic Resonance Imaging (MRI)

Imaging speed is important in many MRI applications and it is mainly limited by physical (gradient amplitude and slew-rate) and physiological (nerve stimulation) constraints [192]. Aiming to exploit the sparsity which is implicit in MR images, the researchers developed CS based implementation for rapid MRI. Several implementations for 2D and 3D Cartesian imaging (most of the current product pulse sequences in the clinic are Cartesian) were demonstrated. It was shown that the sparsity of MR images can be exploited to significantly reduce scan time or improve the spatial resolution. More details about the experimental implementations and corresponding results were proposed in various research [192].

References:

[1] D. H. Auston and K. P. Cheung, "Coherent time-domain far-infrared spectroscopy," *J. Opt. Soc. Am. B,* vol. 2, no. 4, pp. 606-612, 1985.

[2] P. R. Smith, D. H. Auston, and M. C. Nuss, "Subpicosecond photoconducting dipole antennas," *IEEE J. Quant. Elec.*, vol. 24, no. 2, pp. 255-260, 1988.

[3] C. Fattinger and D. Grischkowsky, "Terahertz beams," *Appl. Phys. Lett.*, vol. 54, no. 6, pp. 490, 1989.

[4] M. V. Exter, C. Fattinger, and D. Grischkowsky, "Terahertz time-domain spectroscopy of water vapor," *Opt. Letts.*, vol. 14, no. 20, pp. 1128-1130, 1989.

[5] B. B. Hu and M. C. Nuss, "Imaging with terahertz waves," *Opt. Lett.*, vol. 20, no. 16, pp. 1716-1719, 1995.

[6] D. M. Mittleman, R. H. Jacobsen, and M. C. Nuss, "T-ray imaging," *IEEE Set Top. Quant. Elec,* vol. 2, pp. 679-692, 1996.

[7] J. D. Kafka, M. L. Watts, and J. W. J. Pieterse, "Picosecond and femtosecond pulse generation in a regeneratively mode-locked Ti:sapphire laser," *IEEE J. Quantum Electronics*, vol. 28, no. 10, pp. 2151-2162, 1992.

[8] G. P. Gallerano and S. Biedron, "Overview of terahertz radiation sources," *26th International Free Electron Laser (FEL) Conference*, Trieste, Italy, 2004.

[9] P. U. Jepsen, D. G. Cooke, and M. Koch, "Terahertz spectroscopy and imaging - Modern techniques and applications," *Laser Photonics*, vol. 5, no. 1, pp. 124-166, 2010.

[10] D. H. Auston, "Picosecond optoelectronic switching and gating in silicon," *Appl. Phys. Lett.*, vol. 26, no. 3, pp. 101-103, 1975.

[11] Y. C. Shen, "Terahertz pulsed spectroscopy and imaging for pharmaceutical applications: A review," *Int. J. Pharm.*, vol. 417, no. 1-2, pp. 48-60, 2011.

[12] P. U. Jepsen, R. H. Jacobsen, and S. R. Keiding, "Generation and detection of terahertz pulses from biased semiconductor antennas," *J. Opt. Soc. Am. B,* vol. 13, no. 11, pp. 2424-2436, 1996.

[13] D. W. Faries, K. A. Gehring, P. L. Richards, and Y. R. Sheen,"Tuneable Far-Infrared Radiation Generated from the Difference Frequency between Two Ruby Lasers," *Phys. Rev.*, vol. 180, no.2, pp. 363-365, 1969.

[14] L. Xu, X. C. Zhang, and D. H. Auston, "Terahertz beam generation by femtosecond optical pulses in electro-optic materials," *Appl. Phys. Lett.*, vol. 61, no. 15, pp. 1784-1786, 1992.

[15] Q. Wu and X. C. Zhang, "Free-space electro-optic sampling of terahertz beams," *Appl. Phys. Lett.*, vol. 67, no. 24, pp. 3523-3525, 1995.

[16] Q. Wu and X. C. Zhang, "Ultrafast electro-optic field sensors," *Appl. Phys. Lett.*, vol. 68, no. 12, pp. 1604-1606, 1996.

[17] G. Gallot, J. Q. Zhang, R.W. McGowan, T. I. Jeon, and D. Grischkowsky, "Measurements of the THz absorption and dispersion of ZnTe and their relevance to the electro-optic detection of THz radiation," *Appl. Phys. Lett.*, vol. 74, no. 23, pp. 3450, 1999.

[18] Q. Wu and X. C. Zhang, "7 terahertz broadband GaP electro-optic sensor," *Appl. Phys. Lett.*, vol. 70, no. 14, pp. 1784-1786, 1997.

[19] P. Y. Han and X. C. Zhang, "Coherent, broadband midinfrared terahertz beam sensors," *Appl. Phys. Lett.*, vol. 73, no. 21, pp. 3049-3051, 1998.

[20] R. Huber, A. Brodschelm, F. Tauser, and A. Leitenstorfer, "Generation and field-resolved detection of femtosecond electromagnetic pulses tuneable up to 41 THz," *Appl. Phys. Lett.*, vol. 76, no. 22, pp. 3191-3193, 2000.

[21] C. Kübler, R. Huber, S. Tubel, and A. Leitenstorfer, "Ultrabroadband detection of multi-terahertz field transients with GaSe electro-optic sensors: Approaching the near infrared," *Appl. Phys. Lett.*, vol. 85, no. 16, pp. 3360-3362, 2004.

[22] D. J. Cook and R. M. Hochstrasser, "Intense terahertz pulses by four-wave rectification in air," *Opt. Lett.*, vol. 25, no. 16, pp. 1210-1212, 2000.

[23] T. Löffler, F. Jacob, and H. G. Roskos, "Generation of terahertz pulses by photoionization of electrically biased air," *Appl. Phys. Lett.*, vol. 77, no. 3, pp. 453-455, 2000.

[24] J. Dai, X. Xie, and X. C. Zhang, "Detection of Broadband Terahertz Waves with a Laser-Induced Plasma in Gases," *Phys. Rev. Lett.*, vol. 97, no. 10, 103903, 2006.

[25] I. S. Gregory, C. Baker, W. R. Tribe, I. V. Bradley, M. J. Evans, E. H. Linfield, A. G. Daives, and M. Missous, "Optimization of photomixers and antennas for continuous-wave terahertz emission," *IEEE J. Quantum Electronics*, vol. 41, no. 5, pp. 717-728, 2005.

[26] S. Verghese, K. A. McIntosh, S. Calawa, W. F. Dinatale, E. K. Duerr, and K. A. Molvar, "Generation and detection of coherent terahertz waves using two photomixers," Appl. Phys. Lett., vol. 73, no. 26, pp. 3824-3826, 1998.

[27] M. Tani, S. Matsuura, K. Sakai, and M. Hangyo, "Multiple-frequency generation of sub-terahertz radiation by multimode ld excitation of photoconductive antenna," *IEEE Microwave Guided Wave Lett.*, vol. 7, no. 9, pp. 282-284, 1997.

[28] E. R. Brown, K. A. McIntosh, K. B. Nichols, and C. L. Dennis, "Photomixing up to 3.8 THz in low-temperature-grown GaAs," *Appl. Phys. Lett.*, vol. 66, no. 3, pp. 285-287, 1995.

[29] R. Wilk, F. Breitfeld, M. Mikulics, and M. Koch, “Continuous wave terahertz spectrometer as a noncontact thickness measuring device,” *Appl. Opt.*, vol. 47, no. 16, pp. 3023-3026, 2008.

[30] A. Dobroiu, M. Yamashita, Y. N. Ohshima, Y. Morita, C. Otani, and K. Kawase, "Terahertz imaging system based on a backward-wave oscillator," *Appl. Opt.*, vol. 43, no. 30, pp. 5637-5646, 2004.

[31] B. Ferguson and X. C. Zhang, "Materials for terahertz science and technology," *Nature Materials*, vol. 1, no. 1, pp. 26-33, 2002.

[32] R. Kohler, A. Tredicucci, F. Beltram, H. E. Beere, E. H. Linfield, A. G. Davis, D. A. Davis, D. A. Ritchie, R. C. Lotti, and F. Rossi, "Terahertz semiconductor-heterostructure laser," *Nature*, vol. 417, no. 6885, pp. 156-159, 2002.

[33] A. Wade, G. Fedorov, D. Smirnov, S. Kumar, B. S. Williams, Q. Hu, and J. L. Reno, "Magnetic-field-assisted terahertz quantum cascade laser operating up to 225K," *Nature Photonics*, vol. 3, no. 1, pp. 41-45, 2009.

[34] N. Jukam, S. S. Dhillon, D. Oustinov, J. Madeo, C. Manquest, S. Barbieri, C. Sirtori, S. P. Khanna, E. H. Linfield, A. G. Davies, and J. Tignon, "Terahertz amplifier based on gain switching in a quantum cascade laser," *Nature Photonics*, vol. 3, no. 12, pp. 715-719, 2009.

[35] G. P. Williams, "Far-IR/THz radiation from the Jefferson Laboratory, energy recovered linac, free eletron laser," *Rev. Sci. Instrum.*, vol. 73, no. 3, pp. 1461-1463, 2002.

[36] A. C. Warren, J. M. Woodall, J. L. Freeouf, D. Grischkowsky, D. T. McInturff, M. R. Melloch, and N. Otsuka, "Arsenic precipitates and the semi-insulating properties of GaAs buffer layers grown by low-temperature molecular beam epitaxy," *Appl. Phys. Lett.*, vol. 57, no. 13, 1331-1333, 1990.

[37] S. Gupta, M. Y. Frankel, J. A. Valdmanis, J. F. Whitaker, G. A. Mourou, F. W. Smith, and A. R. Calawa, "Subpicosecond carrier lifetime in GaAs grown by molecular beam epitaxy at low temperatures," *Appl. Phys. Lett.*, vol. 59, no. 25, pp. 3276-3278, 1991.

[38] S. Gupta, J. F. Whitaker, and G. A. Mourou, "Ultrafast carrier dynamics in III-V semiconductors grown by molecular-beam epitaxy at very low substrate temperatures," *IEEE J. Quantum Electronics*. vol. 28, no. 10, pp. 2464-2472, 1992.

[39] I. S. Gregory, C. Baker, W.R. Tribe, M. J. Evans, H. E. Beere, E. H. Linfield, A. G. Davies, and M. Missous, "High resistivity annealed low-temperature GaAs with 100 fs lifetimes," *Appl. Phys. Lett.*, vol. 83, no. 20, pp. 4199-2401, 2003.

[40] J. Sigmund, C. Sydlo, H. L. Hartnagel, N. Benker, H. Fuess, F. Rutz, T. Kleine-Ostmann, and M. Koch, "Structure investigation of low-temperature-grown GaAsSb, a material for photoconductive terahertz antennas," *Appl. Phys. Lett.*, vol. 87, no. 25, 252103, 2005.

[41] C. Baker, I. S. Gregory, W. R. Tribe, I. V. Bradley, M. J. Evans, E. H. Linfield, and M. Missous, "Highly resistive annealed low-temperature-grown InGaAs with sub-500 fs carrier lifetimes," *Appl. Phys. Lett.*, vol. 85, no. 21, pp. 4965-4967, 2004.

[42] B. Sartorius, H. Roehle, H. Künzel, J. Böttcher, M. Schlak, D. Stanze, H. Venghaus, and M. Schell, "All-fiber terahertz time-domain spectrometer operating at 1.5 µm telecom wavelengths," *Opt. Express*, vol. 16, no. 13, pp. 9565-9570, 2008.

[43] H. Roehle, R. J. B. Dietz, H. J. Hensel, J. Böttcher, H. Künzel, D. Stanze, M. Schell, and B. Sartorius, "Next generation 1.5 µm terahertz antennas: mesa-structuring of InGaAs/InAlAs photoconductive layers," *Opt. Express*, vol. 18, no. 3, pp. 2296-2301, 2010.

[44] M. Suzuki and M. Tonouchi, "Fe-implanted InGaAs photoconductive terahertz detectors triggered by 1.56 µm femtosecond optical pulses," *Appl. Phys. Lett.*, vol. 86, no. 16, 163504, 2005.

[45] M. Suzuki and M. Tonouchi, "Fe-implanted InGaAs terahertz emitters for 1.56 μm wavelength excitation," *Appl. Phys. Lett.*, vol. 86, no. 5, 051104, 2005.

[46] N. Chimot, J. Mangeney, L. Joulaud, P. Crozat, H. Bernas, K. Blary, and J. F. Lampin, "Terahertz radiation from heavy-ion-irradiated $In_{0.53}Ga_{0.47}As$ photoconductive antenna excited at 1.55 μm," *Appl. Phys. Lett.*, vol. 87, no. 19, 193510, 2005.

[47] F. Sizov and A. Rogalski, "THz detectors," *Prog. Quant. Elec.*, vol. 34, no. 5, pp. 278-347, 2010.

[48] B. S. Karasik, D. Olaya, J. Wei, S. Pereverzev, M. E. Gershenson, J. H. Kawamura, W. R. McGrath, and A. V. Sergeev, "Record-low NEP in hot-eletron titaium nanobolometers," *IEEE Trans. Appl. Supercond.*, vol. 17, no. 2, pp. 293-297, 2007.

[49] E. H. Putley, "Thermal detectors," in: R.J. Keyes (Ed.), Optical and Infrared Detectors, Springer, Berlin, Germany, 1977.

[50] M. C. Gaidis, H. M. Pickett, C. D. Smith, S. C. Martin, R. P. Smith, and P. H. Siegel, "A 2.5 THz receiver front-end for spaceborne applications," *IEEE Trans. Microwave Theory Technol.*, vol. 48, no. 4, pp. 733-739, 2000.

[51] G. J. Dolan, T. G. Phillips, and D. P. Woody, "Low-noise 115-GHz mixing in superconducting oxide-barrier tunnel junctions, " *Appl. Phys. Lett.*, vol. 34, no. 5, pp. 347-349, 1979.

[52] J. E. Carlstrom, and J. Zmuidzinas, "Reviews of Radio Science," in: W. R. Stone (Ed), Oxford Univ. Press, Oxford, UK, 1996.

[53] D. Mittleman, "Sensing with Terahertz Radiation," Springer Series in Optical Sciences, Heidelberg, Springer, 2002.

[54] M. V. Exter, and D. R. Grischkowsky, "Characterization of an optoelectronic terahertz beam system," *IEEE Trans. Microw. Theory Tech.*, vol. 38, no. 11, pp. 1684-1691, 1990.

[55] P. U. Jepsen, R. H. Jacobsen, and S. R. Keiding, "Generation and detection of terahertz pulses from biased semiconductor antennas," *J. Opt. Soc. Am. B*, vol. 13, no. 11, pp. 2424-2436, 1996.

[56] P. Y. Han and X. C. Zhang, "Free-space coherent broadband terahertz time-domain spectroscopy," *Meas. Sci. Technol.*, vol. 12, no. 11, pp. 1747-1756, 2001.

[57] W. L. Chan, J. Deibel, and D. M. Mittleman, "Imaging with terahertz radiation," *Rep. Prog. Phys.*, vol. 70, no. 8, pp. 1325-1379, 2007.

[58] T. I. Jeon and D. Grischkowsky, "Characterization of optically dense, doped semiconductors by reflection THz time domain spectroscopy," *Appl. Phys. Lett.*, vol. 72, no. 23, pp. 3032-3034, 1998.

[59] L. Thrane, R. H. Jacobsen, P. U. Jepsen, and S. R. Keiding, "THz reflection spectroscopy of liquid water," *Chem. Phys. Lett.*, vol. 240, no. 4, pp. 330-333, 1995.

[60] Y. C. Shen and P. F. Taday, "Development and application of terahertz pulsed imaging for nondestructive inspection of pharmaceutical tablet," *IEEE Set Top. Quant. Elec.*, vol. 14, no. 2, pp. 407-415, 2008.

[61] M. Nagai, H. Yada, T. Arikawa, and K. Tanaka, "Terahertz time-domain attenuated total reflection spectroscopy in water and biological solution," *Int. J. Infrared Millim. Waves.*, vol. 27, no. 4, pp. 505-515, 2006.

[62] H. Hirori, K. Yamashita, M. Nagai, and K. Tanaka, "Attenuated Total Reflection Spectroscopy in Time Domain Using Terahertz Coherent Pulses," *Jpn. J. Appl. Phys. 2, Lett.*, vol. 43, no. 10A, pp. L1287-L1289, 2004.

[63] D. A. Newnham, P. F. Taday, "Pulsed terahertz attenuated total reflection spectroscopy," *Appl. Spectro.*, vol. 62, no. 4, pp. 394-398, 2008.

[64] H. Hirori, M. Nagai, and K. Tanaka, "Destructive interference effect on surface plasmon resonance in terahertz attenuated total reflection," *Opt. Express*, vol. 13, no. 26, pp. 10801-10814, 2005.

[65] H. Yada, M. Nagai, and K. Tanaka, "The intermolecular stretching vibration mode in water isotopes investigated with broadband terahertz time-domain spectroscopy," *Chem. Phys. Lett.*, vol. 473, no. 4-6, pp. 279-283, 2009.

[66] H. Yada, M. Nagai, and K. Tanaka, "Origin of the fast relaxation component of water and heavy water revealed by terahertz time-domain attenuated total reflection spectroscopy," *Chem. Phys. Lett.*, vol. 464, no. 4-6, pp. 166-170, 2008.

[67] T. Arikawa, M. Nagai, and K. Tanaka, "Hydration structures of 2-butoxyethanol monomer and micelle in solution," *Chem. Phys. Lett.*, vol. 477, no. 1-3, pp. 95-101, 2009.

[68] D. Grischkowsky, S. Keiding, M. V. Exter, and C. Fattinger, "Far-infrared time-domain spectroscopy with terahertz beams of dielectrics and semiconductors," *J. Opt. Soc. Am. B*, vol. 7, no. 10, pp. 2006-2015, 1990.

[69] L. Duvillaret, F. Garet, and J. L. Coutaz, "A reliable method for extraction of material parameters in terahertz time-domain spectroscopy," *IEEE J. Sel. Top. Quantum Electron.*, vol. 2, no. 3, pp. 739-746, 1996.

[70] L. Duvillaret, F. Garet, and J. L. Coutaz, "Highly precise determination of optical constants and sample thickness in terahertz time-domain spectroscopy," *Appl. Optics.*, vol. 38, no. 2, pp. 409-415, 1999.

[71] P. Y. Han, M. Tani, M. Usami, S. Kono, R. Kersting and X. C. Zhang, "A direct comparison between terahertz time-domain spectroscopy and far-infrared Fourier transform spectroscopy," *J. Applied Physics*, vol. 89, no. 4, pp. 2357-2359, 2001.

[72] P. U. Jepsen and B. M. Fischer, "Dynamic range in terahertz time-domain transmission and reflection spectroscopy," *Opt. Lett.*, vol. 30, no. 1, pp. 29-31, 2005.

[73] V. P. Wallace, E. MacPherson, J. A. Zeitler, and C. Reid, "Three-dimensional imaging of optically opaque materials using nonionizing terahertz radiation," *J. Opti. Soc. Am. Aopti. Img. Sci. Vis.*, vol. 25, no. 12, pp. 3120-3133, 2008.

[74] R. P. Cogdill, R. N. Forcht, Y. C. Shen, P. F. Taday, J. R. Creekmore, C. A. Anderson, and J. K. Drennen III, "Comparison of terahertz pulse imaging and near-infrared spectroscopy for rapid non-destructive analysis of tablet coating thickness and uniformity," *J. Pharm. Innov.*, vol. 2, no. 1-2, pp. 29-36, 2007.

[75] Y. C. Shen, S. Y. Zhang, and Y. S. Jiang, "Angular resonance absorption spectra of Langmuir-Blodgett films studied by the photoacoustic techinique," *Thin Solid Films*, vol. 248, no. 1, pp. 36-40, 1994.

[76] W. T. Silfvast, "Laser fundamentals," 2nd ed. Cambridge Univ. Press. pp. 9-39, Cambridge, U.K., 2004.

[77] D. M. Mittleman, M. Gupta, R. Neelamani, R. G. Barniuk, J. V. Rudd, and M. Koch, "Recent advances in terahertz imaging," *Appl. Phys. B.*, vol. 68, no. 6, pp. 1085-1094, 1999.

[78] A. W. M. Lee, Q. Qin, S. Kumar, B. S. Williams, Q. Hu, and J. L. Reno, "Real-time terahertz imaging over a standoff distance (>25 meters)," *Appl. Phys. Lett.*, vol. 89, no. 14, 141125, 2006.

[79] Z. Jiang and X. C. Zhang, "Terahertz imaging via electrooptic effect," *IEEE Trans. Microwave Th. Tech.*, vol. 47, no. 12, pp. 2644-2650, 1999.

[80] J. Pearce, H. H. Choi, D. M. Mittleman, J. White, and D. Zimdars, "Terahertz wide aperture reflection tomography," *Opt. Lett.*, vol. 30, no. 13, pp. 1653-1655, 2005.

[81] S. Wang and X. Zhang, "Pulsed terahertz tomography," *J. Phys. D: Appl. Phys.*, vol. 37, no. 4, pp. 964 (R31-R36), 2004.

[82] A. Bandyopadhyay, A. Stepanov, B. Schulkin, M. D. Federici, A. Sengupta, D. Gary, J. F. Federici, R. Barat, Z. H. Michalopoulou, and D. Zimdars, "Terahertz interferometric and synthetic aperture imaging," *J. Opt. Soc. Am. A*, vol. 23, no. 5, pp. 1168-1178, 2006.

[83] Z. P. Jiang and X. C. Zhang, "Single-shot spatiotemporal terahertz field imaging," *Opt. Lett.*, vol. 23, no. 14, pp. 1114-1116, 1998.

[84] A. Nahata, J. T. Yardley, and T. F. Heinz, "Free-space electro-optic detection of continuous-wave terahertz radiation," *Appl. Phys. Lett.*, vol. 75, no. 17. pp. 2524-2526, 1999.

[85] A. Nahata, J. T. Yardley, and T. F. Heinz, "Two-dimensional imaging of continuous-wave terahertz radiation using electro-optic detection," *Appl. Phys. Lett.*, vol. 81, no. 6, pp. 963-965, 2002.

[86] T. Kleine-Ostmann, P. Knobloch, M. Koch, S. Hoffmann, M. Breede, M. Hofmann, G. Hein, K. Pierz, M. Sperling, and K. Donhuijsen, "Continuous-wave THz imaging," *Electron. Lett.*, vol. 37, no. 24, pp. 1461-1463, 2001.

[87] Y. C. Shen, T. Lo, P. F. Taday, B. E. Cole, W. R. TYibe, and M. C. Kemp, "Detection and identification of explosives using terahertz pulsed spectroscopic imaging," *Appl. Phys. Lett.*, vol. 86, no. 24, 241116, 2005.

[88] H. B. Liu, Y. Chen, G. J. Bastiaans, and X. C. Zhang, "Detection and identification of explosive RDX by THz diffuse reflection spectroscopy," *Opt. Express*, vol. 14, no. 1, pp. 415-423, 2006.

[89] N. Karpowicz, H. Zhong, C. Zhang, K. I. Lin, J. S. Hwang, J. Xu, and X. C. Zhang, "Compact continuous-wave subterahertz system for inspection applications," *Appl. Phys. Lett.*, vol. 86, no. 5, 054105, 2005.

[90] K. Kawase, Y. Ogawa, and Y. Watanabe, and H. Inoue, "Non-destructive

terahertz imaging of illicit drugs using spectral fingerprints," *Opt. Express*, vol. 11, no. 20, pp. 2549-2554, 2003.

[91] D. Zimdars, J. S. White, G. Stuk, A. Chernovsky, G. Fichter, and S. Williamson, "Large area terahertz imaging and non-destructive evaluation application," *Insight*, vol. 48, no. 9, pp.537-539, 2006.

[92] S. Wietzke, C. Jansen, F. Rutz, D. M. Mittleman, and M. Koch, "Determination of additive content in polymeric compounds with terahertz time-domain spectroscopy," *Polym. Testing*, vol. 26, no. 5, pp. 614-618, 2007.

[93] N. Krumbholz, T. Hochrein, N. Vieweg, T. Hasek, K. Kretschmer, M. Bastian, M. Mikulics, and M. Koch, "Monitoring polymeric compounding processes inline with THz time-domain spectroscopy," *Polym. Testing*, vol. 28, no. 1, pp. 30-35, 2009.

[94] S. Wietzke, C. Jordens, N. Krumbholz, M. Koch, B. Baudrit, and M. Bastian, "Terahertz imaging: a new non-destructive technique for the quality control of plastic weld joints," *J. Eur. Opt. Soc. Rapid Public*, vol. 2, pp. 07013, 2007.

[95] C. Jansen, S. Wietzke, O. Peters, M. Scheller, N. Vieweg, M. Salhi, N. Krumbholz, C. Jordens, T. Hochrein, and M. Koch, "Terahertz imaging: applications and perspectives," *Appl. Opt.*, vol. 49, no. 19, pp. E48-E57, 2010.

[96] F. Rutz, M. Koch, S. Khare, M. Moneke, H. Richter, and U. Ewert, "Terahertz quality control of polymeric products," *Int. J. Infrared Millim. Waves*, vol. 27, no. 4, pp. 547-556, 2006.

[97] P. F. Taday, "Applications of terahertz spectroscopy to pharmaceutical sciences," *Philos. Trans. R. Soc. Lond. A, Math. Phys. Eng. Sci.*, vol. 362, no. 1815, pp. 351-362, 2004.

[98] P. F. Taday, I. V. Bradley, D. D. Arnone, and M. Pepper, "Using terahertz pulse spectroscopy to study the crystalline structure of a drug: A case study of the polymorphs of ranitidine hydrochloride," *J. Pharma. Sci.*, vol. 92, no. 4, pp. 831-838, 2003.

[99] J. A. Zeitler, K. Kogermann, J. Rantanen, T. Rades, P. F. Taday, M. Pepper, J. Aaltonen, and C. J. Strachan, "Drug hydrate systems and dehydration processes studied by terahertz pulsed spectroscopy,” *Int. J. Pharm.*, vol. 334, no. 1-2, pp. 78-84, 2007.

[100] A. J. Fitzgerald, B. E. Cole, and P. F. Taday, "Nondestructive analysis of tablet coating thicknesses using terahertz pulsed imaging," *J. Pharma. Sci.*, vol. 94, no. 1, pp. 177-183, 2005.

[101] J. A. Spencer, Z. Gao, T. Moore, L. F. Buhse, P. F. Taday, D. A. Newnham, Y. Shen, A. Portieri, and A. Husain, "Delayed release tablet dissolution related to coating thickness by terahertz pulsed image mapping," *J. Pharma. Sci.*, vol. 97, no. 4, pp. 1543-1550, 2008.

[102] W. Kohler, M. Panzner, U. Klotzbach, E. Beyer, S. Winnerl, M. Helm, F. Rutz, C. Jordens, M. Koch, and H. Leitner, "Non-destructive investigation of paintings with THz-radiation," *Proceedings of the European Conference of Non-Destructive Testing*, Berlin, Germany, 2006.

[103] J. B. Jackson, M. Mourou, J. F. Whitaker, I. N. Duling III, S. L. Williamson, M.

Menu, and G. A. Mourou, "Terahertz imaging for non-destructive evaluation of mural paintings," *Opt. Coram.*, vol. 281, no. 4, pp. 527-532, 2008.

[104] K. Fukunaga and Y. Ogawa, S. I. Hayashi, and I. Hosako, "Terahertz spectroscopy for art conservation," *IEICE Electron. Exp.*, vol. 4, no. 8, pp. 258-263, 2007.

[105] K. Fukunaga and Y. Ogawa, S. I. Hayashi, and I. Hosako, "Application of terahertz spectroscopy for character recognition in a medieval manuscript," *IEICE Electron. Exp.*, vol. 5, no. 7, pp. 223-228, 2008.

[106] A. J. L. Adam, P. C. M. Planken, S. Meloni, and J. Dik, "TeraHertz imaging of hidden paint layers on canvas," *Opt. Express*, vol. 17, no. 5, pp. 3407-3414, 2009.

[107] D. L. Donoho, "Compressed sensing," *IEEE Trans. Inf. Theory*, vol. 52, no. 4, pp. 1289-1306, 2006.

[108] E. J. Candès, J. Romberg, and T. Tao, "Robust uncertainty principles: Exact signal reconstruction from highly incomplete frequency information," *IEEE Trans. Inf. Theory*, vol. 52, no. 2, pp. 489 - 509, 2006.

[109]E. J. Candès and T. Tao, "Near optimal signal recovery from random projections: Universal encoding strategies?," *IEEE Trans. Inf. Theory*, vol. 52, no. 12, pp. 5406-5425, 2006.

[110] R. G. Baraniuk, "Compressive sensing," *IEEE Signal Proc. Mag*., vol. 24, no. 4, pp. 118-120, 2007.

[111] E. J. Candès, "Compressive sampling," *in Int. Congress of Mathematicians*, Madrid, Spain, vol. 3, pp. 1433-1452, 2006.

[112] E. J. Candès and M. B. Wakin, "An introduction to compressive sampling," IEEE Signal Proc. Mag., vol. 25, no. 2, pp. 21-30, 2008.

[113] J. Romberg, "Imaging via compressive sampling," *IEEE Signal Proc. Mag.*, vol. 25, no. 2, pp. 14-20, 2008.

[114] R. G. Baraniuk, "More Is less: Signal processing and the data deluge," *Science*, vol. 331, no. 6018, pp. 717-719, 2011.

[115] M. Fornasier and H. Rauhut, "Compressive sensing," *Chapter in Part 2 of the Handbook of Mathematical Methods in Imaging* (O. Scherzer Ed.), 2011.

[116] M. A. Davenport, M. F. Duarte, Y. C. Eldar, and G. Kutyniok, "Introduction to compressed sensing," *Chapter in Compressed Sensing: Theory and Applications, Cambridge University Press*, 2012.

[117] M. F. Duarte and Y. C. Eldar, "Structured compressed sensing: Theory and applications," *IEEE Trans. on Signal Proc.*, vol. 59, no. 9, pp. 4053-4085, 2011.

[118] R. M. Willett, R. F. Marcia, and J. M. Nichols, "Compressed sensing for practical optical imaging systems: a tutorial," *Opt. Eng.*, vol. 50, no. 7, pp. 072601, 2011.

[119] http://dsp.rice.edu/cs

[120] H. Nyquist, "Certain topics in telegraph transmission theory," *Trans. AIEE*, vol. 47, pp. 617-644, Apr. 1928 Reprint as classic paper in: *Proc. IEEE*, vol. 90, no. 2, 2002.

[121] C. E. Shannon, "Communication in the presence of noise," *Proc. Institute of*

Radio Engineers, vol. 37, no.1, pp. 10-21, 1949. Reprint as classic paper in: *Proc. IEEE*, vol. 86, no. 2, 1998.

[122] M. Unser, "Sampling-50 years after Shannon," *Proc. IEEE*, vol. 88, no. 4, pp. 569-587, 2000.

[123] Y. C. Eldar and T. Michaeli, "Beyond bandlimited sampling," *IEEE Signal Proc. Mag.*, vol. 26, no. 3, pp. 48-68, 2009.

[124] J. Ke and M. A. Neifeld, "Optical architectures for compressive imaging," *Applied Optics*, vol. 46, no. 22, 5293-5303, 2007.

[125] M. F. Duarte, M. A. Davenport, D. Takhar, J. N. Laska, T. Sun, K. F. Kelly, and R. G. Baraniuk, "Single-pixel imaging via compressive sampling," *IEEE Signal Proc. Mag.*, vol. 25, no. 2, pp.83-91, 2008.

[126] J. Haupt, W. U. Bajwa, M. Rabbat, and R. Nowak, "Compressed sensing for networked data," *IEEE Signal Proc. Mag.*, vol. 25, no. 2, pp. 92-101, 2008.

[127] K. Gedalyahu and Y. C. Eldar, " Time-delay estimation from low-rate samples: A union of subspaces approach," *IEEE Trans. Signal Proc.*, vol. 58, no. 6, pp. 3017-3031, 2010.

[128] M. Mishali and Y. C. Eldar. "Blind multi-band signal reconstruction: Compressed sensing for analog signals," *IEEE Trans. Signal Proc.*, vol. 57, no. 3, pp. 993-1009, 2009.

[129] K. Gedalyahu, R. Tur, and Y. C. Eldar, "Multichannel sampling of pulse streams at the rate of innovation," *IEEE Trans. Signal Proc.*, vol. 59, no. 4, pp. 1491-1504, 2011.

[130] R. G. Baraniuk, V. Cevher and M. B. Wakin, "Low-dimensional models for dimensionality reduction and signal recovery: A geometric perspective," *Proc. IEEE*, vol. 98, no. 6, pp. 959-971, 2010.

[131] R. A. DeVore, "Nonlinear approximation," *Acta Numerica*, vol. 7, pp.51-150, 1998.

[132] A. M. Bruckstein, D. L. Donoho, and M. Elad, "From sparse solutions of systems of equations to sparse modeling of signals and images," *SIAM Rev.*, vol. 51, no. 1, pp. 34-81, 2009.

[133] W. B. Pennebaker, J. L. Mitchell, "JPEG still image data compression standard," *Van Nostrand Reinhold*, 1993. *Eighth printing by Kulwer Academic Publishers*, U. S. A., 2004.

[134] D. Taubman, M. Marcellin, "JPEG2000: Image compression fundamentals, standards and practice," *Kluwer Academic Publishers*, U. S. A., 2001.

[135] D. L. Donoho, "De-noising by soft-thresholding," *IEEE Trans. Inf. Theory*, vol. 41, no. 3, pp. 613-627, 1995.

[136] I. F. Gorodnitsky and B. D. Rao, "Sparse signal reconstruction from limited data using FOCUSS: A re-weighted minimum norm algorithm," *IEEE Trans. Signal Proc.*, vol. 45, no. 3, pp. 600-616, 1997.

[137] S. S. Chen, D. L. Donoho, and M. A. Saunders, "Atomic decomposition by basis pursuit," *SIAM J. Sci. Computing*, vol. 20, no. 1, pp. 33-61, 1998.

[138] R. Rubinstein, A. M. Bruckstein, and M. Elad, "Dictionaries for sparse representation modeling," *IEEE proceeding*, vol. 98, no. 6, pp. 1045-1057,

2010.

[139] E. J. Candès and D. L. Donoho, "Curvelets - surprisingly effective nonadaptive representation for objects with edges," *Curves and Surfaces*, 1999.

[140] E. J. Candès, L. Demanet, D. L. Donoho, and L. Ying, "Fast descrete curvelet transforms," *Multiscale Modeling & Simulation*, vol. 5, no. 3, pp. 861-899, 2006.

[141] M. N. Do and M. Vetterli, "Contourlets: A directional multiresolution image representation," *Int. conf. image process.*, vol. 1, pp. 357-360, 2002.

[142] M. N. Do and M. Vetterli, "The contourlet transform: an efficient directional multiresolution image representation, " *IEEE Trans. image process.*, vol. 14, no. 12, pp. 2091-2106, 2005.

[143] E. LePennec and S. Mallat, "Sparse geometric image representations with bandelets," *IEEE Trans. Image Process*., vol. 14, no. 4, pp. 423-438, 2005.

[144] G. Peyre and S. Mallat, "Surface compression with geometric bandelets," ACM Trans. Graph., vol. 24, no. 3, pp. 601-608, 2005.

[145] E. J. Candès, J. Romberg, and T. Tao, "Stable signal recovery from incomplete and inaccurate measurements," *Comm. Pure Appl. Math.*, vol. 59, no. 8, pp. 1207-1223, 2006.

[146] E. J Candès and T. Tao, "Decoding by linear programming," *IEEE Trans. Inf. Theory*, vol. 51, no. 12, pp. 4203-4215, 2005.

[147] M. A. Davenport, J. N. Laska, P. T. Boufouons, and R. G. Baraniuk, "A simple proof that random matrices are democratic," Technical Report TREE 0906, Rice Univ., ECE Dept., 2009.

[148] J. N. Laska, P. T. Boufounos, M. A. Davenport, and R. G. Baraniuk, "Democracy in action: Quantization, saturation, and compressive sensing," *Appl. Comput. Harmon. Anal.*, vol. 31, no. 3, pp. 429-443, 2011.

[149] J. A. Tropp, J. N. Laska, M. F. Duarte, J. K. Romberg, and R. G. Baraniuk, "Beyond Nyquist: Efficient sampling of sparse, bandlimited signals," *IEEE Trans. Inf. Theory*, vol. 56, no. 1, pp. 520-544, 2010.

[150] J. A. Tropp, M. B. Wakin, M. F. Duarte, D. Baron, and R. G. Baraniuk, "Random filters for compressive sampling and reconstruction," *In 31st IEEE International Conference on Acoustics, Speech, and Signal Processing (ICASSP)*, Toulouse, France, 2006.

[151] M. Mishali and Y. C. Eldar, "From theory to practice: Sub-Nyquist sampling of sparse wideband analog signals," *IEEE J. Select. Top. Signal Processing*, vol. 4, no. 2, pp. 375-391, 2010.

[152]J. Romberg, "Compressive sensing by random convolution," *SIAM J. Imag. Sci.*, vol. 2, no. 4, pp. 1098-1128, 2009.

[153] J. P. Slavinsky, J. N. Laska, M. A. Davenport, and R. G. Baraniuk, "The compressive mutliplexer for multi-channel compressive sensing," *In 36th IEEE International Conference on Acoustics, Speech, and Signal Processing (ICASSP)*, Prague, Czech Republic, 2011.

[154] W. U, Bajwa, J. D. Haupt, G. M. Raz, S. J. Wright, and R. D. Nowak, "Toeplitz-structured compressed sensing matrices," *In Proc. IEEE Workshop on*

Statistical Signal Processing, pp. 294-298, Washington D. C., USA, 2007.

[155] J. D. Haupt, W. U. Bajwa, G. M. Raz, and R. D. Nowak, "Toeplitz compressed sensing matrices with applications to sparse channel estimation," *IEEE Trans. Inf. Theory*, vol. 56, no. 11, pp. 5862-5875, 2010.

[156] F. Sebert, Y. M. Zou, L. Ying, "Toeplitz block matrices in compressed sensing and their applications in imaging," *in 5th International Conference on Information Technology and Application and Biomedicine,* pp. 47-50, Shenzhen, P. R. C., 2008.

[157] H. Rauhut, "Compressive sensing and structured random matrices," *Theoretical Foundations and Numerical Methods for Sparse Recovery*, vol. 9 of Radon Series Comp. Appl. Math., pp. 1-92. M. Fornasier, ed., deGruyter, 2010.

[158] W. Yin, S. P. Morgan, J. Yang, and Y. Zhang, "Practical compressive sensing with Toeplitz and circulant matrices," Rice University CAAM Technical Report TR10-01, 2010.

[159] M. Herman and T. Strohmer, "High-resolution radar via compressed sensing," *IEEE Trans. Signal Processing,* vol. 57, no. 6, pp. 2275-2284, 2009.

[160] D. L. Donoho, "For most large underdetermined systems of linear equations, the minimal l_1 norm solution is also the sparsest solution," *Comm. Pure Appl. Math.*, vol. 59, no. 6, pp. 797-829, 2006.

[161] D. L. Donoho, "For most large underdetermined systems of linear equations, the minimal l_1 norm near-solution approximates the sparsest near-solution," *Comm. Pure Appl. Math.*, vol. 59, no. 7, pp. 907-934, 2006.

[162]Y. Tsaig, D. L. Donoho, "Extensions of compressed sensing," *Signal Processing*, vol. 86, no. 3,pp. 549-571, 2006.

[163] H. Fang, Q. B. Zhang and S. Wei, "A method of image reconstruction based on sub-gaussian random projection," *J. Computer Research and Development*, vol. 45, no. 8, pp. 1402-1407, 2008.

[164] T. T. Do, T. D. Trany and L. Gan, "Fast compressive sampling with structurally random matrices," *in 33rd IEEE International Conference on Acoustics, Speech and Signal Processing*, pp. 3369-3372, Las Vegas, NV, 2008.

[165] J. Ke and M. A. Neifeld, "Optical architectures for compressive imaging," *Applied Optics*, vol. 46, no. 22, pp. 5293-5303, 2007.

[166] L. Gan, "Block compressed sensing of natural images," *in 15th International Conference on Digital Signal Processing*, IEEE, pp. 403–406, Cardiff, UK, 2007.

[167] B. Logan, "Properties of high-pass signals," PhD thesis, Columbia University, 1965.

[168] D. L. Donoho, M. Elad and V. Temlyakov, "Stable recovery of sparse overcomplete representations in the presence of noise," *IEEE Trans. Inf. Theory*, vol. 52, no. 1, pp. 6-18, 2006.

[169] K. Koh, S. J. Kim and S. Boyd, "An interior-point method for large-scale l_1 regularized least squares," *Journal of machine learning research*, vol. 8, pp. 1519-1555, 2007.

[170] M. A. T. Fiqueiredo, R. D. Nowak and S. J. Wright, "Gradient projection for

sparse reconstruction: Application to compressed sensing and other inverse problems," *IEEE Journal of Selected Topics in Signal Processing*, vol. 1, no. 4, pp. 586-598, 2007.

[171] D. L. Donoho and Y. Tsaig, "Fast solution of l_1-norm minimization problems when the solution may be sparse," *Technical Report, Department of Statistics , Stanford University*, USA, 2008.

[172] E. J. Candès, N. Braun and M. B. Wakin, "Sparse signal and image recovery from compressive samples," *In 4th IEEE International Symposium on Biomedical Imaging: From Nano to Macro*, vol. 1-3, pp. 976-979, Arlington, VA, 2007.

[173] D. Needell and J. A. Tropp, "CoSaMP: Iterative signal recovery from incomplete and inaccurate samples," *Appl. Comput. Harmon. Anal.*, vol. 26, no. 3, pp. 301-321, 2009.

[174] T. Blumensath and M. E. Davies, "Iterative hard thresholding for compressive sensing," *Appl. Comput. Harmon. Anal.*, vol. 27, no. 3, pp. 265-274, 2009.

[175] W. Dai and O. Milenkovic, "Subspace pursuit for compressive sensing signal reconstruction," *IEEE Trans. Inform. Theory*, vol. 55, no. 5, pp. 2230-2249, 2009.

[176] I. Daubechies, M. Defrise, and C. D. Mol, "An iterative thresholding algorithm for linear inverse problems with a sparsity constraint," *Comm. Pure Appl. Math.*, vol. 57, no. 11, pp. 1413-1457, 2004.

[177] M. A. Davenport and M. B. Wakin, "Analysis of orthogonal matching pursuit using the restricted isometry property," *IEEE Trans. Inform. Theory*, vol. 56, no. 9, pp. 4395-4401, 2010.

[178] D. L. Donoho, Y. Tsaig, I. Drori, and J. L. Stark, "Sparse solution of underdetermined linear equations by stagewise orthogonal matching pursuit," submitted for publication, 2007.

[179] S. G. Mallat and Z. F. Zhang. "Matching pursuits with time-frequency dictionaries," *IEEE Trans. Signal Processing*, vol. 41, no. 12, pp. 3397-3415, 1993.

[180] D. Needell and R. Vershynin, "Uniform uncertainty principle and signal recovery via regularized orthogonal matching pursuit," *Found. Comput. Math.*, vol. 9, no. 3, pp. 317-334, 2009.

[181] D. Needell and R. Vershynin, "Signal recovery from incomplete and inaccurate measurements via regularized orthogonal matching pursuit," *IEEE J. Select. Top. Signal Processing*, vol. 4, no. 2, pp. 310-316, 2010.

[182] D. Needell and R. Vershynin, "Greedy signal recovery and uncertainty principles," *Conference on Computational Imaging.*, Proceedings of the SPIE, vol. 6814, no. 68140J-12, San Jose, CA, 2008.

[183] N. G. Kingsbury, "Complex wavelets for shift invariant analysis and filtering of signals," *Appl. Comput. Harmon. Anal.*, vol. 10, no. 3, pp. 234-253, 2001.

[184] T. Blumensath and M. E. Davies, "Iterative thresholding for sparse approximations," *Journal of Fourier Analysis and Applications*, vol. 14, no. 5-6, pp. 629-654, 2007.

[185] L. I. Rudin, S. Osher, and E. Fatemi, "Nonlinear total variation based noise removal algorithms," *Physica D*, vol. 60, no. 1-4, pp. 259-268, 1992.

[186] M. S. Lobo, L. Vandenberghe, S. Boyd and H. Lebret, "Applications of second-order cone programming," *Linear Algebra and its Applications,* vol. 284, no. 1-3, pp. 193-228, 1998.

[187] D. Takhar, J. Laska, M. Wakin, M. Duarte, D. Baron, S. Sarvotham, K. Kelly, and R. Baraniuk, "A new compressive imaging camera architecture using optical-domain compression," *Proc. SPIE*, vol. 6065, pp. 6509, 2006.

[188] D. J. Brady, K. Choi, D. L. Marks, R. Horisaki, and S. Lim, "Compressive holography," *Opt. Express*, vol. 17, no. 15, pp. 13040-13049, 2009.

[189] M. E. Gehm, R. John, D. J. Brady, R. M. Willett, and T. J. Schulz, "Single-shot compressive spectral imaging with a dual-disperser architecture," *Opt. Express*, vol. 15, no. 21, pp. 14013-14027, 2007.

[190] F. J. Herrmann, Y. A. Erlangga, and T. T. Y. Lin, "Compressive simultaneous full-waveform simulation," *Geophys.*, vol. 74, no. 4, pp. A35-A40, 2009.

[191] B. Jafarpour, V. K. Goyal, D. B. McLaughlin, and W. T. Freeman, "Transform-domain sparsity regularization of inverse problems in geosciences," *Geophys.*, vol. 74, no. 5, pp. R69-R83, 2009.

[192] M. Lustig, D. Donoho, and J. M. Pauly, "Sparse MRI: The application of compressed sensing for rapid MR imaging," *Magnetic Resonance in Medicine*, vol. 58, no. 6, pp. 1182-1195, 2007.

[193] J. Provost and F. Lesage, "The application of compressed sensing for photo-acoustic tomography," *IEEE Trans. Med. Imaging,* vol. 28, no. 4, pp. 585-594, 2009.

Chapter 3

Random Projection on THz Imaging

3.1 Introduction of Random Projection on THz Imaging

Over the past decade, TPI has been demonstrated in applications areas as diverse as the medical diagnosis of human tissue, the detection and chemical mapping of illicit drugs and explosives, and pharmaceutical tablet inspection [1-4]. Because of the relatively modest power levels available from the photoconductive sources commonly used in THz time-domain spectroscopy and imaging systems, and the lack of compact and sensitive multi-element THz detectors, most TPI experiments have been performed by raster scanning the object relative to a focused THz beam, and by using a single-point detector. Consequently, a complete image usually takes minutes or even hours to acquire, depending on the total number of pixels and the required spectral range/resolution. For example, normally it takes six minutes to scan a 400×400 pixels image [5].

Focal-plane detector arrays can be used to achieve real-time THz imaging [6, 7]. However, this system requires high complexity and operational cost. More importantly, such systems cannot provide spectroscopic information of sample. By non-uniform sampling in the Fourier domain, interferometric or tomographic approaches can significantly reduce the number of measurements. However, the acquisition speed of such systems is still limited by raster scanning unless a full THz detector array is used [8-10]. The acquisition speed is a major limiting factor for real-time applications such as in vivo medical and security imaging, or for on-line industrial process monitoring. This chapter discusses how we used CS, a novel theory in signal processing, to achieve high-speed THz imaging.

Nowadays, CS has emerged to sense sparse signals by reducing the sampling rate and storage of acquisition devices [11, 12]. As discussed in section 2.2.3, a typical THz image or waveform can be approximated as a sparse signal. In addition, the optical single-pixel camera architecture can be adapted to image at wavelengths (such as THz range and far-infrared range) that are currently impossible with conventional CCD and CMOS. Thus, a single-pixel THz imaging system can be built based on the concept of CS. Figure. 3.1 shows the schematic diagram of this single-pixel THz imaging system. After propagating through the sample and masks, the THz beam was collimated, by using a focus lens, onto the detector. A small number of linear projections of an image onto random binary patterns were recorded and finally used for reconstruction and processing. Compared with conventional THz imaging, this approach not only eliminates the need to raster scan the object or THz beam, but also reduces the number of measurements required. In the next sections, we will demonstrate that such a fast and efficient THz imaging system is achievable by using random projection approach.

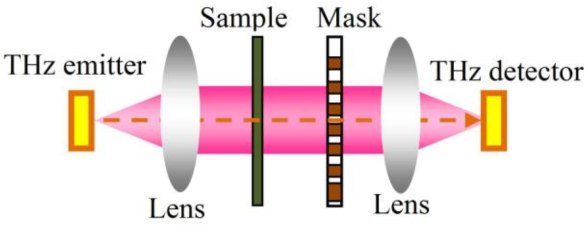

Figure. 3.1 Schematic diagram of single-pixel THz imaging system.

3.2 Simulation Procedure on Random Projection

As discussed in equation 2.16, given a THz signal $x \in R^N$, we can represent the CS process using M linear measurements mathematically as $y_{M\times 1} = \Phi_{M\times N} x_{N\times 1}$ where Φ is an $M \times N$ sensing matrix and $y \in R^M$. Sensing matrix Φ aims to reduce the dimension from R^N to R^M ($M \ll N$). In practice, the linear measurements $y_{M\times1}$, i.e., linear projections of an image onto random binary patterns, can be directly measured from the THz detector. In the simulations, they can be obtained by multiplying the original image $x_{N\times1}$ and sensing matrix Φ. In order to solve the problem shown in equation 2.19, the minimum mean square error (MMSE) linear estimation is used as the reconstruction algorithm [13, 14]. Then, the reconstructed image can be written as $\hat{x}_{N\times1} = \hat{\Phi}_{N\times M}\, y_{M\times1}$. According to this, using the equation 2.20, the reconstruction matrix can be expressed as $\hat{\Phi} = R_{xx}\Phi^T(\Phi R_{xx}\Phi^T)^{-1}$, where R_{xx} represents the autocorrelation function of the input signal. For nature images, we approximate R_{xx} using the AR(1) model with correlation coefficient $\rho = 0.95$. A flowchart diagram of the simulation on synthetic and real-world THz data is presented in Figure. 3.2, to demonstrate a general reconstruction process.

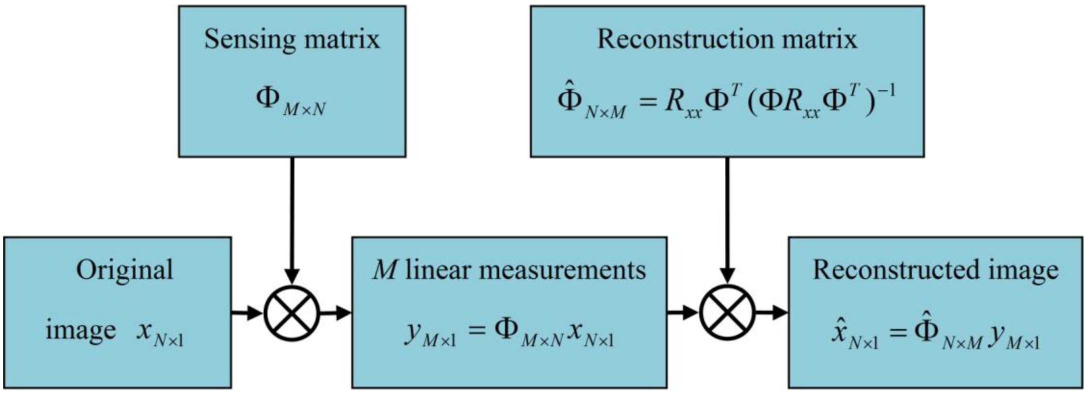

Figure. 3.2 Flowchart diagram of simulation on synthetic and real-world THz data.

3.3 Simulation Results on Synthetic Data and Real-World THz Data

A. Data Analysis using a Different Number of Measurements

This section reports the random projection on THz imaging in order to briefly demonstrate some motivations and benefits of the CS-THz system. From Figure. 3.3, we assumed that we aim to obtain a 96×96 pixels THz image from a full body scan, and, obviously, a weapon is hidden on the back of the human body. The conventional TPI will take 96×96=9216 measurements to fully raster scan the object, thus it is time-consuming. Full random matrices are chosen to be the sensing matrices to reconstruct the images. The entries in such matrices are independent and identically distributed (i.i.d.). More significantly, it can also be shown that random matrices will satisfy the RIP with high probability if the entries are chosen according to a Gaussian, Bernoulli, or more generally any sub-Gaussian distribution. The full random matrices have been mathematically proved for compressed sensing, so we chose them as our sampling operator in this chapter to validate the feasibility of random projection on THz imaging. MMSE linear estimation is used as the reconstruction algorithm. Figure. 3.4 shows the simulated results $y_{M\times 1} = \Phi_{M\times N} x_{N\times 1}$ for linear measurements. The 96×96 original image $x_{N\times 1}$ is presented in the left-hand inset. The reconstructed image $\hat{x}_{N\times 1} = \hat{\Phi}_{N\times M}\, y_{M\times 1}$ (right-hand inset) is obtained by using 500 measurements. In this case, M=500, N=9216, and, obviously, the reconstructed image can be identified when M<<N.

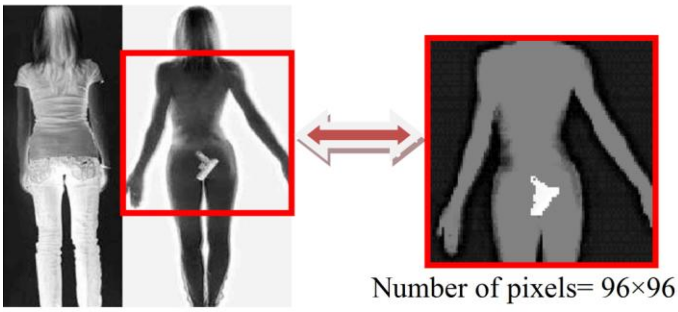

Figure. 3.3 Original image for body scan with weapon.

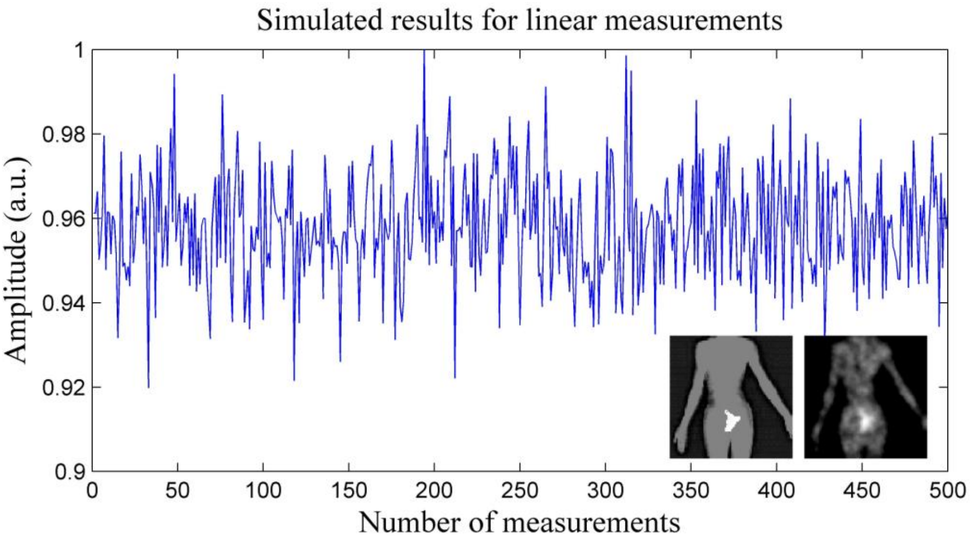

Figure. 3.4 Simulated results for linear measurements. The left-hand inset image is the original image and the right-hand inset image is the reconstructed image using 500 linear measurements.

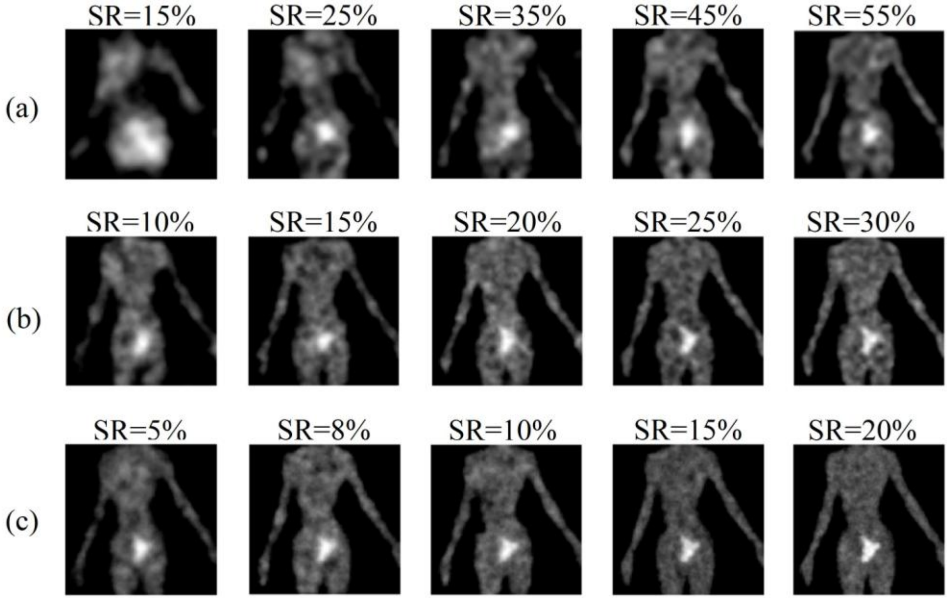

Figure. 3.5 Reconstructed images using (a) 24×24 physical pixels sensing matrices; (b) 48×48 physical pixels sensing matrices; and (c) 96×96 physical pixels sensing matrices. (SR: sampling rate).

The image is respectively reconstructed using three various sizes of sensing matrices, which contain 24×24, 48×48 and 96×96 physical pixels. Note that all three sets of sensing matrices are converted to 96×96 pixels for sampling. Figure. 3.5 shows the reconstructed images using these three various sizes of sensing matrices. For all kinds of sensing matrices, the more measurements we measured (i.e., larger sampling rate) the better the quality of the reconstructed images. Normally, good reconstruction results (i.e., in this case, the weapon can be identified easily) can be obtained by random sampling only 10%-30% of the sample, rather than pixel-by-pixel raster scanning the object. For high resolution sensing matrices such as in Figure. 3.5 (c), the required measurements can be further reduced to only 5%-8%. Furthermore, as Figure. 3.5 (a) to (c) shows, various sizes of sensing matrices can provide various resolutions of reconstructed images. That means, for certain applications such as security inspection, CS-THz imaging system can maintain the balance of individual privacy and security requirements. Using low resolution sensing matrices (Figure. 3.5 (a)), we can protect privacy and identify whether the object in which we are interested actually exists. If yes, this imaging procedure can be done using higher resolution sensing matrices (Figure. 3.5 (b) and (c)) to recognize the certain shape of the desired object. In brief, compared with conventional TPI, the CS-THz system has potential benefits to further speed up the imaging procedure.

B. Data Analysis using Different Signal to Additive Gaussian Noise Ratios

In order to illustrate the robustness of such a CS-THz system, we compared the variety of reconstructed images (sample image "angry" and "smile") from the simulated signals in the presence of Gaussian white noises, as shown in Figure. 3.6. In addition, the MMSE linear estimation was used for recovery, and all images have 96×96 pixels. Considering the complexity of the sample images, sampling rates of 10%, 20% and 30% were chosen. It can be seen that most of the reconstructed images can be easily recognized, except for ones at relatively low signal to additive Gaussian noise ratio and low sampling rate. Obviously, the quality of reconstructed images is determined by the sampling rates and the additive signal-noise-ratio. Higher SNRs and more sampling rates offer a more impressive reconstructed image.

Based on the data from Figure. 3.6, we can further quantize the signal to noise ratios (SNR) for reconstructed images, as shown in Figure. 3.7. As expected, the SNRs for reconstructed images become greater when increasing the number of measurements or the signal to additive Gaussian white noise ratio; also, they will tend to stabilize when in the presence of high signal to additive Gaussian noise ratio. The reconstructed results could perform much better when using other nonlinear algorithms, however, the imaging procedure will synchronously require more computations.

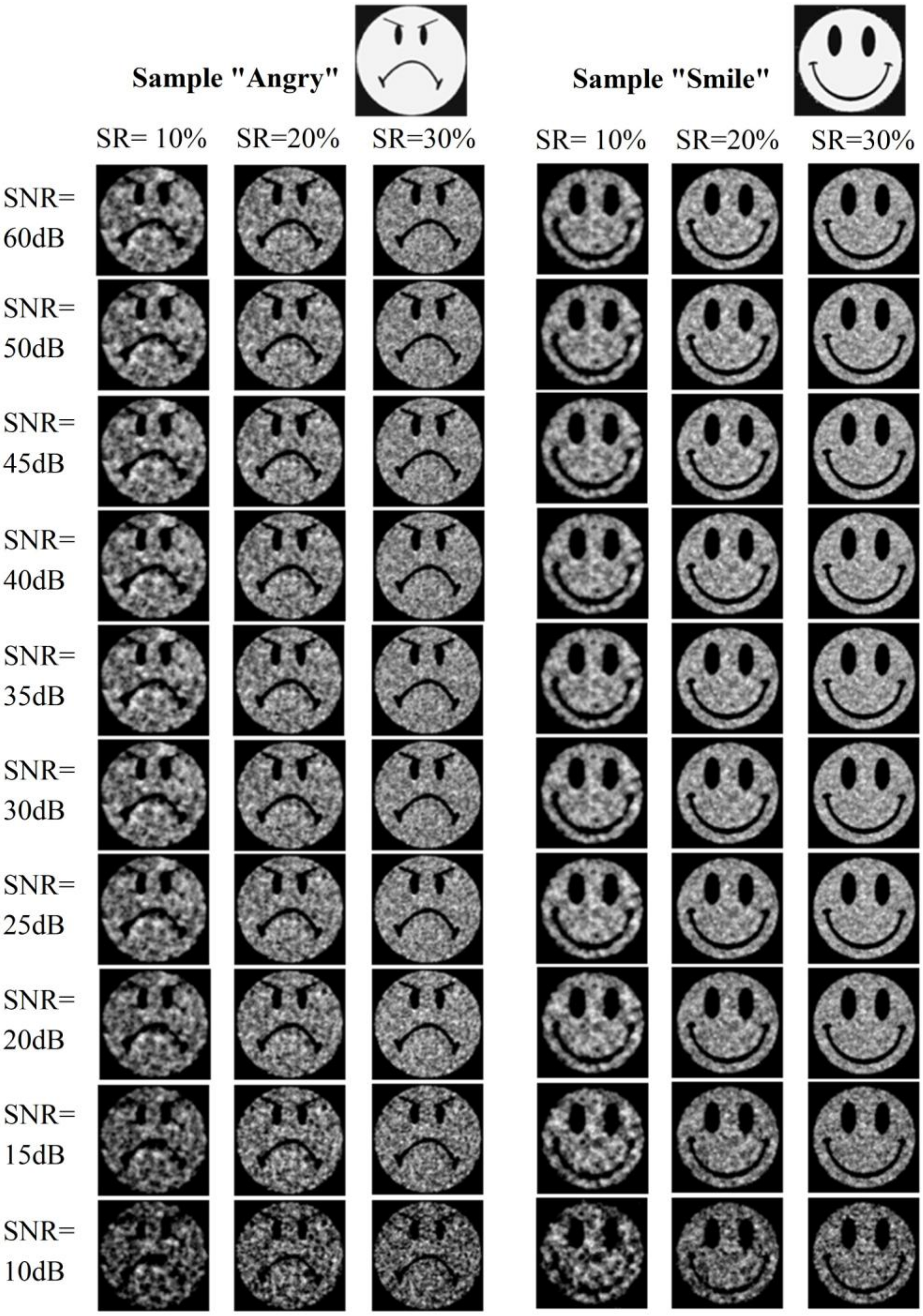

Figure. 3.6 The simulation results for reconstructing two images ("angry" and "smile") using the full random projection. MMSE linear estimation is used for recovery. All images have 96×96 pixels. (SR: sampling rate, SNR: signal to additive Gaussian noise ratio).

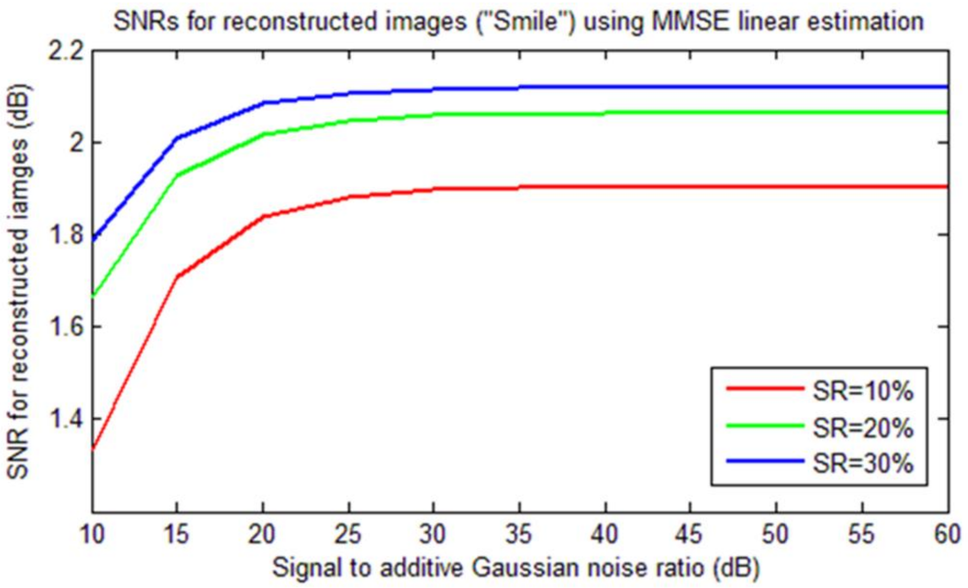

Figure. 3.7 SNRs for reconstructing an image "Smile" using the full random projection. MMSE linear estimation is used for recovery. (SR: sampling rate, SNR: signal to noise ratio).

C. Data analysis on spatial resolution

Aiming to quantize the spatial resolution of such an imaging system, a given sample (a single-pixel line) was reconstructed using MMSE linear estimation for different sampling rates, as shown in Figure. 3.8. Figure. 3.9 (a) shows the A-scan of reconstructed image from each row of the data for reconstructing a single-pixel line at 50% sampling rate, which is presented in Figure. 3.8 (j). In Figure. 3.9 (b), we averaged all the 96 curves presented in Figure. 3.9 (a) for spatial resolution definition. The spatial resolution can be calculated using full width at half maximum (FWHM) method, given by the difference between the two extreme values of the independent variable at which the dependent variable is equal to half of its maximum value $f_{\max}$.

The total pixel number of the image and the corresponding sampling rates determine the spatial resolution of the reconstructed image. The corresponding spatial resolutions for different sampling rates are shown in Table. 3.1. Considering the reconstructed images are normally obtained by using no more than 30% sampling rates of total pixels, the spatial resolution of such random projection THz imaging system is approximately two pixels.

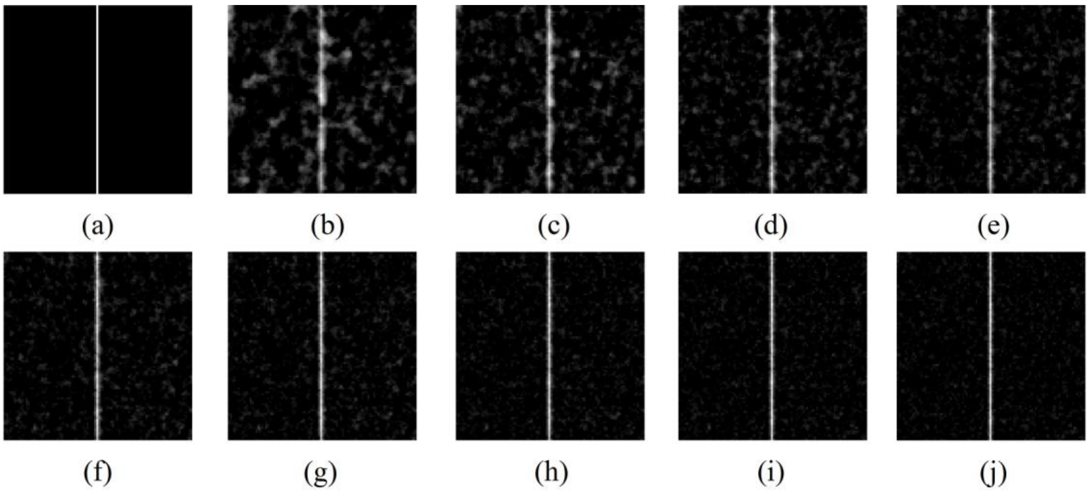

Figure. 3.8 (a) Original image (a single-pixel line). The corresponding reconstructed results (b)-(j) using MMSE linear estimation for different sampling rates at 10%, 15%, 20%, 25%, 30%, 35%, 40%, 45% and 50%, respectively. All images have 96×96 pixels.

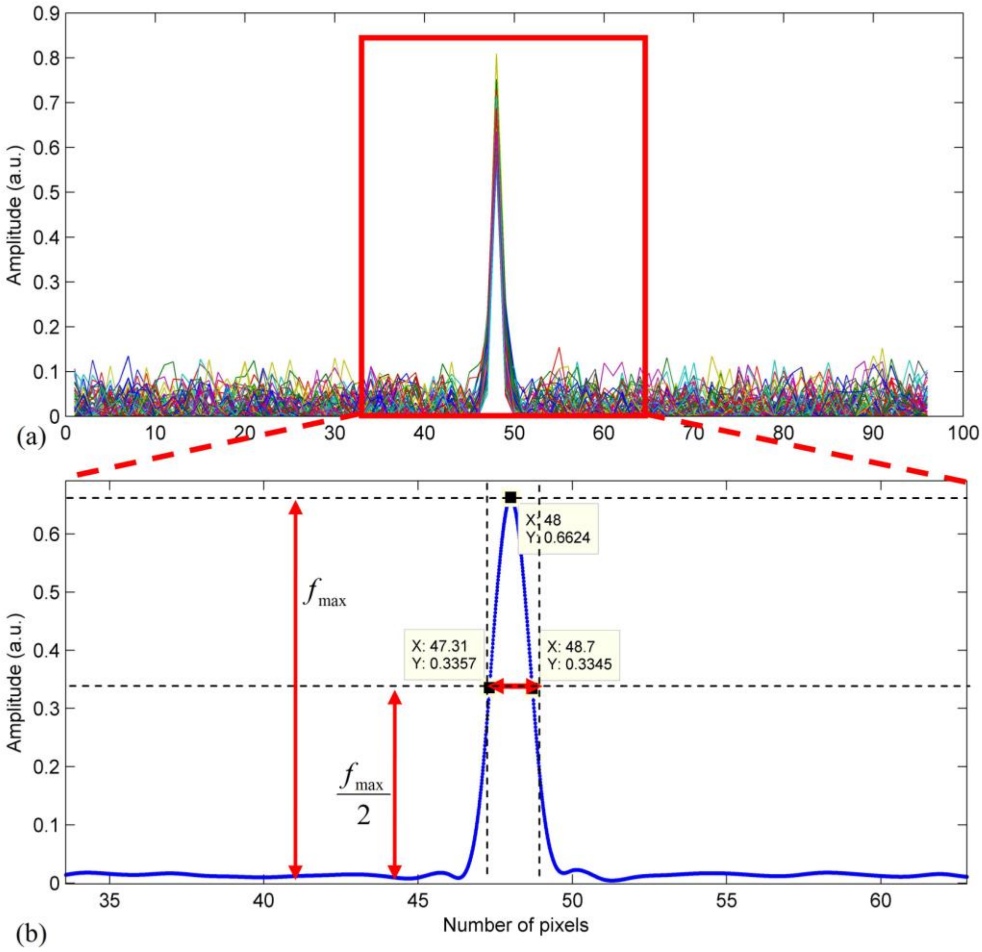

Figure. 3.9 (a) A-scan of reconstructed image from each row of the data for reconstructing single-pixel line at 50% sampling rate. All 96 rows of the data from Figure. 3.7 (j) are presented. (b) The average value of all rows of the data from (a).

Table. 3.1 The corresponding spatial resolution for different sampling rates.

	10%	15%	20%	25%	30%	35%	40%	45%	50%
Spatial resolution (pixels)	2.74	2.25	2.05	1.83	1.70	1.59	1.52	1.47	1.39

3.4 Simulation Results on Real-World THz Data

To further demonstrate random projection on THz imaging, we extended this idea using real-world THz data. The THz data were acquired across an area of 20.0 mm×22.0 mm using a TPIscan-1000 system (TeraView Ltd, Cambridge, U.K.), which covers a spectral range from 0.1 to 3.5 THz. The images have 268×120 pixels and at each pixel a THz waveform was recorded as function of time delay over a scan range of 4.0 mm. The sample used is a polythene pellet of a diameter of 25.0 mm. Inside the pellet there is a T-shaped plastic sheet which is located approximately 0.2 mm below the sample surface. We chose a two-dimensional datacube at a certain time delay (152th temporal band); and for ease of computations we resized the images, using bicubic interpolation, so that the overall data size was 96×96.

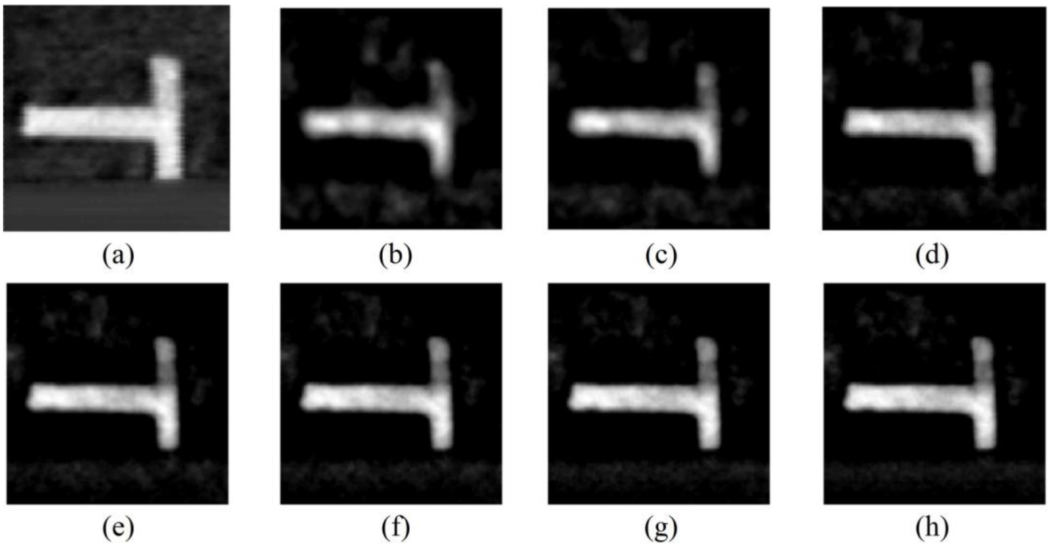

Figure. 3.10 (a) Original image. The corresponding reconstruction results (b)-(h) using MMSE linear estimation for different sampling rates at 3%, 5%, 10%, 15%, 20%, 25% and 30%, respectively.

Table. 3.2 Mean square error (MSE) and signal-to-noise ratio (SNR) in dB, for different observation rates.

	3%	5%	10%	15%	20%	25%	30%
MSE	0.6128	0.5738	0.5482	0.5401	0.5366	0.5348	0.5333
SNR (dB)	4.2533	4.8242	5.2204	5.3513	5.4064	5.4364	5.4604

Figure. 3.10 (b)-(h) shows the reconstruction results for different sampling rates at 3%, 5%, 10%, 15%, 20%, 25% and 30%, respectively. The dark areas correspond to the polythene pellet, and the bright areas correspond to the T-shaped plastic sheet. One can see that all the reconstruction results are visually recognizable. As the sample is relatively sparse, it can be reconstructed at very low sampling rates, such as 3% of the total pixels. According to the data from Figure. 3.10, Table. 3.2 show the mean square error (MSE) and signal-to-noise ratio (SNR) in dB for different observation rates. As expected, better quality images (better SNR) could be obtained by increasing the observation rate.

3.5 Summary

The simulation results on synthetic and real-world THz data demonstrate the feasibility of random projection THz imaging system and its impressive performances. This chapter has discussed the effect of SNRs and the number of measurements, and the limit of spatial resolution. After quantizing these performances, we found that it is not only worthwhile but imperative to develop the physical CS-THz imaging system to solve the problems such as a lack of conventional CCD and CMOS imagers in THz range and slow data acquisition using the raster scanning approach.

References:

[1] B. B. Hu and M. C. Nuss, "Imaging with terahertz waves," *Opt. Lett*. vol. 20, no. 16, pp. 1716-1718, 1995.

[2] E. Pickwell, B. E. Cole, A. J. Fitzgerald, M. Pepper and V. P. Wallace, "In vivo study of human skin using pulsed terahertz radiation," *Phys. Med. Biol*. vol. 49, no. 9, pp. 1595-1607 , 2004.

[3] K. Kawase, Y. Ogawa, Y. Watanabe, and H. Inoue, "Non-destructive terahertz imaging of illicit drugs using spectral fingerprints," *Opt. Express*, vol. 11, no. 20, pp. 2549-2554, 2003.

[4] Y. C. Shen and P. F. Taday, "Development and application of terahertz pulsed imaging for non-destructive inspection of pharmaceutical tablet," *IEEE J. Sel. Top. Quantum Electron*. vol. 14, no. 2, pp. 407-415, 2008.

[5] D. Zimdars, "High speed terahertz reflection imaging," *Proc. SPIE,* vol. 5692, pp. 255-259, 2005.

[6] A. W. M. Lee, Q. Qin, S. Kumar, B. S. Williams, Q. Hu, and J. L. Reno, "Real-time terahertz imaging over a standoff distance (>25 meters)," *Appl. Phys. Lett.*, vol. 89, no. 14, 141125, 2006.

[7] Z. P. Jiang and X. C. Zhang, "Terahertz imaging via electrooptic effect," *IEEE Trans. Microwave Theory Tech*. vol. 47, no. 12, pp. 2644-2650, 1999.

[8] A. Bandyopadhyay, A. Stepanov, A. Sengupta, D. E. Gary, M. D. Federici, B. Schulkin, R. B. Barat, E. Michalopoulou, D. Zimdars, and J. F. Federici, "Terahertz interferometric and synthetic aperture imaging," *J. Opt. Soc. Am. A.*, vol. 23, no. 5, pp. 1168-1178, 2006.

[9] J. Pearce, H. Choi, D. M. Mittleman, J. White, and D. Zimdars, "Terahertz wide aperture reflection tomography," *Opt. Lett*. vol. 30, no. 13, pp. 1653-1655, 2005.

[10] S. Wang and X. C. Zhang, " Pulsed terahertz tomography," *J. Phys. D.*, vol. 37, no. 4, pp. R1-R36, 2004.

[11] D. L. Donoho, "Compressed sensing," *IEEE Trans. Inf. Theory,* vol. 52, no. 4, pp. 1289-1306, 2006.

[12] E. J. Candès, J. Romberg, and T. Tao, "Robust uncertainty principles: Exact signal reconstruction from highly incomplete frequency information," *IEEE Trans. Inf. Theory*, vol. 52, no. 2, pp. 489-509, 2006.

[13] L. Gan, "Block compressed sensing of natural images," *in 15th International Conference on Digital Signal Processing*, IEEE, pp. 403–406, 2007.

[14] J. Ke and M. A. Neifeld, "Optical architectures for compressive imaging," *Applied Optics*, vol. 46, no. 22, pp. 5293-5303, 2007.

[15] W. L. Chan, K. Charan, D. Takhar, K. F. Kelly, R. G. Baraniuk, and D. M. Mittleman, "A single-pixel terahertz imaging system based on compressed sensing," *Appl. Phys. Lett.*, vol. 93, no. 12, 121105, 2008.

[16] W. L. Chan, M. L. Moravec, R. G. Baraniuk, and D. M. Mittleman, "Terahertz imaging with compressed sensing and phase retrieval," *Opt. Lett*. vol. 33, no. 9, pp. 974-976, 2008.

[17] W. L. Chan, H. T. Chen, A. J. Tayler, I. Brener, M. J. Cich, and D. M. Mittleman, "A spatial light modulator for terahertz beams," *Appl. Phys. Lett.*, vol. 94, no. 21, 213511, 2009.

Chapter 4

CS-THz System using a set of Independent Optimized Masks

Recently Chan *et al.* [1, 2] reported the first THz imaging system based on the concept of CS [3, 4]. The basic hardware implementation is similar to Figure. 3.1. The free-space pulsed THz wave front traveling from an object to a single-point detector was spatially modulated by the insertion of a series of planar two-dimensional (2D) masks. Each mask comprised a random checkerboard pattern of 32×32 pixels that could each either transmit or block the THz radiation. By recording the THz field in the presence of each mask, a 2D image of the object was reconstructed [3]. This approach not only eliminates the need to raster scan the object or THz beam, but also reduces the number of measurements required [3]. This is a significant improvement in speed compared with the traditional raster scanning used for THz imaging.

A major advantage of TPI is that the transient electric field, rather than the radiation intensity, is measured as a function of time. This coherent detection scheme not only yields a THz signals with excellent SNR and high dynamic range, but also preserves the important phase information. Therefore, here comes the first problem: such CS-THz system has not been proved to obtain the spectral information of desired sample. The second problem is that a fully random binary operator incurs high computational complexity and huge memory, especially for high-resolution imaging [2]. For example, to get a 512×512 image with 64k measurements (i.e., 25% sampling rate), it requires nearly gigabytes storage and giga-flop operations, which is unrealistic in practice.

Here we proposed to use a set of optimized masks to further speed up the image acquisition process. We will also demonstrate that THz spectroscopic images could be obtained [5]. In this chapter, we discussed the design of the mask set. Numerical simulation results were presented to prove this idea. Then, the experimental results using both IR and THz source concluded that both the spatial and the spectral characteristics of samples could be reconstructed.

4.1 Masks Design based on CS

Consider an $I_r \times I_c$ image, with $N = I_r I_c$ pixels in total, and suppose that one wants to sample it using only $M(<< N)$ measurements. Let $x \in R^N$ denote the vector signal of the *N*-pixel input image. As discussed in the chapter 2, our CS process using *M* linear measurements can be defined as equation (2.14):

$$y_{M\times 1} = \Phi_{M\times N} x_{N\times 1},$$

where Φ is an $M \times N$ sensing matrix and $y \in R^M$. The selection of the sensing matrices Φ (so-called "masks" physically) holds the key to the quality of the reconstructed image. Typically, a set of random measurement functions/masks are used in CS [1, 2]. However, it has been noted that random projections do not work well at low signal-to-noise ratios (SNR) or at low sampling rates [6, 7]. In this chapter, we used an optimized mask set, aiming to reduce further the number of necessary measurements, while still retaining the quality of the reconstructed image. In brief, the binary masks are optimized to approximate the Karhunen-Loeve transform (KLT). The idea is quite similar to that of [8] where the 2D discrete cosine transform is quantized with the ternary set {1,0,-1}. Specifically, we assumed that the autocorrelation matrix R_{xx} of the input image follows the isotropic 2D model with correlation coefficient 0.95 [9]. The $M \times N$ floating-coefficient KLT matrix *U* is then obtained through the eigenvalue decomposition of R_{xx}. After that, we used MATLAB 7.0 to search an optimal threshold *T* so that the binary matrix $\Phi(k,l)$

defined below yields the maximum coding gain (coding gain is the effective gain which is usually measured as the dB difference between a coded and uncoded signal producing the same bit error rate) [9],

$$\Phi(k,l)=\begin{cases}1, & U(k,l)>T,\\ 0, & \text{otherwise}.\end{cases} \tag{4.1}$$

The binary matrix $\Phi(k,l)$ was then used to make the masks.

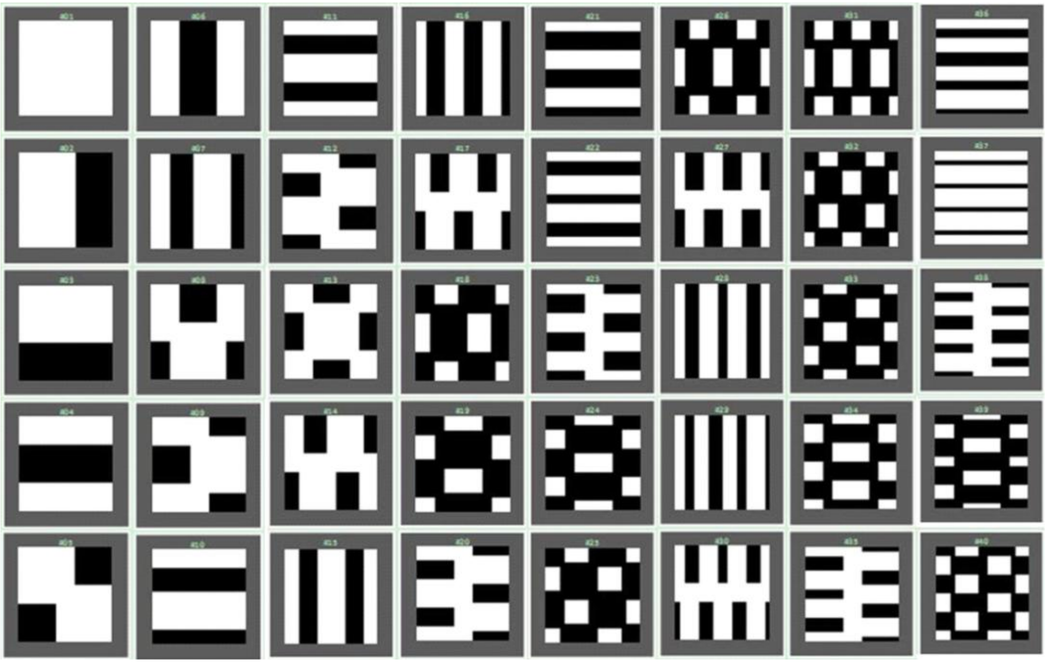

Figure. 4.1 Optimized mask set for CS-THz system.

Figure. 4.1 shows all 40 masks used in our experiment. The masks each comprised 20×20 pixels and were constructed from self-supported copper tape. Each pixel had dimensions of 2.0 mm×2.0 mm, thus providing a 40.0 mm×40.0 mm imaging area. It was confirmed that the pixels were either totally transparent or totally opaque to THz radiation. The lack of a supporting substrate eliminates possible THz absorption/dispersion or phase delays in propagation through the transparent pixels, making this design ideal for broadband spectroscopic imaging applications.

Figure. 4.2 Simulated results demonstrating the universality of the proposed mask. (a) Original image and reconstructed images using (b) 40 optimized masks, (c) 40 random masks, and (d) 120 random masks [5].

It should be emphasized that our mask optimization is based on a general isotropic 2D model, rather than being based on a training set of images. Thus, our masks are generically applicable to a wide range of samples. Indeed, extensive computer simulation demonstrates that our binary approach offers good visual quality for most 20×20 image patches. Figure. 4.2 (b) shows one set of such example images obtained using the 40 optimized masks of the test objects shown in Figure. 4.2 (a). In particular, the far-right panel of Figure. 4.2 shows the image obtained of two light points against a dark background and demonstrates that reasonable image quality is obtained using the mask set in this extreme case. As a comparison, Figures. 4.2 (c) and (d) shows images reconstructed using 40 and 120 random masks, respectively. As expected, the optimized masks outperform the random masks at this low sampling rate (10%, i.e., 40 measurements for images comprising 20×20 pixels). The quality of the reconstructed images can be improved by increasing the number of random masks from 40 (a sampling rate of 10%) to, for example, 120 (a sampling rate of 30%), although the measurement time will increase. From simulated results, it is proved that we can obtain great reconstruction images with less number of measurements by using these 40 optimized masks than that by using random masks. In the next section, we will develop this mask set into the physical experimental setup.

4.2 CS-THz Experiment using IR Light Source

4.2.1 Experimental Setup

IR light source was first used to demonstrate the idea of CS-THz using a set of independent optimized masks. Figure. 4.3 shows the schematic diagram of the compressive imaging system using IR light source. An IR LED and a photodiode were used as the light source and the detector, respectively. The IR light from a source was collimated using a parabolic mirror. After propagating through the masks and sample, the IR beam was then focused, by using another parabolic mirror, onto the detector. Similar to that in previous studies, a single-point detector is utilized to measure the signal. Data acquisition (DAQ) card (National Instrument USB-6221) is used to collect the signal recorded from detector and send it to PC for image reconstruction. In our experiments, all the samples were made of self-supported copper tape. Limited by the diameter of parabolic mirror, the image window is of size 40.0 mm×40.0 mm.

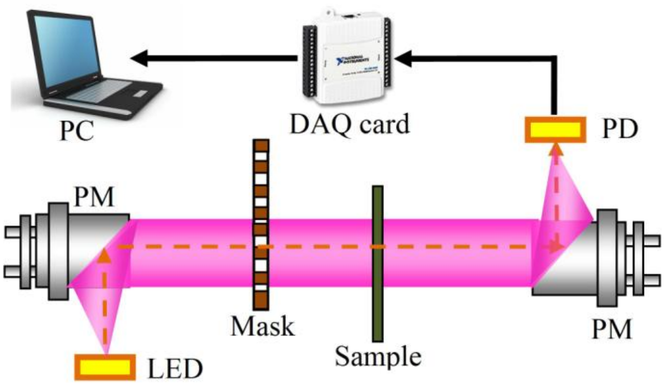

Figure. 4.3 Schematic diagram of the compressive imaging system (PM: parabolic mirror, LED: light emitting diode, PD: photodiode, DAQ: data acquisition).

4.2.2 Experimental Results

Figure. 4.4 shows the simulated and reconstructed results ($y_{M\times 1} = \Phi_{M\times N} x_{N\times 1}$)

comparison using 40 optimized masks. The 20×20 original image $x_{N\times1}$ is presented in the left-hand inset. It is clear to see that the reconstructed results are highly close to the simulated results, thus the reconstructed image $\hat{x}_{N\times1} = \hat{\Phi}_{N\times M} y_{M\times1}$ (right-hand inset) is easily obtained. In this case, *M*=40, *N*=400, and again, the reconstructed IR image can be identified when *M*<<*N*.

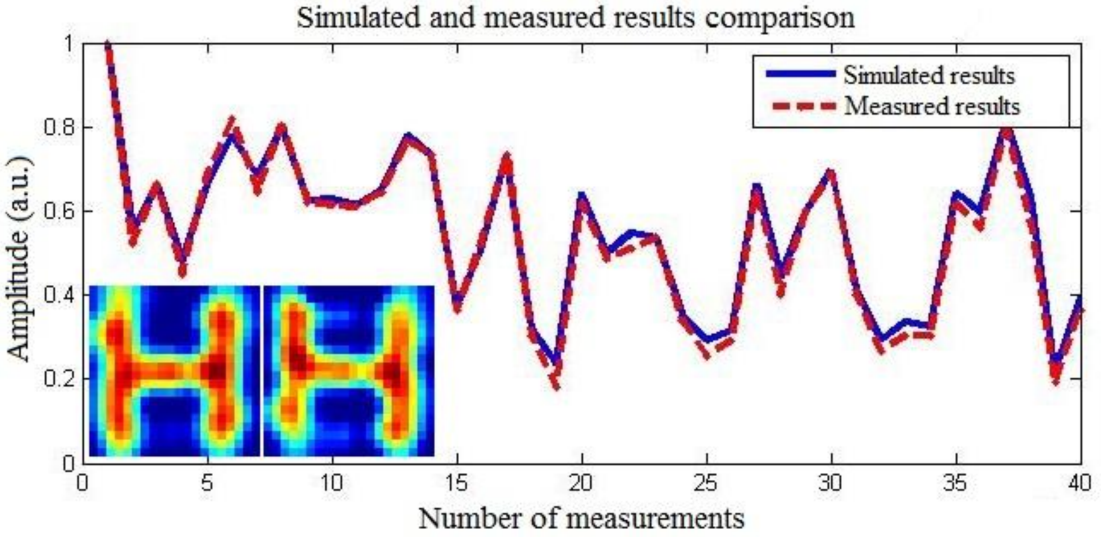

Figure. 4.4 Simulated results for linear measurements. The left-hand inset image is the simulated results and the right-hand inset image is the reconstructed image using 40 optimized masks.

Figure. 4.5 shows, as examples, the IR images of English characters T, H, A, M and G reconstructed by 40 optimized masks. The dark areas (in blue) correspond to the opaque copper tape, and the bright areas (in red) correspond to the cut-through holes. In all cases, with MMSE linear estimation, all the characters can be easily recognized with only 10% sampling rate. For relatively much sparse signals, such as "T", "H" and "A", it offers high quality of reconstructed images. However, due to the limited image resolution, for relatively less sparse signals (i.e., images consist of relatively more sharp areas), such as "M" and "G", the reconstruction performance becomes worse. Certain parts of information around sharp areas which are not such sparse were missed in the reconstruction procedure.

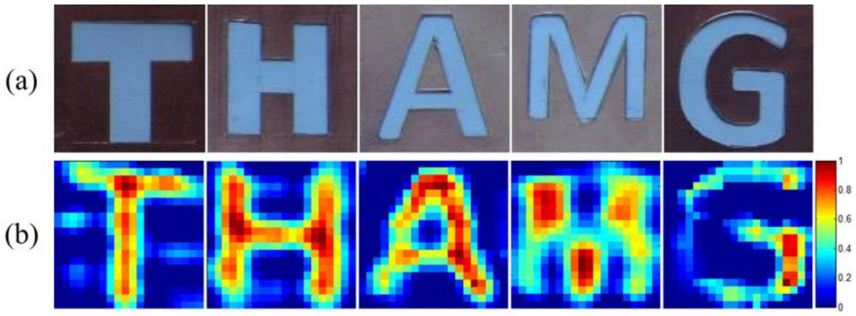

Figure. 4.5 (a) Photographs of the samples shaped as "T", "H", "A", "H" and "G" used in IR imaging experiment, and their corresponding IR images reconstructed using (b) MMSE linear estimation. Each image has 20×20 pixels and was reconstructed by 40 optimized masks.

One of the easiest and most useful methods to solve this problem is to increase the resolution of the mask set. Here we extend the original 20×20 pixels imaging area to be an 80×80 pixels area. Similar to the block CS method [10], the 80×80 pixels image is divided into four 20×20 pixels areas and each block is sampled independently using the same 40 optimized mask set. Figure. 4.6 shows the reconstructed 20×20 pixels and 80×80 pixels IR images shaped as "E", respectively. Two reconstruction algorithms, i.e., MMSE linear estimation [10, 11] and the total variation minimization (TV-min) nonlinear reconstruction algorithm [12] have been investigated. Compared with Figure. 4.6 (b) and (d), even with MMSE linear estimation, the reconstructed 80×80 pixels IR images perform much better reconstruction quality than the 20×20 pixels images.

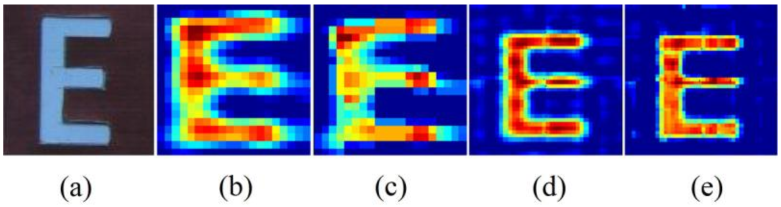

Figure. 4.6 (a) Photographs of the samples shaped as "E" used in IR imaging experiment. Their corresponding 20×20 pixels IR images are reconstructed using (b) MMSE linear estimation and (c) TV-min nonlinear reconstruction algorithm. The extended 80×80 pixels IR images are reconstructed using (d) MMSE linear estimation and (e) TV-min nonlinear reconstruction algorithm.

4.3 CS-THz Experiment using BWO THz Source

4.3.1 Experimental Setup

As a further demonstration that the developed compressed imaging system is also applicable to THz imaging, we used a backward wave oscillator (BWO) source (Insight Product Company, USA) which provides electromagnetic radiation at 0.14 THz. The schematic diagram of this system is illustrated in Figure. 4.7. The detector used was SPH-49 (Spectrum Detector Inc. USA).

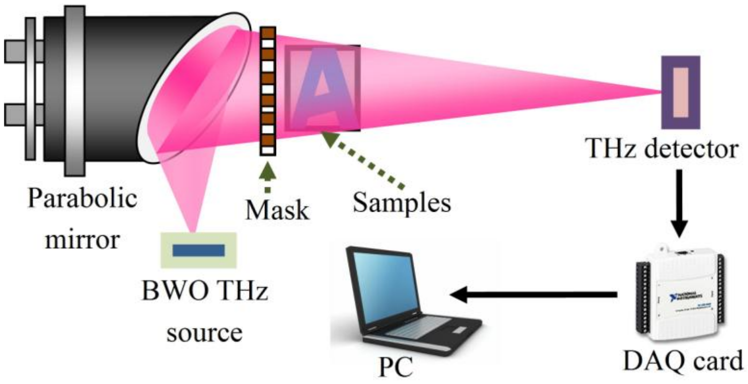

Figure. 4.7 Schematic diagram of the compressed THz imaging system using BWO source.

4.3.2 Experimental Results

Similar to that in [13], we reported a THz imaging system using BWO as a radiation source. The experimental results further inspect the performance of such CS imaging system in THz range. Figure. 4.8 shows the THz images reconstructed using simulated signals and measured signals. With MMSE linear reconstruction, although the THz radiation is not that uniform in the whole imaging window (the signal in upper area is relatively weak), all the characters are visually recognizable. From section 4.2.2 and this section, as this CS imaging system works great in both IR and THz range, we can further develop this proven technique into TPI system to replace the conventional raster scan method.

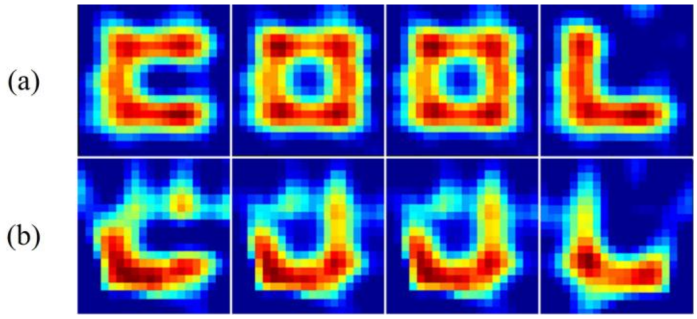

Figure. 4.8 THz images reconstructed using (a) simulated signals and (b) measured signals. Each character of this sample shaped as "COOL" is respectively reconstructed using 40 optimized masks. Each image has a 20×20 pixels with a pixel size of 2.0 mm×2.0 mm. A BWO source at 0.14 THz was used to illuminate the sample and the transmitted THz radiation was measured using a single-element pyroelectric sensor.

4.4 CS-THz Time-Domain (pulsed) Spectroscopic Imaging Experiment

4.4.1 Experimental Setup

Aiming to obtain both a spatial and spectral features of a sample, we developed Figure. 4.3 into a time-domain (pulsed) THz spectroscopic imaging system. Figure. 4.9 shows our experimental arrangement, which is similar to that typically used for the coherent generation and detection of broadband THz radiation [14]. A Ti:sapphire laser provides visible/near-infrared pulses of 12 fs duration at a center wavelength of 790 nm with a repetition rate of 76 MHz. The output is split into two parts: a 330 mW beam is used for THz generation and a 40 mW beam serves as the probe beam for THz detection. THz radiation is generated from a low-temperature-grown (LTG) GaAs photoconductive emitter with an electrode gap of 0.4 mm and is biased using a 10 kHz square wave of peak amplitude ±100 V. The THz pulses emitted (in the “reflection” geometry [14]) are collimated and focused onto a 1.0-mm-thick (110) ZnTe crystal for electro-optic detection. Only one pair of parabolic mirrors is required for imaging using the compressive sampling technique as the sample (and the binary masks) is placed in a collimated THz beam. In our experimental arrangement, however, we retained two pairs of parabolic mirrors to allow conventional THz-TDS measurements to allow, in addition, conventional THz-TDS measurement to be performed.

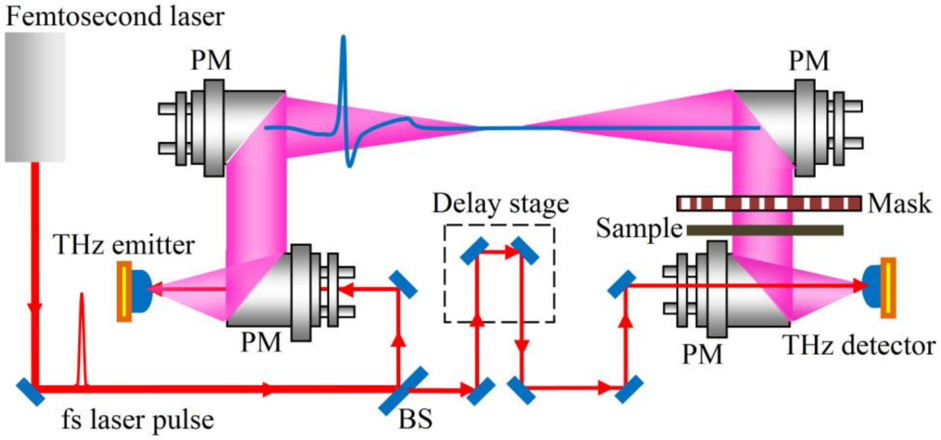

Figure. 4.9 Experimental arrangement for TPI using compressive sampling. Each of 40 masks has a 40.0 mm×40.0 mm imaging area. The copper pixels are opaque to THz radiation while the white pixels are transparent to THz radiation. (BS: beam splitter, PM: parabolic mirror) [5].

4.4.2 Experimental Results

As mentioned in the chapter 2, the THz frequency region of the electromagnetic spectrum offers a unique combination of properties. Many crystalline substances possess sharp characteristic spectral features in this frequency range associated with both inter- and intramolecular vibrational modes [15, 16]. This, when coupled with the ability of THz radiation to propagate through common barrier materials, such as clothing and packaging, makes THz imaging and spectroscopy a potentially powerful tool for nondestructive determination of the chemical composition and physical structure of a concealed sample [17]. Here, for the first time, the CS-THz time-domain (pulsed) spectroscopic imaging has been demonstrated to obtain both a spatial and spectral characteristics of a sample. Similar to [1, 2], based on the experimental setup of compressed TPI from Figure. 4.9, CS has been proposed to reduce the number of measurements and acquisition time, rather than the conventional raster scan method which is time-consuming.

Figure. 4.10 shows an example of experimental results for TPI. The original image, which has a 20×20 pixels with a pixel size of 2.0 mm×2.0 mm, is made by copper tape in Figure. 4.10 (a). The THz beam penetrating the sample and one of the 40 masks was converted to the THz electric field and then recorded as a function of time delay using the time-domain spectroscopy system. In total, 40 THz waveforms were measured; one for each of the 40 masks. Each waveform was Fourier transformed into the frequency domain, and the THz amplitude at a selected frequency was used for image reconstruction. As can be seen, the Chinese character "big" can be reconstructed in both spatial domain and spectral domain at different THz frequencies from 0.15 THz to 2.0 THz.

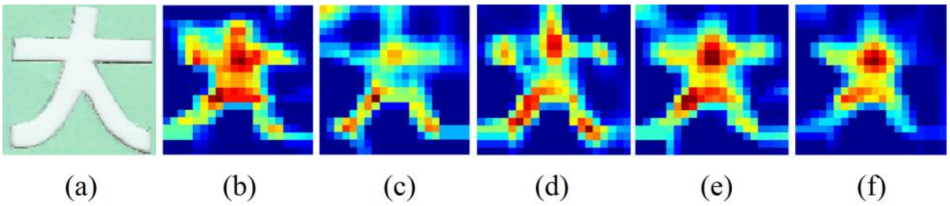

Figure. 4.10 (a) Original 20.0 mm×20.0 mm image of a Chinese character "big". (b) Spatial domain reconstruction. (c)-(f) Reconstructed image at 0.15, 0.3, 1.0 and 2.0 THz. All image have 20×20 pixels and the pixel size is 2.0 mm×2.0 mm.

Similarly, aiming to obtain the chemical mapping of samples, a sample comprising regions of polyethylene, lactose, and copper tape (Figure. 4.11 inset) was placed in the collimated THz beam path together with one of the 40 optimized masks, and also the THz electric field was recorded as a function of time delay using the time-domain spectroscopy system. Measurements were performed at room temperature with dried air purging to exclude water vapor. In all measurements, the variable delay stage, which provides the time delay between the THz pulse and probe pulse, was scanned over a distance of 5.0 mm, providing a spectral resolution of 0.03 THz. Again, all the 40 THz waveforms corresponding to each of the 40 masks was Fourier transformed into the frequency domain, and the THz amplitude at a selected frequency was used for image reconstruction.

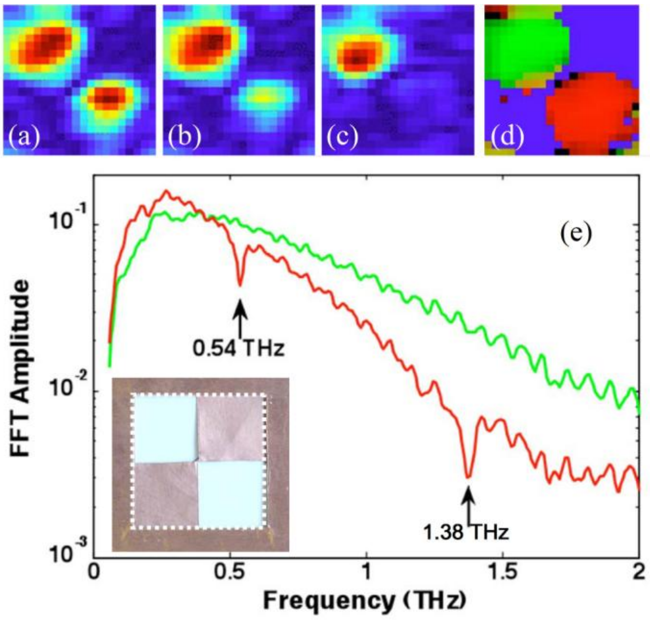

Figure. 4.11 (a)-(c) Reconstructed THz images of the sample at 0.50, 0.54, and 1.38 THz, respectively. Each image is 40.0 mm×40.0 mm. (d) RGB chemical map of the sample where red is assigned to lactose, green to polythene, and blue to regions of no transmission (copper areas). (e) THz spectra of polyethylene (upper trace) and lactose (lower trace). The inset shows a photograph of the sample that is made of copper tape with two square holes (each 20.0 mm×20.0 mm). A 3.0-mm-thick polyethylene pellet is placed at the top-left square while a 3.2-mm-thick lactose pellet is placed at the bottom-right square [5].

Figure. 4.11 (a)-(c) show the THz images reconstructed at frequencies of 0.50, 0.54, and 1.38 THz. At 0.5 THz, the absorption of both polyethylene and lactose is minimal, and this is reflected in the reconstructed image in which two bright regions are observed corresponding to strong THz transmission through both materials (Figure. 4.11 (a)). The dark areas correspond to the opaque copper tape. Lactose monohydrate powder has tow well-defined strong absorption features at 0.54 and 1.38 THz [18]. Consequently, at these two frequencies, the reconstructed sample image shows a much weaker transmission for the lactose (bottom-right square of Figures. 4.11 (b) and (c)).

A major advantage of THz-TDS is that the transient electric field, rather than the radiation intensity, is measured as a function of time. This coherent detection scheme not only yields a THz signals with excellent SNR and high dynamic range, but also preserves the important phase information. This enabled us to measure a THz spectrum at each pixel in the image. Figure. 4.11 (e) shows the calculated THz spectra of the lactose and polyethylene, determined by averaging over an area of 4×4 pixels at the centers of the lactose (top-left square) and polyethylene (bottom-right square) regions. Two well-defined absorption features are observed in the lactose spectrum at 0.54 and 1.38 THz, which agree well with the published data [19]. To the best of our knowledge, this represents the first combined THz imaging and spectroscopic measurement using a binary mask set. Furthermore, as a THz spectrum was obtained for each pixel of the image, spatially resolved chemical maps of the sample can be obtained by using cosine correlation mapping [20]. For a better visualization of the chemical distributions in the sample, the extracted chemical maps are displayed as a red-green-blue (RGB) map [20]. Figure. 4.11 (d) demonstrates that in this way the chemical distribution of the lactose and polyethylene can be clearly distinguished.

4.5 Summary

In conclusion, we have reported the experimental implementations of both IR and THz imaging, especially for THz time-domain (pulsed) spectroscopic imaging, using an optimized binary mask set. The time-domain (pulsed) THz spectroscopic imaging is possible using a single-point detector and CS, allowing a spatial and chemical map of sample to be obtained. This significantly reduces the number of measurements required to form an image, with a commensurate reduction in image acquisition time. Furthermore, we have been able to demonstrate image reconstruction over a far greater frequency range (up to 2.0 THz), which is of considerable significance for a broad range of imaging applications. For the future work, considering the pixel number of masks is only 20×20 pixels, we can further increase the pixel number of masks to obtain higher resolution reconstructed images. Also, for the time being, all the 40 masks are changed manually, we can improve the system which enables the measurement to be done automatically and continuously, idea for real-time THz imaging application.

References:

[1] W. L. Chan, K. Charan, D. Takhar, K. F. Kelly, R. G. Baraniuk, and D. M. Mittleman, "A single-pixel terahertz imaging system based on compressed sensing," *Appl. Phys. Lett.*, vol. 93, no. 12, 121105, 2008.

[2] W. L. Chan, M. L. Moravec, R. G. Baraniuk, and D. M. Mittleman, "Terahertz imaging with compressed sensing and phase retrieval," *Opt. Lett*. vol. 33, no. 9, pp. 974-976, 2008.

[3] D. L. Donoho, "Compressed sensing," *IEEE Trans. Inf. Theory,* vol. 52, no. 4, pp. 1289-1306, 2006.

[4] E. J. Candès, J. Romberg, and T. Tao, "Robust uncertainty principles: Exact signal reconstruction from highly incomplete frequency information," *IEEE Trans. Inf. Theory*, vol. 52, no. 2, pp. 489-509, 2006.

[5] Y. C. Shen, L. Gan, M. Stringer, A. Burnett, K. Tych, H. Shen, J. E. Cunningham, E. P. J. Parrott, J. A. Zeitler, L. F. Gladden, E. H. Linfield, and A. G. Davies, "Terahertz pulsed spectroscopic imaging using optimized binary masks," *Appl. Phys. Lett.*, 95, no. 23, 231112, 2009.

[6] J. Haupt and R. Nowak, "Compressive sampling vs. conventional imaging," *Proc. IEEE Intl. Conf. on Image Processing*, pp. 1269-1272, Atlanta, GA, 2006.

[7] Y. Weiss, H. S. Chang, and W. T. Freeman, "Learning compressed sensing," *Snowbird Learning Workshop*, Allerton, 2007.

[8] N. P. Pitsianis, D. J. Brady, and X. Sun, "Sensor-layer image compression based on the quantized cosine transform," *Proc. SPIE,* vol. 5817, pp. 250-257, 2005.

[9] J. Liang, X. Li, G. Sun, and T. D. Tran, "Two-dimensional wiener filters for error resilient time domain lapped transform," *the 31st IEEE International Conference on Acoustics, Speech, and Signal Processing (ICASSP),* vol. III, pp. 241-244, Toulouse, France, 2006.

[10] L. Gan, "Block compressed sensing of natural images," *in Proc. Int. Conf. Digital Signal Processing*, pp. 403-406, Cardiff, UK, 2007.

[11] J. Ke and M. A. Neifeld, "Optical architectures for compressive imaging," *Applied Optics*, vol. 46, no. 22, pp. 5293-5303, 2007.

[12] E. J. Candès, J. Romberg, and T. Tao, "Robust uncertainty principles: Exact signal reconstruction from highly incomplete frequency information," *IEEE Trans. Inf. Theory*, vol. 52, no. 2, pp. 489 - 509, 2006.

[13] A. Dobroiu, M. Yamashita, Y. N. Ohshima, Y. Morita, C. Otani, and K. Kawase, "The backward wave oscillator as a radiation source in terahertz imaging," *conference digest of the 2004 joint 29th international conference on infrared and millimeter waves and 12th international conference on terahertz electronics*, pp. 825-826, Karlsruhe, Germany, 2004.

[14] Y. C. Shen, P. C. Upadhya, E. H. Linfield, H. E. Beere, and A. G. Davies, "Ultrabroadband terahertz radiation from low-temperature-grown GaAs photoconductive emitters," *Appl. Phys. Lett.*, vol. 83, no. 15, pp. 3117-3119, 2003.

[15] M. Walther, B. Fischer, M. Schall, H. Helm, and P. U. Jepsen, "Far-infrared vibrational spectra of all-trans, 9-cis and 13-cis retinal measured by THz time-domain spectroscopy," *Chem. Phys. Lett*. vol. 332, no. 3-4, pp. 389-395, 2000.

[16] Y. C. Shen, P. C. Upadhya, E. H. Linfield, H. E. Beere, and A. G. Davies, "Temperature-dependent low-frequency vibrational spectra of purine and adenine," *Appl. Phys. Lett.*, vol. 82, no. 12, pp. 2350-2352, 2003.

[17] A. G. Davies, A. D. Burnett, W. Fan, E. H. Linfield, and J. E. Cunningham, "Terahertz spectroscopy of explosives and drugs," *Mater. Today*, vol. 11, no. 3, pp. 18-26, 2008.

[18] J. Liang, X. Li, G. Sun, and T. D. Tran, "Two-dimensional wiener filters for error resilient time domain lapped transform," *the 31st IEEE International Conference on Acoustics, Speech, and Signal Processing (ICASSP)*, vol. III, pp. 241-244, Toulouse, France, 2006.

[19] E. R. Brown, J. E. Bjarnason, A. M. Fedor, and T. M. Korter, "On the strong and narrow absorption signature in lactose at 0.53 THz," Appl. Phys. Lett., vol. 90, no. 6, 061908, 2007.

[20] Y. C. Shen and P. F. Taday, "Development and application of terahertz pulsed imaging for non-destructive inspection of pharmaceutical tablet," *IEEE J. Sel. Top. Quantum Electron*. vol. 14, no. 2, pp. 407-415, 2008.

Chapter 5

CS-THz System using a Single Spinning Disk

Motivated by the CS theory several single-pixel cameras [1-4] have been developed. Most of existing works use a random Bernoulli operator, in which the entries of Φ are random selected as 0 and 1 with equal probability. In such systems, a set of independent two-dimensional random binary masks are required, each of which corresponds to one row of Φ. Despite their theoretical advantages, there are a couple of practical limitations. First, as each row of Φ is independent, the imaging speed is limited by the slow translation of one random pattern to another [2, 3]. Second, a fully random binary operator incurs high computational complexity and huge memory, especially for high-resolution imaging [4].

To solve these problems, in our work [5], we proposed the use of a single rotating disk (similar to the Nipkow disk used in confocal microscopy [6]) for a fast single-pixel camera. The measurements in [5] were preformed in a "stop-measure-rotate" fashion by using a motorized stage to rotate the disk, and THz images were obtained using a backward wave oscillator (BWO) source operating at a single frequency of 0.14 THz. After that, in [7], we showed for the first time, to our knowledge, that a continuously spinning disk can be used for fast compressive IR imaging and TPI. This enables the measurement to be done automatically and continuously, ideal for real-time THz imaging applications.

5.1 Spinning Disk Design based on CS

Figure. 5.1 illustrates the schematic diagram of the spinning disk. This spinning disk has random binary patterns, where 0 (the black pixel) and 1 (the white pixel) have equal probabilities. During the imaging process, the whole disk s covered except for a small fixed rectangular area, which has the same dimension of reconstructed image. When spinning the disk, each effective mask is obtained from the rectangular window in green with different binary patterns (the ring area between two dashed red lines is the imaging area). Then, a set of effective masks are obtained for reconstruction.

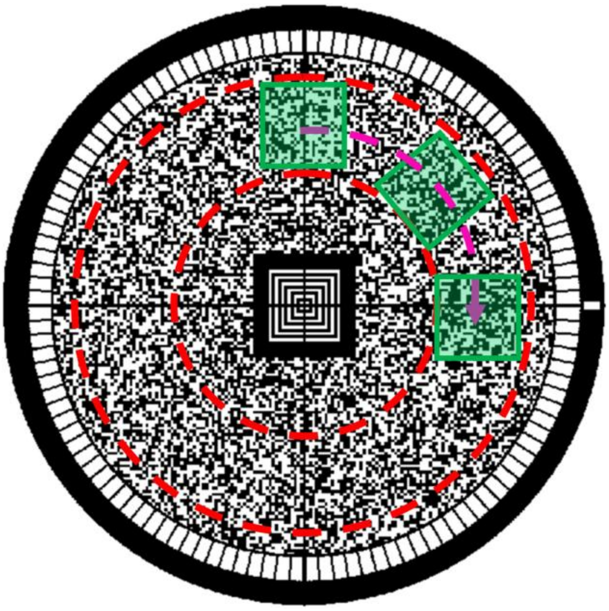

Figure. 5.1 Schematic diagram of the spinning disk. When spinning the disk, each effective mask is obtained from the rectangular window in green with different binary patterns (i.e., the area between two red dashed lines is the actual imaging area).

From a signal processing point of view, the sampling operator Φ corresponding to a spinning disk can be approximated as random block Toeplitz matrix with the following form:

$$\Phi = \begin{bmatrix} A_0 & A_1 & \cdots & A_{(L-1)} \\ A_{-1} & A_0 & \cdots & A_{(L-2)} \\ \vdots & \vdots & \ddots & \vdots \\ A_{(1-M)} & A_{(2-M)} & \cdots & A_{(L-M)} \end{bmatrix}, \tag{5.1}$$

where each $A_i(1-M<i<L-1)$ is an 1×n ($n=N/L$) random binary row vector. The parameter L (or equivalently n) depends on the rotation step α and the position of the observation rectangular area. L becomes large when α is small and when the rectangular area is close to the center of the disk. Compared with the full random matrix used in [2], Φ given above requires less storage space and yields much faster computation. More importantly, it can be easily implemented in hardware. [8] and [9] first derived that when x is a sparse signal (i.e., when the sparsifying transform Ψ is an identity matrix), the total number of measurements required is $M \geq O(K^3 \log(N/K))$. More recent results in [10] show that the bounds could be further improved to $M \geq O(K \log^2(N))$. This implies that the spinning disk implementation offers a sub-optimal theoretical bound (with an extra scaling factor of log N) when Ψ is an identity matrix. For other Ψ, there is no reported work about theoretical performance bounds of (block) Toeplitz matrix.

In order to illustrate the validation of this spinning disk approach and the robustness of the corresponding reconstruction algorithms, we compared the various of reconstructed images from the simulated signals in the presence of Gaussian white noises. Similar to that in chapter 4, both the minimum mean square error (MMSE) linear estimation [11, 12] and the total variation minimization (TV-min) nonlinear reconstruction algorithm [13] have been investigated. As we can see from Figure. 5.2, most of the reconstructed images can be easily recognized except ones using TV-min nonlinear reconstruction algorithm at relatively low signal to additive Gaussian noise ratio. Note that only 120 measurements (each of these 120 effective masks is obtained by spinning the disk for each 3 degrees) were necessary to obtain an image of 1024 pixels. This represents a 9 times reduction in measurement number and thus measurement time. We can further quantize the signal to noise ratios (SNR) for reconstructed images from Figure. 5.2 to Figure. 5.3. The SNRs for reconstructed images become greater when increasing the number of measurements or the signal to additive Gaussian white noise ratio; also they will tend to stable when in the presence of high signal to additive Gaussian noise ratio. Compared with those using MMSE linear estimation, the simulation results using TV-min nonlinear reconstruction algorithm perform much better in most of cases, especially in the presence of high signal to additive Gaussian noise ratio. However, in relatively low signal to additive Gaussian noise ratio, MMSE works better in return. So in the realistic experiment with large noises, further increase in the measurement number may decrease the quality of the reconstructed images.

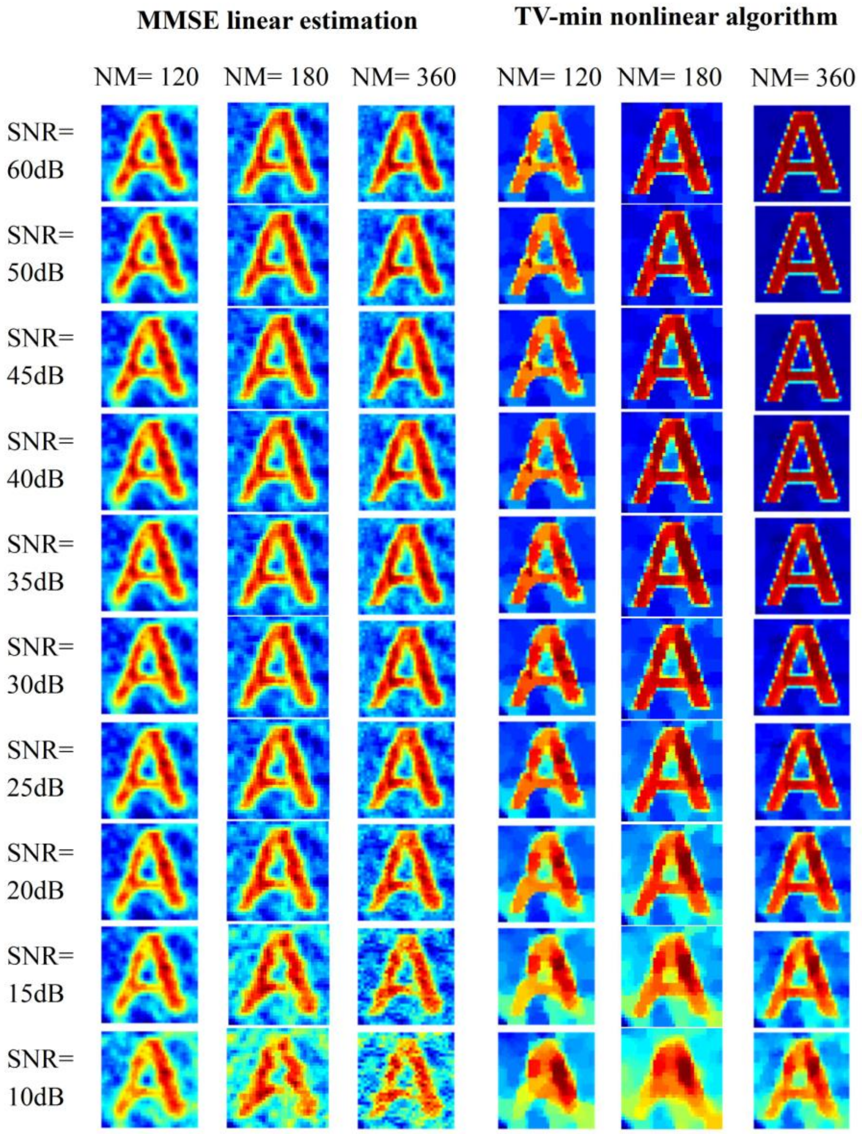

Figure. 5.2 The simulation results for reconstructing an image of English character "A" using the spinning disk configuration. Both MMSE linear estimation and TV-min nonlinear reconstruction algorithm are used. All images have 32×32 pixels. (NM: number of measurements, SNR: signal to additive Gaussian noise ratio).

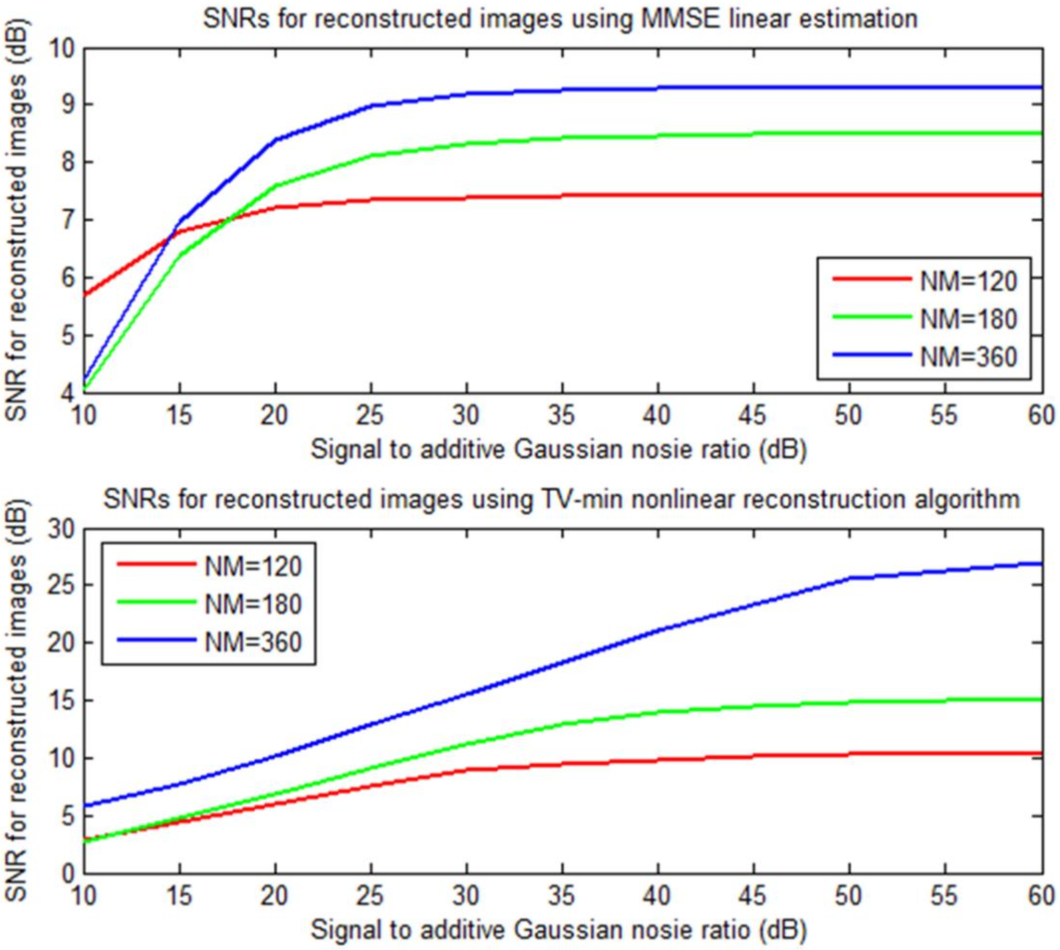

Figure. 5.3 SNRs for reconstructing an image of English character "A" using the spinning disk configuration. Both MMSE linear estimation and TV-min nonlinear reconstruction algorithm are investigated. (NM: number of measurements, SNR: signal to noise ratio).

Figure. 5.4 presents the SNR comparison for reconstructed images using full random operators (FRO) and spinning disk configuration (SDC). As expected, the quality of the reconstructed images could be improved by increasing the number of measurements. For spinning disk configuration, it is about 2-5 dB degradation with regard to the full random operators. This spinning disk implementation could yield similar performance as Gaussian random operators (the theoretically ideal operator in CS theory). The inset reconstructed images are easily obtained using 360 measurements. With the theoretical validation of the spinning disk configuration, we will develop it into the experimental implementation in the next section.

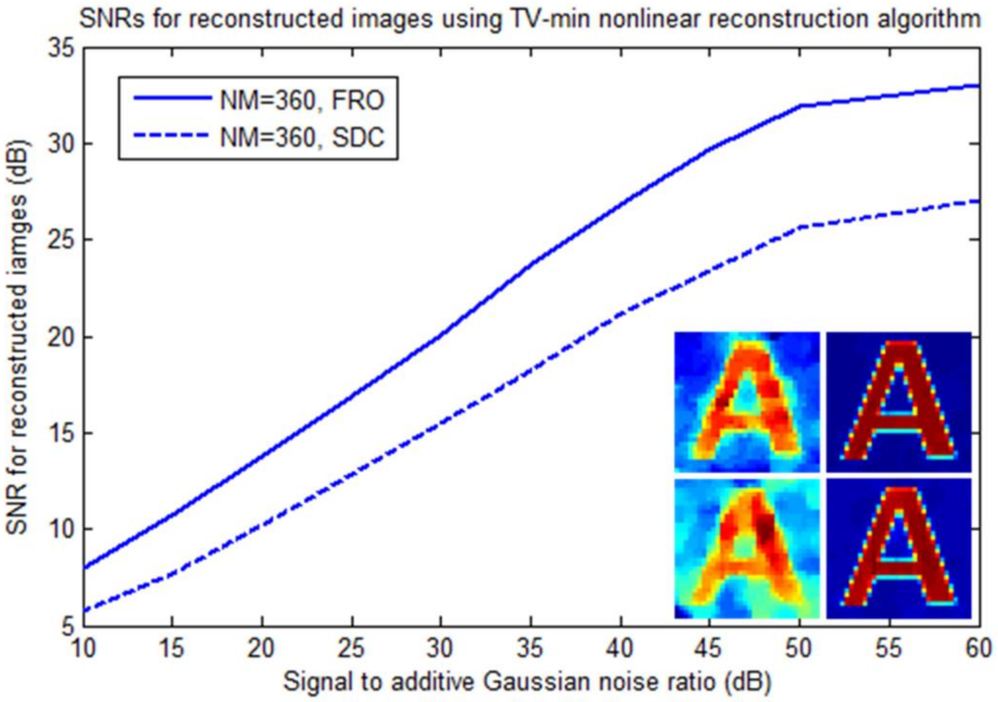

Figure. 5.4 SNRs comparison for reconstructed images using spinning disk configuration (SDC) and full random operator (FRO). TV-min nonlinear reconstruction algorithm is used. For SDC, it is about 2-5 dB degradation with regard to the FRO. The insets show the reconstructed images using 360 measurements: the top two images are reconstructed using FRO and the bottom two are recovered using SDC, both at 10 dB and 60 dB signal to additive Gaussian noise ratio. (NM: number of measurements, SNR: signal to noise ratio).

5.2 CS-THz Experiment using IR Light Source

5.2.1 Experimental Setup

Although some theoretical results about (block) Toeplitz measurement operator were investigated in literature [8-10, 14, 15], their practical applications in compressive imaging applications, especially hardware implementations are still under development. Here we developed the first spinning disk configuration into experimental implementation.

Figure. 5.5 shows the schematic diagram of a spinning disk based compressive imaging system. Also, a photo of such compressive IR imaging system is presented in

Figure. 5.6. As expected, during the imaging process, the whole disk is covered except for a small fixed rectangular area. Each time the disk is rotated by α deg, the inner product between the object and the rectangular area is measured using a single detector. As a further illustration, we provided a video demonstration [16] to explain the spinning disk imaging process, and to demonstrate how the quality of the reconstructed images progressively improves as the number of measurements increased. Note that, at each rotation angle, the new binary pattern inside the rectangular is shifted version of the previous pattern with only a small number of elements added in. So the corresponding sampling operator Φ could thus be approximated as a Toeplitz block matrix which is discussed above.

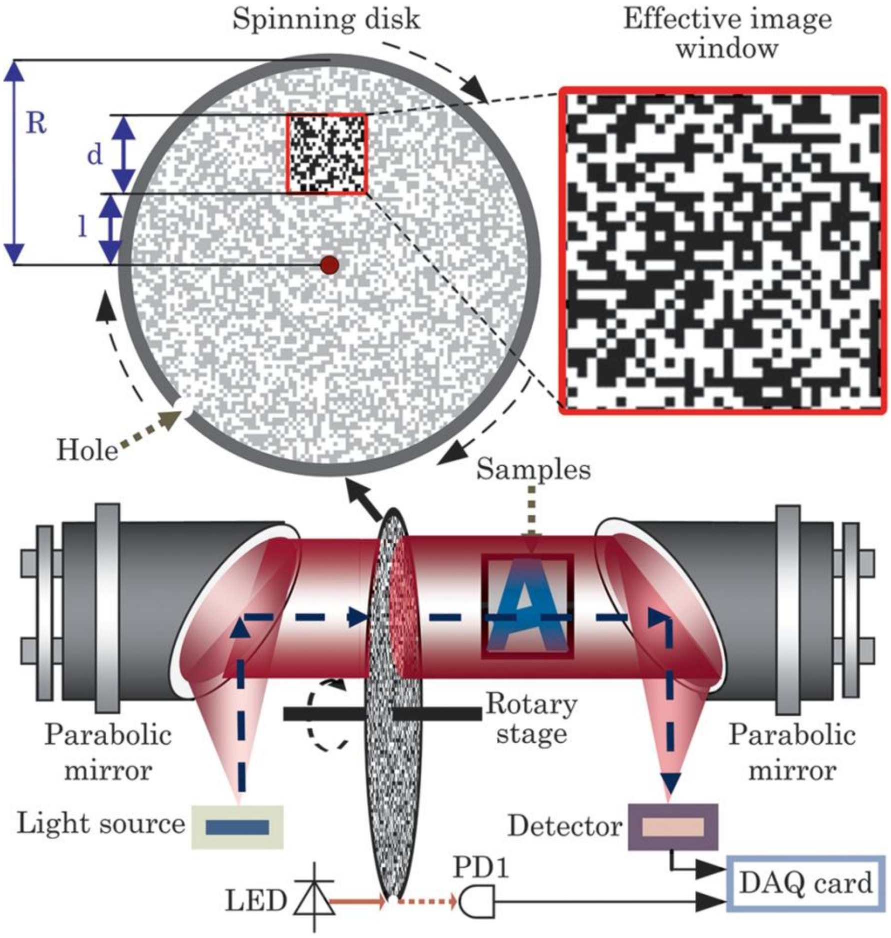

Figure. 5.5 Schematic diagram of a spinning disk based compressive imaging system. The square enclosed by the solid red line represents the "effective image window". In our experiment, the spinning disk has a radius of R=95.0 mm and the image window is placed *l*=35.0 mm from the center of the disk. A hole of 0.5 mm diameter at the edge of the spinning disk is used for synchronizing the mask position and the measured signal. (LED: light emitting diode, PD1: photodiode, DAQ: data acquisition) [7].

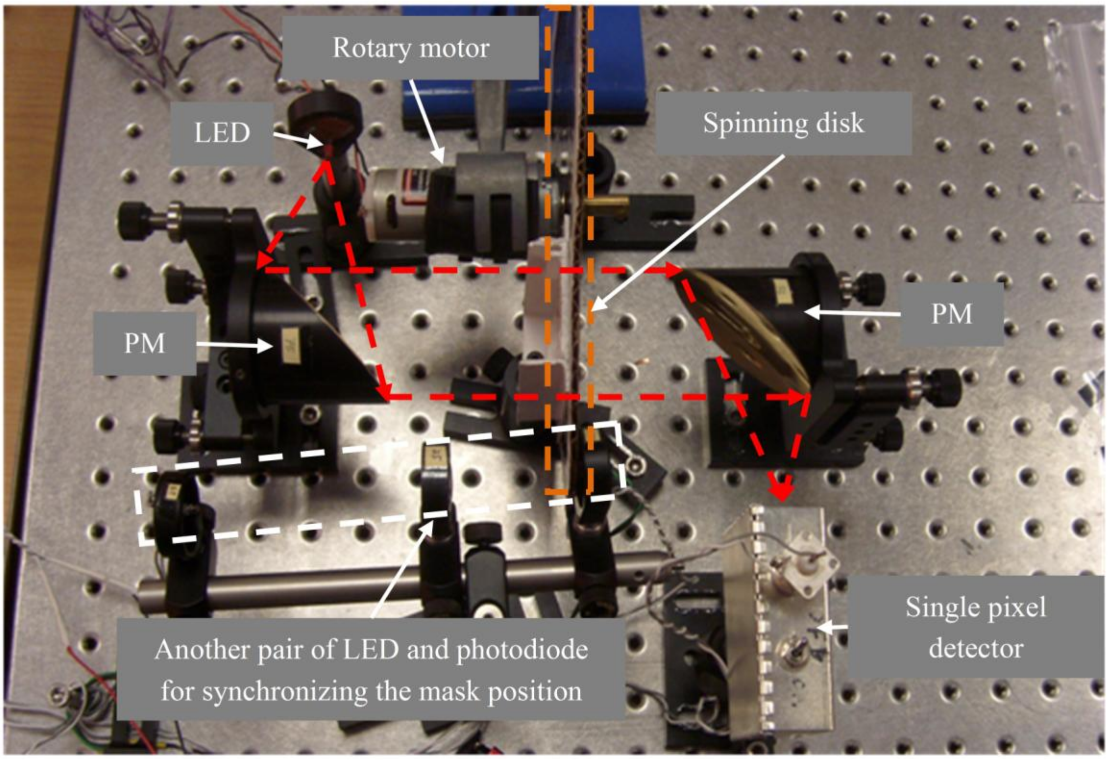

Figure. 5.6 Photo of a spinning disk based IR compressive imaging system. A pair of LED and photodiode in white dashed square, together with a hole of 0.5 mm diameter at the edge of the spinning disk, are used for synchronizing the mask position and the measured signal. (LED: light emitting diode, PM: parabolic mirror).

In our IR experiment, an IR LED and a photodiode were used as the light source and the detector, respectively. The IR light from a source was collimated using a parabolic mirror. After propagating through the sample and the spinning disk, the IR beam was then focused, by using another parabolic mirror onto the detector. All the samples were made of copper tape on a plastic plate and the spinning disk was fabricated by simply printing the designed binary patterns on a transparent plastic sheet. This spinning disk has a radius of R=95.0 mm and the imaging window is placed l=35.0 mm from the center of the disk (Figure. 5.5). The effective image window has a dimension of 32×32 (1024 pixels in total). The spatial resolution of the image is mainly limited by the pixel size, which is much larger than the wavelength of the IR radiation used here.

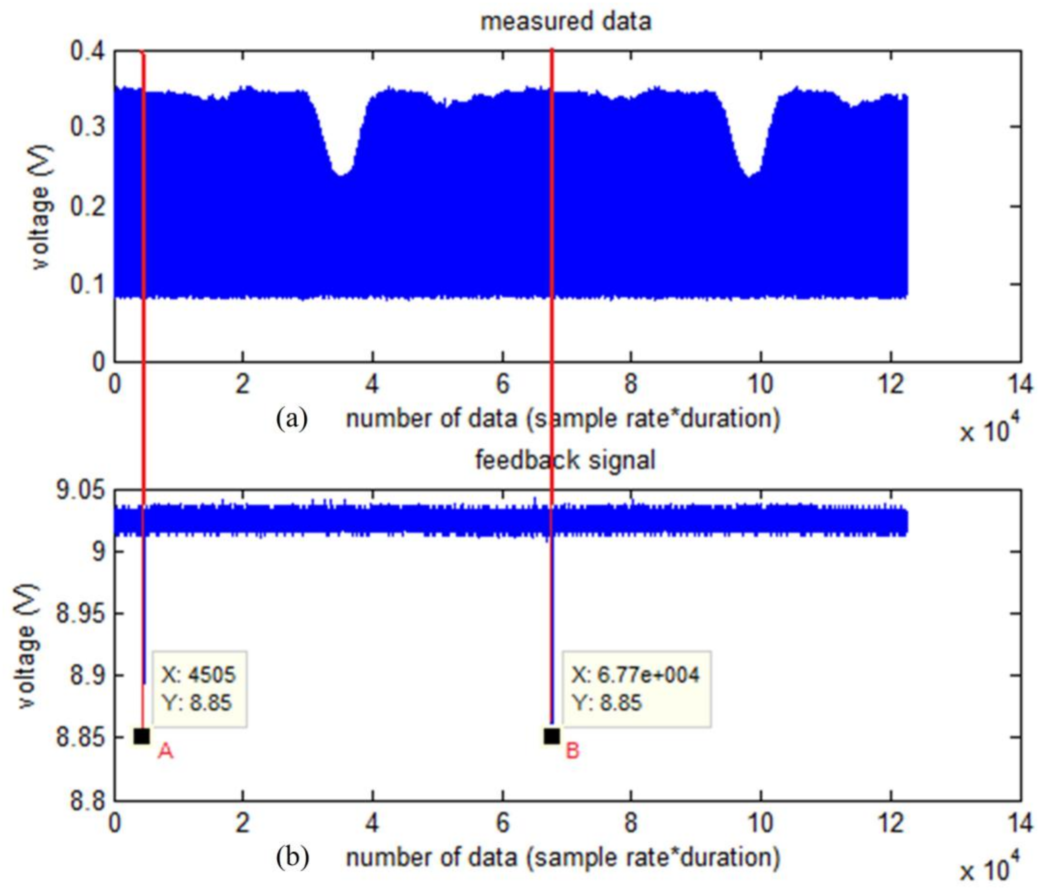

Figure. 5.7 Synchronizing the disk rotation with data measurement by comprising the measured data from detector and the feedback signal from photodiode (PD1). (a) Measured data for reconstruction. (b) Feedback signal for synchronization.

One important issue is how to synchronize the disk rotation with data measurement. To achieve this, we put a hole of 0.5 mm diameter near the edge of the spinning disk. An LED and a photodiode (PD1 in Figure. 5.5) were then used to monitor the disk rotation. The signal recorded using PD1 provides information about the relative masks positions for the data acquisition (DAQ) card. Concretely, from Figure. 5.7, once the spinning disk is rotated to the position of the hole which near the edge of the spinning disk, we will obtain an peak value such as that in the position "A" and "B" in the figure. From each peak value to the next one (i.e., from the start position to the end position of every 360 degrees), we can easily monitor the positions corresponding to each measurement (effective masks). Hence, the system can effectively measure the CS samples while continuously spinning the disk.

Also, two reconstruction algorithms, i.e., the MMSE linear estimation [11, 12] and the TV-min nonlinear reconstruction algorithm [13] have been investigated. Note that CS requires nonlinear reconstruction [13, 17]. However, algorithms like TV-min optimization are time-consuming. To keep up with the measurement speed, we used the classical MMSE linear operator [11, 12] as an initial solution, in which the autocorrelation matrix of x follows the autoregressive model of order 1 with the autocorrelation coefficient $\rho=0.95$ [12]. The time required to reconstruct a 32×32 pixel image using MMSE reconstruction is only about 0.002 s, while that using TV-min optimization is around 5 s (hardware specification: Intel Core2 Duo CPU at 2.00 GHz, 3.00 Gbyte memory; software: MATLAB 2011a).

5.2.2 Experimental Results

Based on the experimental setup in Figure. 5.5, the experimental IR results are presented here. Figure. 5.8 shows, as examples, the IR images of English characters T, E, R, and A, and a Chinese character guo reconstructed from 240 measurements (each of these 240 effective masks is obtained by spinning the disk for each 1.5 degrees). The dark areas correspond to the opaque tape, and the bright areas correspond to the cut-through holes. One can see that, even with MMSE linear reconstruction, all the characters (including the complicated guo) are visually recognizable. As expected, better quality images could be obtained using the TV-min optimization algorithm. The imaging acquisition speed is about 1 image/s, mainly limited by the speed of the specific electric motor (940D series, MFA) used in our experiment. This achievement demonstrate the proof of the principle, also allows the measurements to be done continuously. So we can further extend such idea to the THz imaging system.

Figure. 5.8 (a) Photographs of the samples used in IR imaging experiment, and their corresponding IR images reconstructed using (b) MMSE linear estimation and (c) the TV-min nonlinear reconstruction algorithm. Each image has 32×32 pixels and was reconstructed from 240 measurements [7].

5.3 CS-THz Experiment using BWO THz Source

5.3.1 Experimental Setup

As a further demonstration that the developed compressed imaging system is also applicable to THz imaging, in our prior THz compressive imaging experiments [5], we used a BWO source (Insight Product Company, USA) which provides electromagnetic radiation at 0.14 THz. The schematic diagram of this compressive THz imaging system using BWO source is illustrates in Figure. 5.9. The detector used was SPH-49 (Spectrum Detector Inc. USA). A DSP Lock-in Amplifier (SR830, Stanford Research System, USA) was used to amplify the signal in the measurements. Figure. 5. 10 shows the photo of such compressive THz imaging system using BWO source. The power supply provides 1400 volts to generate this BWO source.

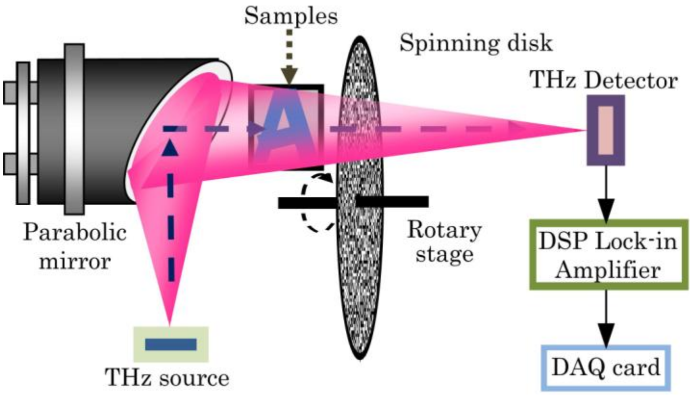

Figure. 5.9 Schematic diagram of the compressive THz imaging system using BWO source. A single rotating mask (a spinning disk) was used to modulate the THz beam.

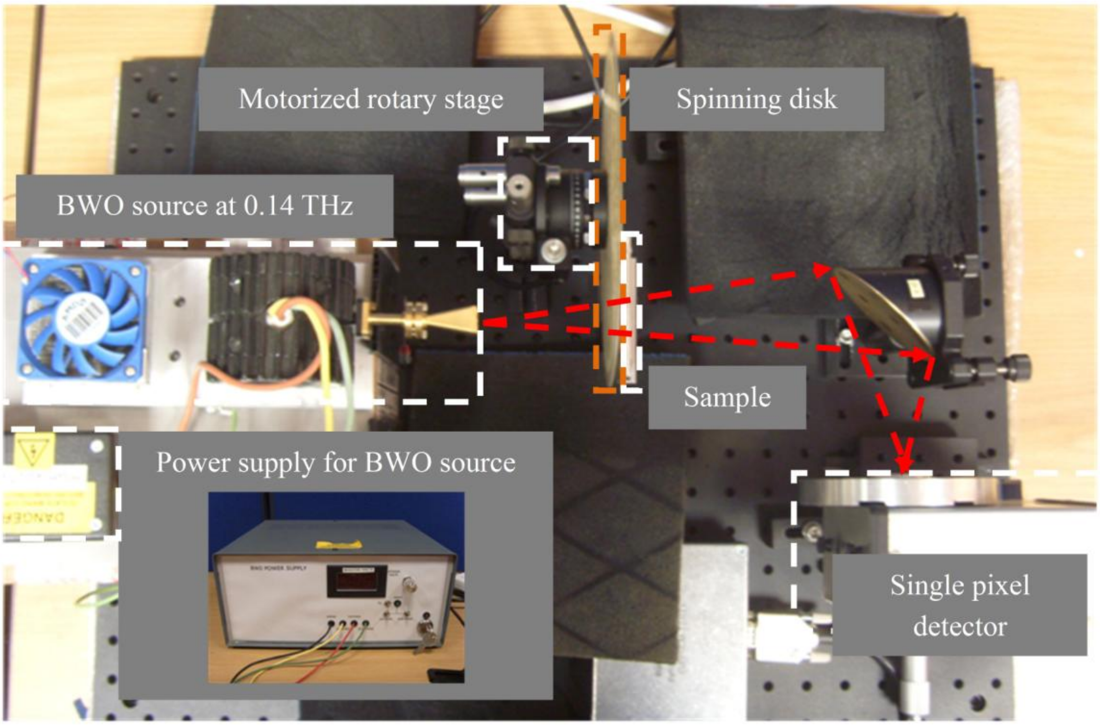

Figure. 5.10 Photo of the compressive THz imaging system using BWO source.

The THz measurements based on such setup were performed in a "stop-measure-rotate" using a motorized stage which can set the step size accurately. So in this setup, no extra components are needed to synchronize the disk rotation with data measurement. As shown in Figure. 5.11, the random binary pattern of the spinning disk was fabricated on a 0.5-mm-thick standard print circuit board (PCB).

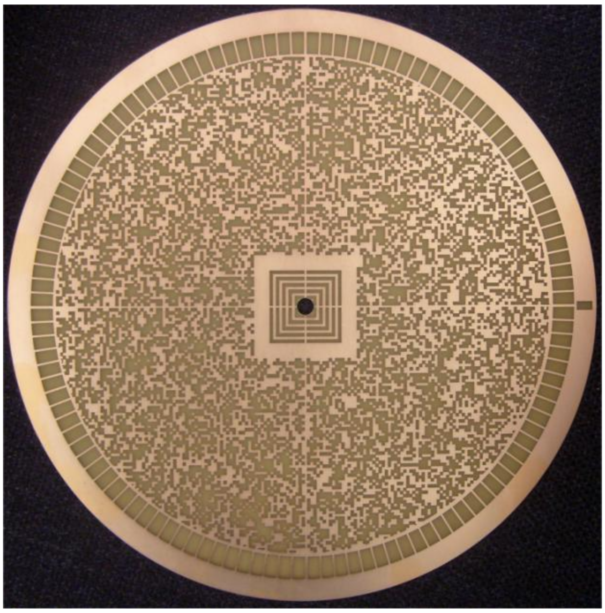

Figure. 5.11 The physical spinning disk which is fabricated on a 0.5-mm-thick standard print circuit board (PCB). The diameter of this spinning disk is 20.0 mm and each of the physical pixel is 1.0 mm×1.0 mm.

5.3.2 Experimental Results

As expected, all sample patterns which are concealed in fiber reinforced epoxy resin can be identified easily in Figure. 5.12. Here, the THz measurements were preformed in a "stop-measure-rotate" method. All the images with 1024 pixels were reconstructed from 100 measurements in about 200 seconds, which represents a significant reduction in both the measurement number and the measurement time. This is the first time for spinning disk configuration to be developed in THz imaging system. We anticipated that better image quality could be obtained by improving the SNR, and shorter image acquisition time could be achieved by using a fast THz detector.

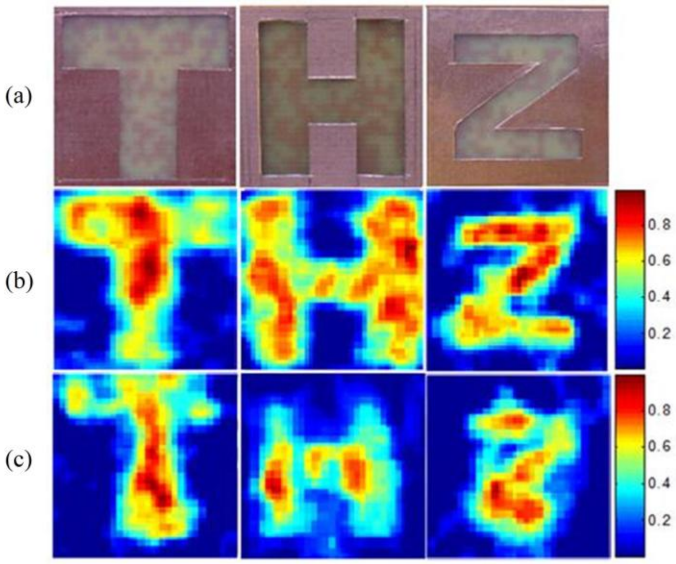

Figure. 5.12 (a) Photograph of samples, and the corresponding THz images reconstructed using (b) simulated signals and (c) measured signals. The samples used are copper tape with a cut-through pattern of "T", "H" and "z", which is concealed in fiber reinforced epoxy resin. The spinning disk was used, and the images were reconstructed from 100 measurements. Each image has a 32×32 pixels with a pixel size of 1.0 mm×1.0 mm. A BWO source at 0.14 THz was used to illuminate the sample and the transmitted THz radiation was measured using a single-element pyroelectric sensor [5].

5.4 CS-THz Time-Domain (pulsed) Imaging Experiment

5.4.1 Experimental Setup

Based on the setup in Figure. 5.13, we further developed the spinning disk configuration in a typical THz time-domain system [3]. The THz emitter was a biased photoconductive antenna [18] and the THz receiver was a ZnTe electro-optic crystal [19]; both of them were driven by femtosecond laser pulses from a Ti:sapphire laser. In the experiments, we first found that maximum THz signal (peak position) by varying the time delay between the THz pulse and the optical probe pulse using a variable delay stage. We then fixed the position of the variable delay stage at the THz peak position, and recorded the THz signal as a function of the rotation angle of the spinning disk, which, in this case, was driven by a motorized rotation stage (CR1-Z7 series, Thorlabs). The physical spinning disk is same as that used in Figure. 5.11. We found that the PCB substrate material absorbs strongly THz radiation at frequencies above 1.0 THz. Consequently, the THz signal reduced significantly after transmitting through the spinning disk, and the useful frequency range was below 0.45 THz.

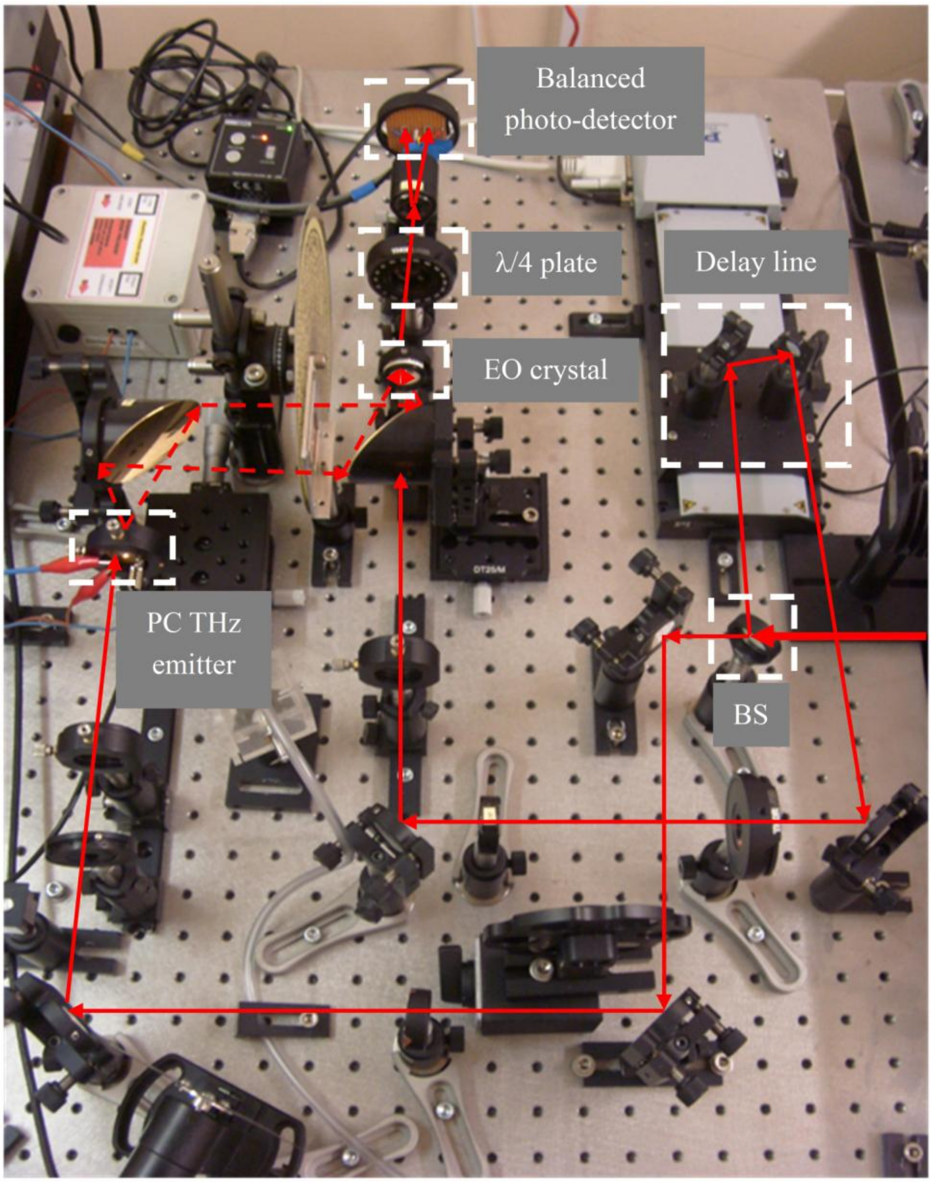

Figure. 5.13 Photo of the compressed THz time-domain (pulsed) spectroscopic imaging system. A photoconductive emitter is used for THz generation and an EO crystal is used for THz detection. (BS: beam splitter, PC THz emitter: photoconductive THz emitter, and EO: electro-optic).

5.4.2 Experimental Results

The stability of the femtosecond laser directly determines the SNR of THz time-domain (pulsed) imaging system. It depends on many environmental conditions such as electrical noise, room temperature and cooler temperature. It is necessary to monitor the power of laser during the whole experiment. As shown in Figure. 5.14 (a), during the starting period of time, the power of laser will continuously decease. We can calibrate the measured data by using the recorded power of laser which is as a function of time delay. Form Figure. 5.14 (b), to some extent, the difference between the simulated results and the experimental results can be reduced. Empirically, the power of laser will tend to be stable after a period of time. It is important to keep the environmental conditions stable because they directly determine the stability of femtosecond laser. The power of laser should be recorded during the whole experiment to monitor the system stability and for calibration if possible.

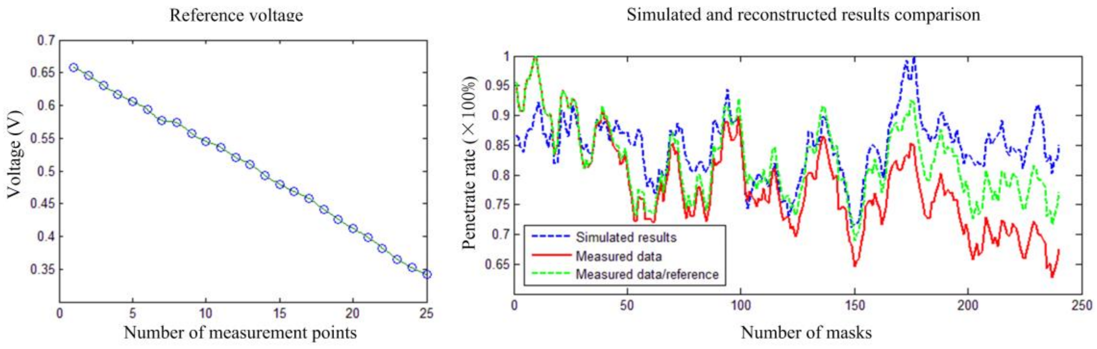

(a) (b)

Figure. 5.14 (a) Power of laser as a function of time delay. (b) Simulated and reconstructed results comparison. The curve in blue is the simulated results which is the ideal simulated data. The one in red is the measured data; and the one in green is the calibrated data using the data from (a).

Owing to the limited SNR, the rotation speed of the spinning disk was 5 deg/s and it took about 80 seconds to measure one THz image. For the same reason, we used 160 measurements for image reconstruction, as further increase in the measurement number decreases the quality of the reconstructed THz images. It was also reported in [2] that, even with full random binary operators, more measurements could add more artifacts for reconstructed THz images. Figure. 5.15 shows our experimental results for THz images of A, U, and H. Although the quality of reconstructed images is not as good as that in the IR experiments, all these characters are still recognizable. Also, compared with classical MMSE reconstruction, the TV-min optimization does not provide much visual improvement. This could be caused by the imperfection of the operator Φ in practical implementations. Fabrication error and misalignment of the spinning disk patterns as well as the nonuniform disk substrate could all contribute such noises in Φ. Nevertheless, our experimental results demonstrated the concept of using a continuously spinning disk approach for rapid compressive THz imaging.

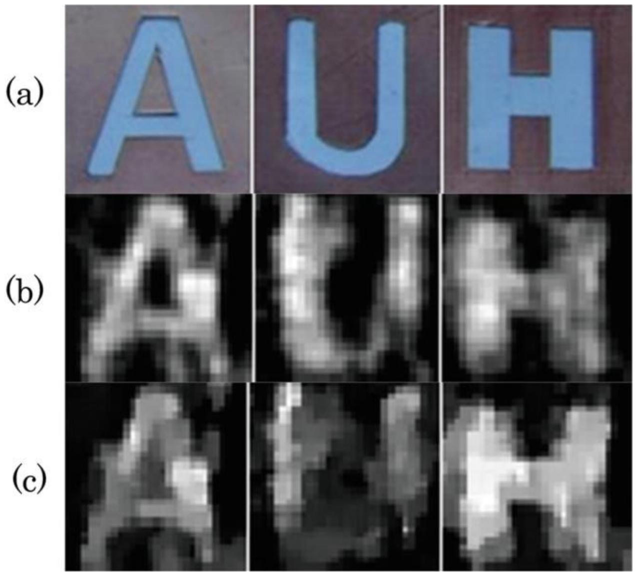

Figure. 5.15 (a) Photographs of the samples used in the THz imaging experiment, and their corresponding THz images reconstructed using (b) MMSE linear estimation and (c) the TV-min nonlinear reconstruction algorithm. Each image has 32×32 pixels and was reconstructed from 160 measurements [7].

Recall that, in [2, 3], a set of 10s or 100s of physical masks were used and it could take up to 30 min [3] to complete the THz image acquisition by switching 40 masks manually. Our spinning disk approach uses only one physical mask and less acquisition time. This simplifies the experimental setup, and allows the measurements to be done continuously. We noted that a THz spatial modulator could, in principle, be used for automatic CS-THz imaging [20]. However, the THz spatial modulator reported has only 4×4 pixels, limiting its practical imaging applications.

5.5 New Generation Spinning Disk

Considering that the PCB substrate material absorbs strongly THz radiation as well as the nonuniform disk substrate could contribute to such noises in Φ, currently, we designed a new generation spinning disk without substrate to minimize these noises. This new generation spinning disk is made of a 0.28-mm-thick steel plate. A number of 2.0-mm-diameter holes are drilled on this steel plate instead of 1.0 mm×1.0 mm squares which are fabricated on the PCB board. The schematic diagram of this new generation spinning disk is shown in Figure. 5.16. The corresponding sampling operator Φ could also be approximated as a Toeplitz block matrix. Using this new generation spinning disk, it can offer similar performance as that using our previous spinning disk, whereas minimizing the effect of the disk itself to the THz imaging system.

Figure. 5.16 Schematic diagram of new generation spinning disk which is made of a 20.0 mm×20.0 mm steel plate. The diameter of each holes drilled on the plate is 2.0 mm.

In order to illustrate the validation of this new generation spinning disk approach, we developed it in our IR experiments. Similar to the previous IR experiments, an IR LED and a photodiode were used as the light source and the detector, respectively.

The effective image window has a dimension of 33.4 mm×33.4 mm. In all the IR experiments, 1440 measurements were recorded to reconstruct the images of size 96×96 (9216 pixels in total), which means the sampling rate is around 15.6%.

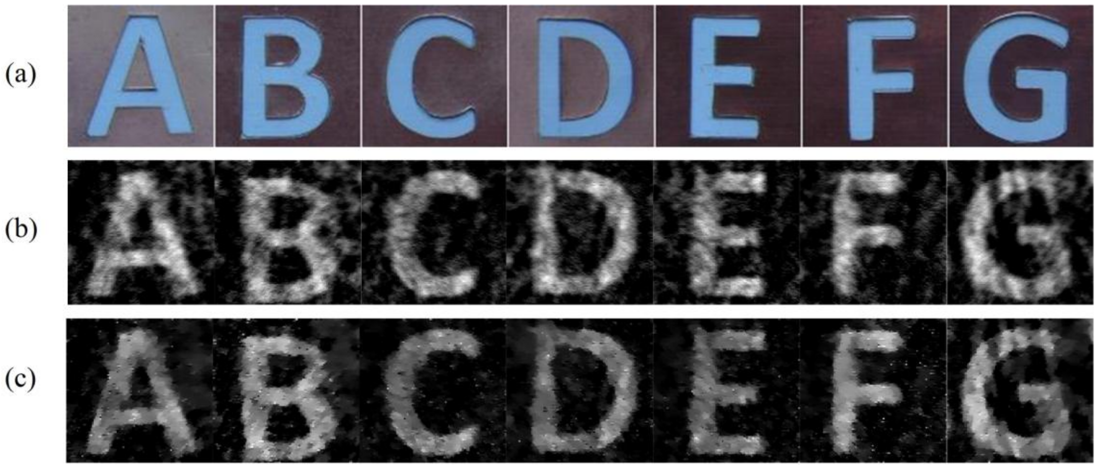

Figure. 5.17 (a) Photographs of the samples used in IR imaging experiment, and their corresponding IR images reconstructed using (b) MMSE linear estimation and (c) the TV-min nonlinear reconstruction algorithm. Each image has 96×96 pixels and was reconstructed from 1440 measurements.

Figure. 5.17 shows, as examples, the IR images of English characters A, B, C, D, E, F, and G reconstructed from 1440 measurements. One can see that, even with MMSE linear reconstruction, all the characters are visually recognizable. Similar to that using previous spinning disk, better quality images could be obtained using the TV-min optimization algorithm. For further quantitative analysis, we used four normal samples (in Figure. 5.18, from left to right) for reconstruction. For the extremely small patterns such as squares of size 1×1, 3×3 pixels and 1-pixel-width straight line, it is hard to recognize using either MMSE linear estimation or the TV-min nonlinear optimization. For the other patterns, even with MMSE linear estimation, the images are visually recognizable. Also, better quality images could be obtained using the TV-min optimization algorithm. Considering the diameter of each physical holes of this spinning disk is 2.0 mm, this new generation spinning disk provides a reasonable spatial resolution to reconstruct such small patterns whose size are only around 1.0 mm. As the physical holes cannot be fabricated as small as possible (diffraction need to be averted), such configuration of the new generator spinning disk has great potential to achieve a high resolution performance.

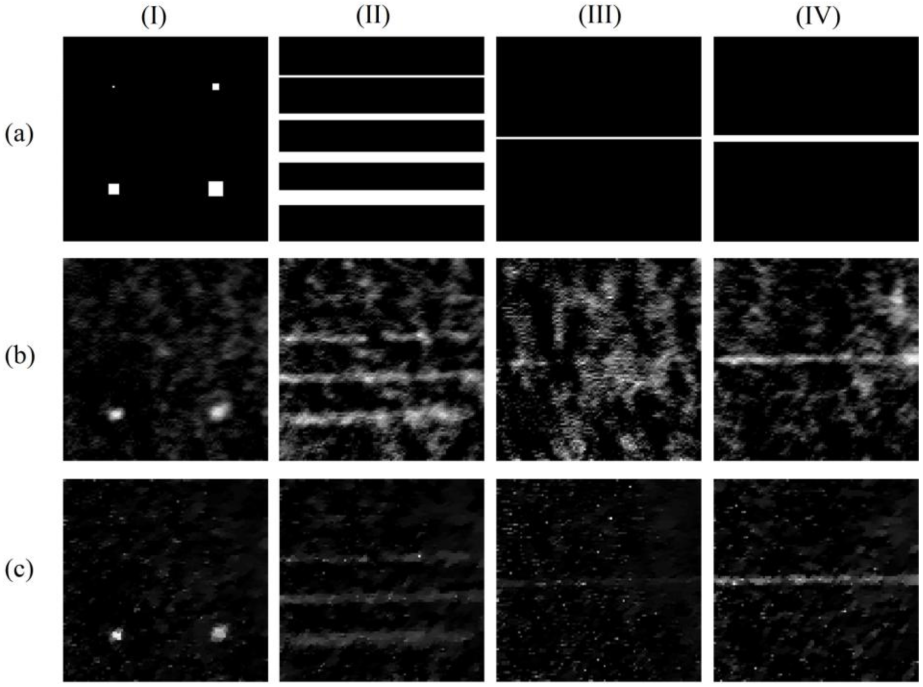

Figure. 5.18 (a) Normal sample images used in IR experiments, and their corresponding IR images reconstructed using (b) MMSE linear estimation and (c) the TV-min nonlinear reconstruction algorithm. Four samples from left to right: (I) Four squares of size 1×1, 3×3, 5×5, and 7×7 pixels. (II) Four straight lines whose widths are 1, 3, 5, and 7 pixels. (III) A straight line with 1-pixel-width. (IV) A straight line with 3-pixels-width. Each pixel equals to 0.33 mm in practice.

For the time being, this new generation spinning disk is only applied in the IR experimental implementation. From the proof of principle above, we believe that it is ready for our new generation spinning disk to be developed in the THz time-domain (pulsed) imaging system to minimize the noises in Φ. To some extent, the SNR could be become well once it is used in the future.

5.6 Discussion

Chan *et al*. reported the first THz-CS implementation in 2006, after that, we designed two different sampling operators and successfully demonstrate both of them in the practical THz time-domain (pulsed) systems. We summarized the current CS-THz systems using the physical masks (i.e., random projection on THz imaging) and present them in the Table. 5.1 as below:

Table. 5.1 Comparison for current CS-THz systems.

	Chan *et al.* [2]	Our work	
Number of masks	Hundreds of masks	40 optimized masks [3]	A single spinning disk configuration [5, 7]
Sampling operator Φ	Full random 0/1 pattern	Optimized 0/1 pattern	Random 0/1 block Toeplitz matrix
Sampling rate	0.2-0.4	0.1	0.16
Imaging resolution	32×32	20×20	32×32
Spectrum	0.15 THz	0.1 THz-2.0 THz	0.1 THz-0.45 THz

From this table, we can find that two different sampling operators were designed and used in our work. There are several improvements we achieved: firstly, we reduced the number of masks to 40 masks and one single spinning disk, rather than hundreds of masks. That means the imaging processing could be further speed up. Secondly, the sampling rates we achieved in both experiments are better than the one Chan *et al.* used. And Thirdly, we successfully reconstructed images within a THz range, rather than a specific frequency, so we can obtain more spectral information in the experiments.

For the 40 optimized masks, both the spatial and spectral characteristics of a sample have been reconstructed using a extremely low sampling rate. And for the spinning disk configuration, it allows an automatically and continuously high-speed compressive image acquisition. Both of these two methods have further developed the current CS-THz areas, ideal for real-time THz imaging applications.

5.7 Summary

In this chapter, we have reported the design and implementation of a continuously spinning disk based compressive imaging system. Such an approach offers the advantages of compact design, fast computation, and easy implementation with potential video-rate imaging speed.

As demonstrated here, the idea of the spinning-disk approach is applicable to both IR and THz time-domain imaging. In particular, for a 32 × 32 image, 240 measurements (i.e., around 24% sampling rate) are sufficient to get an IR image with reasonably good quality. For IR imaging, the imaging acquisition speed we achieved is about 1 image/s, mainly limited by the speed of the specific electric motor used in our experiment.

For THz imaging, owing to the limited SNR, the rotation speed of the spinning disk was 5 deg/s and it took about 80 seconds to measure one THz image. 160 measurements (about 16%) can reconstruct images with acceptable quality. Further increase in the measurement number decreases the quality of the reconstructed THz images. Even with full random binary operators, more measurements could add more artifacts for reconstructed THz images. Also, compared with classical MMSE reconstruction, the TV-min optimization does not provide much visual improvement. This could be caused by the imperfection of the operator Φ in practical implementations. Fabrication error and misalignment of the spinning disk patterns as well as the nonuniform disk substrate could all contribute such noises in Φ.

Considering that the PCB substrate material absorbs strongly THz radiation as well as the nonuniform disk substrate could contribute to such noises in Φ, currently, we designed a new generation spinning disk without substrate to minimize these noises.

Using such new generation spinning disk configuration, the THz image quality and acquisition speed could be significantly improved. From further quantitative analysis, the reconstructed IR results show that the new generation spinning disk can be used to recover high quality IR images and has great potential to achieve a high resolution performance. In the future, we look forward to seeing our new generation spinning disk to be developed in the THz time-domain (pulsed) imaging system to minimize the noises in Φ.

References:

[1] M. F. Duarte, M. A. Davenport, D. Takhar, J. N. Laska, K. F. Kelly and R. G. Baraniuk, "Single-pixel imaging via compressive sampling," *IEEE Sig. Proc. Mag.*, vol. 25, no. 2, pp. 83-91, 2008.

[2] W. L. Chan, K. Charan, D. Takhar, K. F. Kelly, R. G. Baraniuk, and D. M. Mittleman, "A single-pixel terahertz imaging system based on compressed sensing," *Appl. Phys. Lett.*, vol. 93, no. 12, 121105, 2008.

[3] Y. C. Shen, L. Gan, M. Stringer, A. Burnett, K. Tych, H. Shen, J. E. Cunningham, E. P. J. Parrott, J. A. Zeitler, L. F. Gladden, E. H. Linfield, and A. G. Davies, "Terahertz pulsed spectroscopic imaging using optimized binary masks," *Appl. Phys. Lett.*, 95, no. 23, 231112, 2009.

[4] A. Heidari and D. Saeedkia, "A 2D Camera Design with a Single-pixel Detector," *34th International Conference on infrared, millimeter, and terahertz waves*, vol. 1-2, 694-695, Pusan, South Korea, 2009.

[5] H. Shen, N. Newman, L. Gan, S. C. Zhong, Y. Huang and Y. C. Shen, "Compressed terahertz imaging system using a spin disk," *35th International Conference on infrared, millimeter, and terahertz waves*, Rome, Italy, 2010.

[6] G. Q. Xiao, T. R. Corle, and G. S. Kino, "Real-time confocal scanning optical microscope," *Appl. Phys. Lett*. vol. 53, no. 8, pp. 716-718, 1988.

[7] H. Shen, L. Gan, N. Newman, Y. Dong, C. Li, Y. Huang and Y. C. Shen, "Spinning disk for compressive imaging," *Opt. Lett.*, vol. 37, no. 1, pp. 46-48, 2012.

[8] W. U, Bajwa, J. D. Haupt, G. M. Raz, S. J. Wright, and R. D. Nowak, "Toeplitz-structured compressed sensing matrices," *In Proc. IEEE Workshop on Statistical Signal Processing*, pp. 294-298, Washington D. C., USA, 2007.

[9] F. Sebert, Y. M. Zou, L. Ying, "Toeplitz block matrices in compressed sensing and their applications in imaging," *in 5th International Conference on Information Technology and Application and Biomedicine*, pp. 47-50, Shenzhen, P. R. C., 2008.

[10] H. Rauhut, "Compressive sensing and structured random matrices," *Theoretical Foundations and Numerical Methods for Sparse Recovery*, vol. 9 of Radon Series Comp. Appl. Math., pp. 1-92. M. Fornasier, ed., deGruyter, 2010.

[11] J. Ke and M. A. Neifeld, "Optical architectures for compressive imaging," *Applied Optics*, vol. 46, no. 22, pp. 5293-5303, 2007.

[12] L. Gan, "Block compressed sensing of natural images," *in 15th International Conference on Digital Signal Processing*, IEEE, pp. 403–406, Cardiff, UK, 2007.

[13] E. J. Candès, J. Romberg, and T. Tao, "Robust uncertainty principles: Exact signal reconstruction from highly incomplete frequency information," *IEEE Trans. Inf. Theory*, vol. 52, no. 2, pp. 489 - 509, 2006.

[14] J. D. Haupt, W. U. Bajwa, G. M. Raz, and R. D. Nowak, "Toeplitz compressed sensing matrices with applications to sparse channel estimation," *IEEE Trans.*

Inf. Theory, vol. 56, no. 11, pp. 5862-5875, 2010.

[15] W. Yin, S. P. Morgan, J. Yang, and Y. Zhang, "Practical compressive sensing with Toeplitz and circulant matrices," Rice University CAAM Technical Report TR10-01, 2010.

[16] http://www.youtube.com/watch?v=WYsvAG5dWiM

[17] D. Donoho, "Compressed Sensing," *IEEE Trans. Inf. Theory*, vol. 52, vol. 4, pp. 1289-1306, 2006.

[18] D. H. Auston, K. P. Cheung, and P. R. Smith, "Picosecond photoconducting Hertzian dipoles," *Appl. Phys. Lett*., vol. 45, no. 3, pp. 284-286, 1984.

[19] Q. Wu and X. C. Zhang, "Free-space electro-optics sampling of mid-infrared pulses," *Appl. Phys. Lett.*, vol. 71, no. 10, pp. 1285-1286, 1997.

[20] W. L. Chan, H. T. Chen, A. J. Tayler, I. Brener, M. J. Cich, and D. M. Mittleman, "A spatial light modulator for terahertz beams," *Appl. Phys. Lett.*, vol. 94, no. 21, 213511, 2009.

Chapter 6

Three-Dimensional Reconstruction from Random/Incomplete Subsets of THz Data

To date, a number of random projection approaches on THz imaging based on CS have been proposed [1-6]. Such methods require data in a much lower sampling rate than the Nyquist sampling rate. Similar to that was reported in the previous chapters, in such systems, the THz beam passing the object is spatially modulated by a set of physical masks [2, 3] or a physical spinning disk [5, 6], and the resulting THz beam was then focused by using parabolic mirror onto the single pixel detector. A set of linear combinations of the object beam multiplied by the mask patterns were recorded for image reconstruction. Although the number of measurements is much smaller than that of the pixels to be reconstructed, such method using physical sampling operators is still time consuming and not that accurate. In [2, 3], such mechanical movement for changing one mask to another limit applications of CS-THz imaging, especially for high resolution imaging.

Currently, Cho *et al*. [7] reported fast THz reflection tomography using block-based CS [8]. It enables the THz tomography that reduces measurement time by apply the CS technique to the spatial domain. This proposed method does not require any additional spatial modulator or corresponding hardware and achieves fast acquisition and reconstruction without image degradation. It provides a general solution to the fast THz tomography. However, up to now, all these CS implementations have been performed on two-dimensional (2D) THz images.

In this chapter, we reported the compressive multidimensional imaging, especially the first implementation of direct three-dimensional (3D) compressive THz imaging by using random sampling [9]. Using such system, one can offer better quality of reconstructed images and faster acquisition than conventional frame-by-frame 2D approach, synchronously minimizing the hardware implementation. In section 6.1, similar to the idea of [7], a faster TV-min (so-called NESTA) [10] is used to frame-by-frame reconstruct 2D image. And in section 6.2, we demonstrated that only 5% of the 3D THz data is necessary to reconstruct all 3D THz images, thus has huge potential in significantly speeding up the THz measurements and reducing the required data storages.

6.1 Frame-by-Frame Inpainting

For the first step, a frame-by-frame 2D reconstruction is used here in order to demonstrate such compressive multidimensional imaging implementation without any physical spatial modulators, i.e., random sampling on THz imaging. In our work, random sampling is equivalent to under sampling. We keep a number of samples at random locations from a given set of data and leave the rest of the samples. Each observation measures one or more properties of observable bodies distinguished as independent objects or individuals. We can recover the signals using a small number of original data rather than the whole data set.

The results presented below are based on the THz data acquired across an area of 20.0 mm×22.0 mm using a TPIscan-1000 system (TeraView Ltd, Cambridge, U.K.), as shown in Figure. 6.1 (a), which covers a spectral range from 0.1 to 3.5 THz. The images have 268×120 pixels and at each pixel a THz waveform was recorded as function of time delay over a scan range of 4.0 mm. The sample used is a polythene pellet of a diameter of 25.0 mm. Inside the pellet there is a T-shaped plastic sheet which locates approximately 0.2 mm below the sample surface. In this section, for ease of computations we resized the images, using bicubic interpolation, so that the overall data size was 200×200×512. Figure. 6.1 (b) shows a 3D data cube extracted from the sample (40 layers started from 140th temporal band).

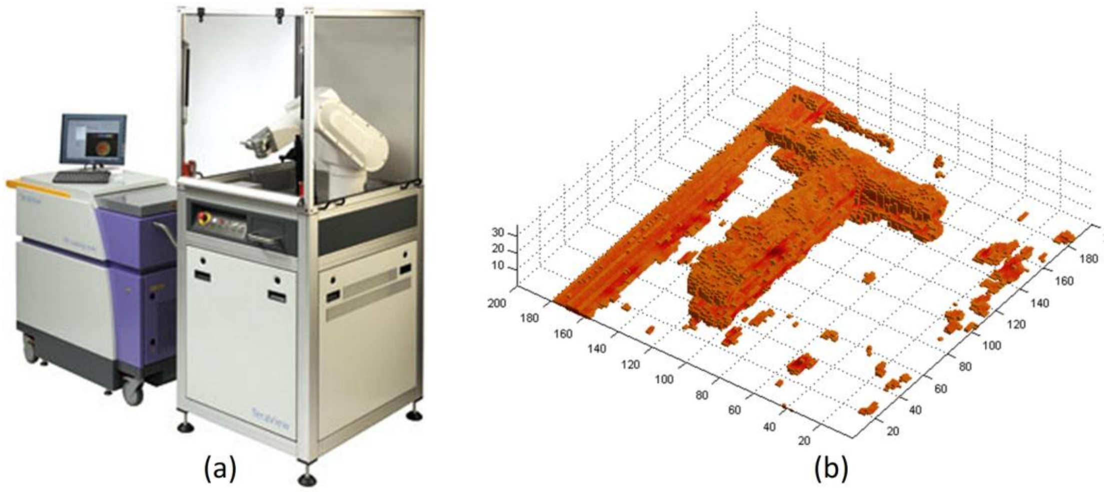

Figure. 6.1 (a) TPIscan-1000 system (TeraView Ltd, Cambridge, U.K.). (b) 3D data cube extracted from the sample (40 layers start from 140th temporal band).

A fast and robust first-order method for sparse recovery, NESTA, can solve the following TV-min problem which is used to recover 2D images [10]:

$$\min\|x\|_{TV} \quad s.t. \quad \|b-\Phi x\|_{l_2} \le \varepsilon . \tag{6.1}$$

In the spirit of Nesterov's smoothing technique, this method achieves a fast and accurate signal recovery by subtle averaging of sequences of iterates. Using such algorithm, a frame-by-frame reconstruction is presented, which means each 200×200 pixels cross-sectional THz image is recovered by using random sampling. Figure. 6.2 (b)-(f) shows the reconstruction results for one example THz image (166th temporal band) for different sampling rates at 10%, 15%, 20%, 25% and 30%, respectively. The dark areas correspond to the polythene pellet, and the bright areas correspond to the T-shaped plastic sheet. One can see that, all the reconstruction results are visually recognizable. According to the data from Figure. 6.2, Table. 6.1 show the mean square error (MSE) and signal-to-noise ratio (SNR) in dB for different observation rates. As expected, better quality images (better SNR) could be obtained by increasing the observation rate.

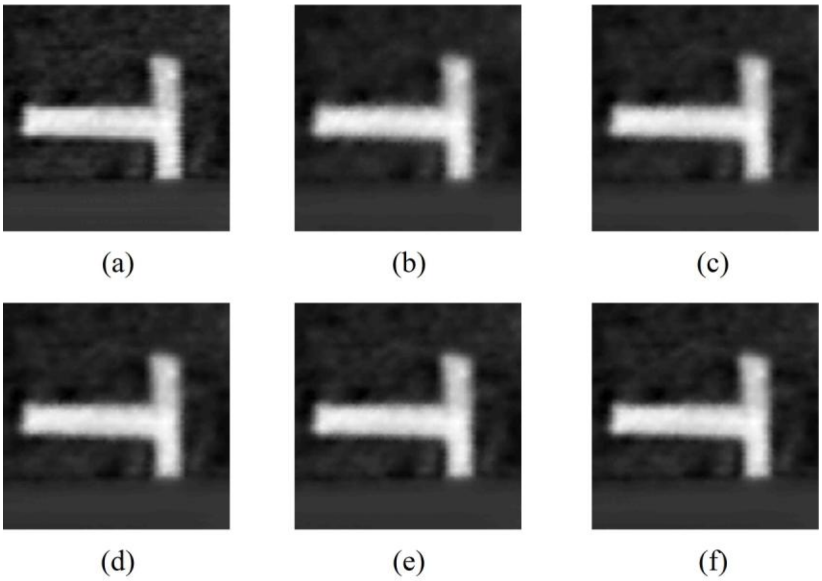

Figure. 6.2 (a) Original image. The corresponding reconstruction results using NESTA (b)-(f) for different sampling rates at 10%, 15%, 20%, 25% and 30%, respectively.

Table. 6.1 Mean square error (MSE) and signal-to-noise ratio (SNR) in dB, for different observation rates.

	10%	15%	20%	25%	30%
MSE	0.0865	0.0680	0.0605	0.0511	0.0457
SNR (dB)	21.01	23.00	24.84	25.85	26.98

A 3D reconstruction data cube extracted from the total reconstruction results is presented in Figure. 6.3. The T-shaped sample can be easily identified using NESTA at a 20% sampling rate. The reconstruction results can offer similar performance to the original image in Figure. 6.1 (b). Thus, this frame-by-frame reconstruction directly reduces the number of sampling points in the spatial domain without spatial modulation or transformation of the signal. It can substantially reduce the number of measurements and computational time without degrading the image quality.

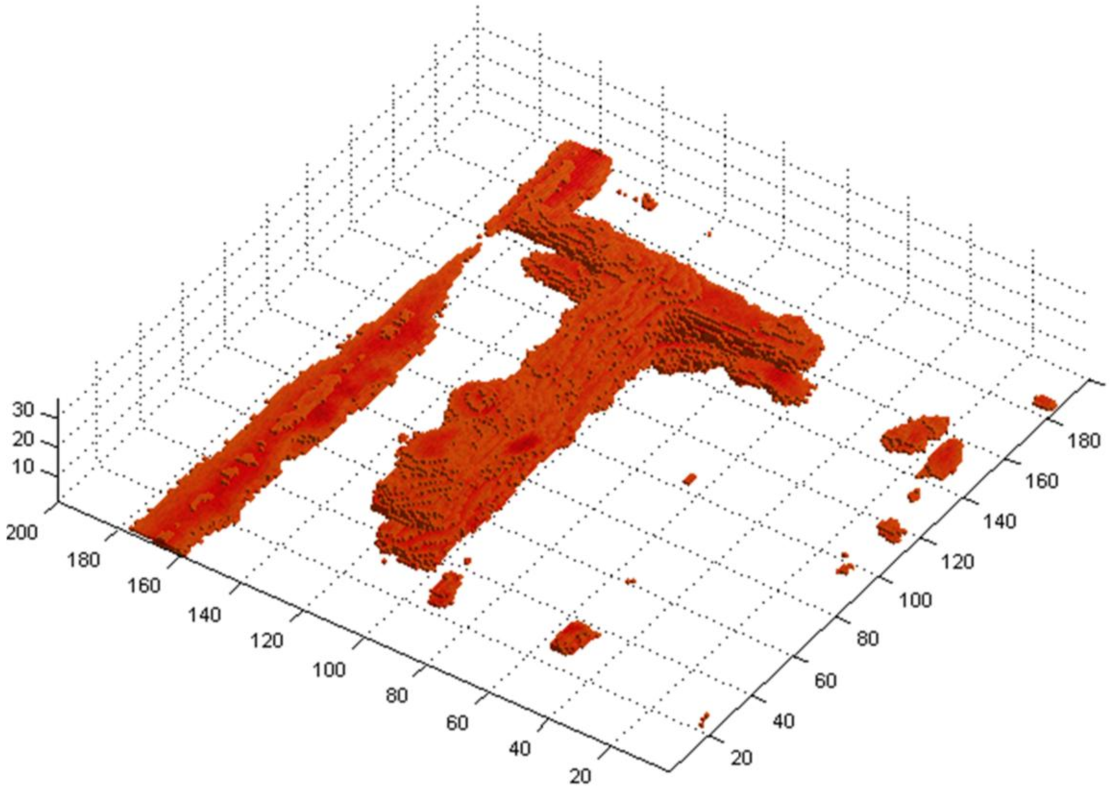

Figure. 6.3 3D reconstruction data cube extracted from the total reconstruction results (40 layers start from 140th temporal band) using NESTA for a 20% sampling rate.

6.2 3D joint Dictionary Learning and Recovery

Up to now, all the CS implementations have been performed on 2D THz images. In this section, we further developed the CS technique and reported the first implementation of direct 3D compressive THz imaging by using random sampling. Our main object is to exploit both spatial and spectral/temporal information for recovering the missing samples. To achieve this object, we first proposed to learn a spatio-spectral/temporal dictionary form a subset of available training data. Using this dictionary, we then jointly recovered the original data samples from a incomplete set of observations. Our experimental results confirm significant improvement over the existing methods.

Basically, CS was first developed for single vector problem, but later, its theoretical extension to the case of multiple vectors was studied in several works [11-14]. Distributed CS [14] and multiple measurement vector (MMV) [11] are two typical extensions. The idea in MMV is to jointly recovering the sparse vectors, while exploiting the common sparsity within the vectors. This can be the case where several measurement vectors are available over time/frequency. In most CS-based methods for multidimensional data, the data is treated as a number of independent single vectors (for example, 2D THz image inpainting in section 6.1). Although there are some works exploiting the correlation among different spectral/temporal bands [15-17], the advantages of joint sparse recovery have yet to be recovered. One of the contributions of this section is to develop an MMV-based method for reconstruction of multidimensional data from an incomplete set of observations.

On the other hand, there are some efforts to take advantages of learned dictionaries as sparsifying transforms, rather than fixed predefined bases [18-21]. The learned dictionaries are well-adapted to a particular class of data and can be considered as a powerful tool for sparsifying and denoising [22], or recovering signals from incomplete set of observations. In general, few works have been done for exploiting the spectral/temporal information for training the dictionaries [17, 19, 21] and more work can be carried out in this regard. In this section, a new strategy is proposed for learning a spatio-spectral dictionary from a subset of available 3D data. Instead of learning the dictionary individually for each spectral/temporal image, we proposed to consider several adjacent spectral/temporal images for learning the dictionary atoms. Thus, both spatial and spectral/temporal information are incorporated into the dictionary atoms. This dictionary, which is obtained from a subset of available data, will be used in the reconstruction stage. In this stage, we proposed an MMV-based technique to jointly recover the original data from an incomplete set of observations. To do this, we applied the proposed method to segments of consecutive smoothly varying images to achieve the corresponding sparse coefficients. The sparse coefficients were then multiplied with the dictionary to recover the original image pixels.

6.2.1 Dictionary Learning for 3D Training Data

In dictionary learning framework the aim is to find a dictionary that can sparsely represent a signal or image subject to availability of a set of training data. A dictionary is normally defined as an overcomplete matrix in which the columns (also called atoms) describe the features of the given training signals or images. Numerous applications can take advantages of learned dictionaries some of which are compression, denoising [22, 23], inpainting [23], and image separation [24, 25]. In contrast to traditional dictionary learning, which is defined for 1D and 2D signals, here we considered 3D data and attempted to simultaneously exploit both spatial and spectral/temporal information in designing the dictionary.

Supposed that the 3D data is composed of *N* adjacent images of size $n\times n$ which are spectrally/temporally related. Assumed further that we have only access to a subset of L_d adjacent images from this set denoting by $\tilde{X}\in R^{n\times n\times L_d}\equiv\{\tilde{X}_1,\tilde{X}_2,\ldots,\tilde{X}_{L_d}\}$. The superscript $(\tilde{\cdot})$ indicates the training data samples. The *i*-th datacube, extracted from $\tilde{X}$ was represented by $\tilde{x}_i=R_i(\tilde{X})$, where R_i is the datacube extraction operator. The datacube is of size of $r\times r\times L_d$, however, we represented it by a column vector of length r^2L_d throughout the subsequent discussions.

We extracted all datacubes with full spatial overlap [23] and defined the following minimization problem to find a sparsifying dictionary from the training vector $\{\tilde{x}_1,\tilde{x}_2,\ldots\}$:

$$\min_{D,\tilde{s}_i}\left\|\tilde{x}_i-D\tilde{s}_i\right\|_F^2 \quad s.t. \quad \left\|\tilde{s}_i\right\|_0\le\tau\,. \tag{6.2}$$

In the above expression, $D\in R^{r^2L_d\times k}$ is an overcomplete dictionary ($k>r^2L_d$), $\{\tilde{s}_i\}$

are sparse coefficients with scalar τ being the sparsity degree. Moreover, $\|\cdot\|_F$ denotes the Frobenius norm and $\|\cdot\|_0$ (ℓ_0-norm) counts the number of non-zeros. Problem (6.2) is not simultaneously convex in $(D, \{\tilde{s}_i\})$ and thus cannot be jointly minimized with respect to both variables. Instead, it should be minimized by considering one of the variables fixed at a time. Many "alternating minimization" approaches have been reported for (6.2) or its variations in the corresponding literature (see [22] and references therein). Here we used K-SVD [22] to solve (6.2). K-SVD is a generalization of K-means clustering and attempts to design a dictionary by alternatingly minimization of (6.2) using a sparse coding method followed by a Singular Value Decomposition (SVD). We noted that since the $\hat{x}_i$'s include both spatial and spectral/temporal information, the obtained dictionary atoms also have this property, and hence called spatio-spectral/temporal.

6.2.2 Joint Reconstruction from Incomplete Data

In the reconstruction stage, we assumed that an incomplete set of 3D observations is available and the aim is to recover the missing samples. By incomplete set we meant accessing to only few random samples of original data. These observations can be obtained as a result of random sampling which is a special case of compressed sensing. It is noteworthy to mention that although the work presented herein is designed for reconstruction from incomplete data it could be further extended for recovery from random projections (CS framework) in the future. Here, we proposed a joint recovery technique which utilizes the aforementioned learned spatio-spectral/temporal dictionary to reconstruct the original images. In what follows we mathematically described the problem and the method.

Consider a sampling operator, denoted by $M(\cdot)$, which operates simultaneously on a set of L_d adjacent images, and keeps only $m << n^2 L_d$ samples from *X*. These observed samples are then re-arranged into a column vector of length *m* denoted by $y = M(X)$, which presents an observation vector. A number of observation vectors can be generated in this way, for all other subsets, denoted by $\{y_1, y_2, \dots\}$. Now, assumed that we only have access to these vectors, in addition to the sampling operator $M(\cdot)$ and the dictionary *D*. Having these information, the aim is to recover the original images $\{X_j\}_{j=1}^N$.

The single image case of the aforementioned problem (i.e., $N = L_d = 1$) is called image inpainting in which the aim is to fill in the missing pixels of a corrupted image [22, 23]. Here, the situation is more complicated since we faced a sequence of related images which should not be treated independently. Our aim is to exploit the spectral/temporal dependency, as well as spatial dependency, while recovering the original data samples. Equipped with a learned spatio-spectral/temporal dictionary, we extended the method in [22, 23] for this purpose. Assuming that the unknown datacubes x_i have a sparse representation over the dictionary *D*, the following minimization problem can be defined for any subset of L_d spectral/temporal bands:

$$\min_{X, \{s_i\}} \lambda \|y - M(X)\|_2^2 + \sum_i \mu_i \|s_i\|_0 + \sum_i \|x_i - Ds_i\|_2^2 . \qquad (6.3)$$

This problem is not simultaneously convex in all variables and should be solved alternately. Consider for the moment that *X* (and correspondingly x_i) is fixed. Therefore, (6.3) is simplified to the following sparse coding problem:

$$\min_{\{s_i\}} \sum_i \mu_i \|s_i\|_0 + \sum_i \|x_i - Ds_i\|_2^2 . \qquad (6.4)$$

There exist different methods in the literature to solve the above problem, such as orthogonal matching pursuit (OMP) or focal underdetermined system solver (FOCUSS). All these methods are in the context of single measurement vector (SMV) and treat the datacubes, independently, rather than jointly. In many multidimensional applications, particular in THz imaging, the amplitudes of image sequences vary smoothly in spectral/temporal dimension, and also there may exist some correlations in this dimension. Hence, we proposed joint recovery of sparse coefficient to exploit this information. This is in-line with the spatio-spectral/temporal dictionary we proposed in the previous section. There are several sparse recovery approaches in the context of multiple measurement vector (MMV) such as MFOCUSS [11] or MOMP [12] which can be used here. The main goal in MMV is to simultaneously recover several sparse vectors having the same supports (locations of non-zeros). In order to utilize MMV for reconstruction of 3D data, the problem (6.4) should be modified.

Consider L_r consecutive subsets of *X*, i.e., $\{X_1, X_2, ...\}$. Assume further that *i*-th extracted datacube from all these subsets are vectorized and arranged into a $r^2 L_d \times L_r$ matrix $\Omega_i = [x_{i1}, x_{i2}, ..., x_{iL_r}]$. It is important to note that since each x_i, itself, is taken from a subset of L_d images, Ω_i involves the information from $L_d L_r$ bands. Correspondingly, we defined the $k \times L_r$ sparse coefficients matrix by $S_i = [s_{i1}, s_{i2}, ..., s_{iL_r}]$. Now instead of solving (6.4), we proposed to solve the following joint minimization problem:

$$\min_{\{S_i\}} \sum_i J^{(p)}(S_i) + \sum_i \|\Omega_i - DS_i\|_F^2 \, , \tag{6.5}$$

where:

$$J^{(p)}(S_i) = \sum_{z=1}^{k} (\|s_i^{[z]}\|_2)^p = \sum_{z=1}^{k} (\sum_{l=1}^{L_r} |s_{il}^{[z]}|^2)^{p/2} \, . \tag{6.6}$$

In the above expression, $0 \le p \le 1$, and $J^{(p)}(S_i)$ is the sparsity constraint which is applied jointly on the columns of S_i. Also, $s_i^{[z]}$ denotes the *z*-th row of S_i, and $s_{il}^{[z]}$ is the (z, l)-th entry of S_i. We considered MFOCUSS [11] algorithm for solving (6.5) which is an extension of FOCUSS algorithm to the MMV case.

After finding all the sparse coefficients, we returned to (6.3) and solved it with respect to X. This can be obtained by taking the gradient of (6.3) with respect to X and setting it to zero which leads to:

$$\hat{X} = (\lambda \mathrm{M}^{\mathrm{T}}\mathrm{M} + \sum_{\mathrm{i}} \mathrm{R}_{\mathrm{i}}^{\mathrm{T}}\mathrm{R}_{\mathrm{i}})^{-1}(\lambda \mathrm{M}^{\mathrm{T}} y + \sum_{i} \mathrm{R}_{\mathrm{i}}^{\mathrm{T}} D s_i), \tag{6.7}$$

where M and R_{i} are the matrix representation forms of $M(\cdot)$ and $R_i(\cdot)$ operators, respectively. Although the above expression seems computationally expensive at the first glance, it can be simply obtained in a pixel-wise fashion, particularly because the matrix to invert in (6.7) is diagonal [23, 25]. It is noteworthy to mention that the above estimation should be executed for all subsets which ultimately gives all spectral/temporal images $\hat{X}_1, \hat{X}_2, ..., \hat{X}_N$.

6.2.4 Results and Discussions

The results presented below are based on the THz data which is presented in section 6.1. In this section, for ease of computations we resized the images, using bicubic interpolation, so that the overall data size was 128×128×512. A subset of THz data was first selected for generating the training samples. We extracted the datacubes of size $r \times r \times L_d$, with r=8. The experiments were conducted for different L_d and L_r to evaluate the performance in each case. The THz images were of size 128×128 (i.e., n=128), and we considered full spatial overlap when extracting the datacubes. In addition, the number of dictionary atoms (length of each row of D) was k=1024.

We applied the proposed method to learn the overcomplete dictionary D in different trails with L_d =1, 2 and 4. Since we worked in the time domain, the obtained dictionary is called spatio-temporal. To examine the reconstruction performance, we assumed availability of only 5% of entire pixels. Such an incomplete set was generated, by zeroing 95% of samples uniformly at random locations. The same experiment was repeated for 10% pixel availability. We then applied the proposed joint reconstruction method (MFOCUSS with learned dictionary) to the incomplete observations for obtaining the sparse coefficients as well as the original THz images. This experiment was repeated for L_r =1, 2 and 3. The accuracy of recovery, in terms PSNR (peak signal to noise ratio) is tabulated in Table. 6.2. The effects of proposed spatio-temporal dictionary are clearly seen by comparing the results with the case of discrete cosine transform (DCT) dictionary. For example, the achieved PSNR for L_d =4, L_r =3, and 10% observations using the proposed method is almost 6.5 dB more than what is achieved with DCT dictionary.

Table. 6.2 Recovery accuracy (PSNR) in dB, for two cases of MFOCUSS with spatio-temporal dictionary (proposed), and MFOCUSS with DCT dictionary. The results are shown for different observation rates and different selection of L_d and L_r [9].

			PSNR (dB)	
L_d	L_r	Observation rate	Proposed	MFOCUSS with DCT
1	1	5%	16.73	13.10
		10%	18.11	14.18
2	1	5%	18.13	13.29
		10%	19.41	14.49
4	1	5%	18.54	13.62
		10%	23.12	15.71
4	2	5%	21.33	14.24
		10%	24.12	16.10
4	3	5%	22.39	15.60
		10%	24.91	18.33

Furthermore, Table. 6.2 shows that higher PSNR is achieved when more number of segments is used for both learning the dictionary and image reconstruction. For example, the achieve PSNR for L_d =4, L_r =3, and 10% observations is almost 7 dB more than what is achieved when L_d =1, L_r =1 using the proposed method. This behavior shows the significance of using MMV versus SMV. Note that the choice of L_d =1, L_r =1 is equivalent to SMV with no exploitation of temporal information.

For comparison with other SMV-based algorithms we also show in Table. 6.3 the accuracy of recovery when the proposed method, TV-min [10] and OMP [26] were used with different observation rates. The results of the proposed method in Table. 6.3 is for L_d =4, L_r =2. As expected, Table. 6.3 shows the superiority of the proposed method over those methods relying on single vector reconstruction.

Table. 6.3 Recovery accuracy (PSNR) in dB, for different methods. We used $L_d = 4$ and $L_r = 2$ for the proposed method [9].

Method	Observation rate					
	5%	10%	15%	20%	25%	30%
TV-min	14.92	17.97	19.40	21.70	22.10	22.55
OMP	14.58	19.03	21.89	23.50	24.09	25.06
Proposed	21.33	24.12	24.91	25.99	26.11	27.04

In addition, the reconstruction results for one example THz image (152th temporal band) have been shown in Figure. 6.4. As seen from Figure. 6.4, the proposed method was able to reconstruct the image with highest PSNR among other methods. Comparing the results in this figure reveals the advantages of spatio-temporal dictionary learning and also joint sparse recovery over the conventional image reconstruction approaches.

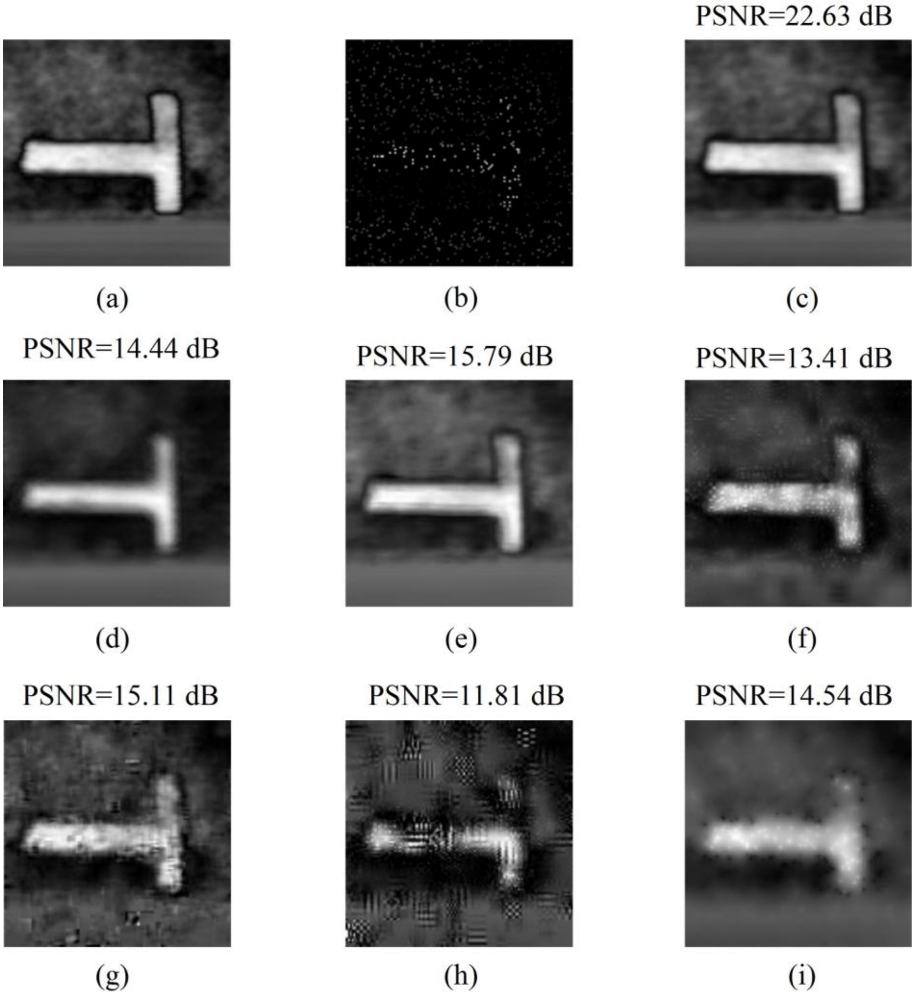

Figure. 6.4 (a) Original image, (b) incomplete image, keeping only 5% of pixels. Reconstruction results using (c) proposed method (MFOCUSS with learned dictionary), (d) MFOCUSS with DCT dictionary, (e) FOCUSS with learned dictionary, (f) FOCUSS with DCT dictionary, (g) OMP with learned dictionary, (h) OMP with DCT dictionary, and (i) TV-min inpainting [9].

6.5 Summary

In this chapter, a new fast tomography method with conventional THz imaging system is proposed using under-sampled data in the spatial domain. After a frame-by-frame 2D reconstruction has been reported by NESTA, a new spatio-spectral/temporal dictionary learning is presented for 3D data. The proposed method learns a sparsifying dictionary from a subset of available data. The key point is to simultaneously use several adjacent images for training, thus, exploiting both spatial and spectral/temporal information through the dictionary atoms. Following this idea, we proposed an MMV-based method for joint recovery of sparse coefficients from an incomplete set of observations. The sparse coefficients and the dictionary, together, were later used to recover the missing samples. Our results on THz data confirmed the significant improvement we achieved compared with existing approaches. This proposed method does not require any additional hardware and achieves fast acquisition and reconstruction. It provides a general solution to the fast spatial-domain THz imaging and has huge potential in significantly speeding up the THz measurements and reducing the required data storages.

References:

[1] M. F. Duarte, M. A. Davenport, D. Takhar, J. N. Laska, K. F. Kelly and R. G. Baraniuk, "Single-pixel imaging via compressive sampling," *IEEE Sig. Proc. Mag.*, vol. 25, no. 2, pp. 83-91, 2008.

[2] W. L. Chan, K. Charan, D. Takhar, K. F. Kelly, R. G. Baraniuk, and D. M. Mittleman, "A single-pixel terahertz imaging system based on compressed sensing," *Appl. Phys. Lett.*, vol. 93, no. 12, 121105, 2008.

[3] Y. C. Shen, L. Gan, M. Stringer, A. Burnett, K. Tych, H. Shen, J. E. Cunningham, E. P. J. Parrott, J. A. Zeitler, L. F. Gladden, E. H. Linfield, and A. G. Davies, "Terahertz pulsed spectroscopic imaging using optimized binary masks," *Appl. Phys. Lett.*, 95, no. 23, 231112, 2009.

[4] A. Heidari and D. Saeedkia, "A 2D Camera Design with a Single-pixel Detector," *34th International Conference on infrared, millimeter, and terahertz waves*, vol. 1-2, 694-695, Pusan, South Korea, 2009.

[5] H. Shen, N. Newman, L. Gan, S. C. Zhong, Y. Huang and Y. C. Shen, "Compressed terahertz imaging system using a spin disk," *35th International Conference on infrared, millimeter, and terahertz waves*, Rome, Italy, 2010.

[6] H. Shen, L. Gan, N. Newman, Y. Dong, C. Li, Y. Huang and Y. C. Shen, "Spinning disk for compressive imaging," *Opt. Lett.*, vol. 37, no. 1, pp. 46-48, 2012.

[7] S. H. Cho, S. H, Lee, C. N. Gung, S. J. Oh, J. H. Son, H. Park, and C. B. Ahn, "Fast terahertz reflection tomography using block-based compressed sensing," *Opt. Express*, vol. 19, no. 17, pp. 16401-16409, 2011.

[8] L. Gan, "Block compressed sensing of natural images," *in 15th International Conference on Digital Signal Processing*, IEEE, pp. 403–406, Cardiff, UK, 2007.

[9] H. Shen, V. Abolghasemi, L. Gan and Y. C. Shen, "Compressive three-dimensional (3D) terahertz imaging," *accepted by Institute of Physics' conference in optics and photonics, Photon12*, 2012.

[10] S. Becker, J. Bobin, and E. J. Candès, "NESTA: a fast and accurate first-order method for sparse recovery," SIAM J. on Imag. Sci., vol. 4, no. 1, pp. 1-39, 2011.

[11] S. F. Cotter, B. D. Rao, K. Engan, and K. Kreutz-Delgado, "Sparse solutions to linear inverse problems with multiple measurement vectors," *IEEE Trans. on Signal Processing*, vol. 53, no. 7, pp. 2477-2488, 2005.

[12] S. F. Cotter, J. Adler, R. D. Rao, and K. Kreutz-Delgado, "Forward sequential algorithms for best basis selection," *IEEE Proc. on Vision, Image and Signal Processing*, vol. 146, no. 5, pp. 235-244, 1999.

[13] Z. Zhang and B. D. Rao, "Sparse signal recovery with temporally correlated source vectors using sparse bayesian learning," IEEE Journal of Selected Topics in Signal Processing, vol. 5, no. 5, pp. 912-926, 2011.

[14] M. F. Duarte, S. Sarvotham, D. Baron, M. B. Wakin, and R. G. Baraniuk,

"Distributed compressed sensing of jointly sparse signals," *39th Asilomar Conf. Signals, Systems, and Computers*, pp. 1537-1541, Pacific Grove, CA, 2005.

[15] T. T. Do, Y. Chen, D. T. Nguyen, N. Nguyen, L. Gan, and T. D. Tran, "Distributed compressed video sensing," *16th IEEE International Conf. on Image Processing - ICIP*, vols. 1-6, pp. 1381-1384, Cairo, Egypt, 2009.

[16] M. F. Duarte and R. G. Baraniuk, "Kronecker compressive sensing," *IEEE Trans. on Image Processing*, vol. 21, no. 2, pp. 494-504, 2012.

[17] W. Yin and S. Valiollahzadeh, "Hyperspectral data reconstruction combining spatial and spectral sparsity," Tech. Rep., Rice University.

[18] A. S. Charles, B. A. Olshausen, and C. J. Rozell, "Learning sparse codes for hyperspectral imagery," *IEEE Journal of Selected Topics in Signal Processing*, vol. 5, no. 5, pp. 963-978, 2011.

[19] Z. Xing, M. Zhou, A. Castrodad, G. Sapiro, and L. Carin, "Dictionary learning for noisy and incomplete hyperspectral images," *SIAM Journal on Imaging Sciences*, vol. 5, no. 1, pp. 33-56, 2012.

[20] Y. Moudden, J. Bobin, J-L. Starck, and J. Fadili, "Dictionary learning with spatio-spectral sparsity constraints," in Signal Processing with Adaptive Sparse Structured Representations - SPARS’09, Saint Malo, France, 2009.

[21] J. B. Greer, "Sparse demixing of hyperspectral images," *IEEE Trans. on Image Processing*, vol. 21, no. 1, pp. 219-228, 2012.

[22] M. Aharon, M. Elad, and A. Bruckstein, "K-SVD: An algorithm for designing overcomplete dictionaries for sparse representation," *IEEE Trans. on Signal Processing*, vol. 54, no. 11, pp. 4311-4322, 2006.

[23] M. Elad, "Sparse and redundant representations: from theory to applications in signal and image processing," Springer, 2010.

[24] V. Abolghasemi, S. Ferdowsi, B. Makkiabadi, and S. Sanei, "Adaptive fusion of dictionary learning and multichannel BSS," *in IEEE International Conf. on Acoustics, Speech, and Signal Processing–ICASSP’12*, 2012.

[25] V. Abolghasemi, S. Ferdowsi, and S. Sanei, "Blind separation of image sources via adaptive dictionary learning," *IEEE Trans. on Image Processing*, 2012.

[26] J. A. Tropp and A. C. Gilbert, "Signal recovery from random measurements via orthogonal matching pursuit," *IEEE Trans. Inf. Theory*, vol. 53, no. 12, pp. 4655-4666, 2007.

Chapter 7

Conclusions and Future Work

7.1 Conclusions

In this research, we developed a faster and more efficient THz imaging system based on the concept of CS. Both the random projection and the random sampling methods for compressive THz imaging were investigated. On the hardware side, we implemented two CS-THz systems based on random projection: one used a set of independent optimized masks and the other employed a single spinning disk. Compared with conventional TPI, these two CS THz imaging systems require no raster scanning of the object and fewer measurements. For random sampling, we demonstrated a 3D joint reconstruction of THz images from random/incomplete subsets of THz data.

The random projection approach was used to reconstruct THz images from the synthetic and real-world THz data. The MMSE linear estimation was used as the reconstruction algorithm and the simulated results were subsequently reconstructed and obtained. Some key aspects of compressive THz imaging, including the effect of number of measurements, the effect of signal-to-noise ratio (SNR), and the limit of spatial resolution etc., have been investigated. The simulation results demonstrated that CS can be successfully used in THz imaging systems and has great potential on real-time THz imaging system because its use can dramatically reduce the number of measurements needed in such systems.

Two different CS-THz systems were developed based on the random projection method. One of these is a THz time-domain (pulsed) spectroscopic imaging system using a set of independent optimized masks. A single-point THz detector, together with a set of 40 optimized 2D binary masks, was used to measure the THz waveform transmitted through a sample. THz time- and frequency-domain images of the sample comprising 20×20 pixels were subsequently reconstructed. We demonstrated the first CS-THz system which can obtain both the spatial distribution and the spectral characteristics of a sample. The binary masks are optimized to approximate the Karhunen-Loeve transform (KLT). Using such masks, the achieved sampling rate is extremely small, only 10% of the pixels are required for reconstructing an image.

In order to further speed up the image acquisition and reconstruction process, another hardware implementation - a single rotating mask (i.e., a spinning disk) with random binary patterns - was used in TPI systems. This demonstrated that a 32×32 pixel image could be obtained from 160 to 240 measurements. This spinning disk configuration allows the use of an electric motor to rotate the spinning disk, thus enabling the experiment to be performed automatically and continuously. We reported the first, to the best of our knowledge, experimental implementation of a spinning disk configuration for high speed compressive THz image acquisition. Also, a second generation spinning disk without substrate was developed to minimize the effect of the disk itself on the THz imaging system. Compared with the current spinning disk-based THz imaging system, such a new generation spinning disk has potential to achieving faster and more efficient THz imaging.

We developed a three-dimensional (3D) reconstruction method in order to reconstruct THz images from random/incomplete subsets of THz data. Such a random sampling approach also provides a fast THz imaging application, which can minimize the current THz imaging hardware implementation. We first proposed to learn a spatio-spectral/temporal dictionary from a subset of available training data. Using this dictionary, the THz images can be then jointly recovered from an incomplete set of observations. Such a method offers fewer computations and greater SNRs than any other algorithms.

7.2 Future Work

The immediate future work following up the work described in this thesis is to develop the second generation spinning disk to THz imaging systems. Currently, the spinning disk configuration has been proved to achieve a video-rate performance in the NIR range. However, owing to the limits of SNR, the rotation speed of the spinning disk was five deg/s and it took about 80 seconds to measure one THz image. It is projected that, after testing the performance of the second generation spinning disk, it can be used in the TPI to further improve the SNR. Hopefully, using such new generation configuration, we can achieve real-time THz imaging application, synchronously characterizing the spectral information of the desired sample.

After that, for the random projection approach, we will focus on camera calibration, derivation of theoretical performance bounds, fast reconstruction algorithms and high-resolution imaging. The design of other types of efficient THz modulator based on different constructions of sensing matrix is another research area. Also, considering both the reconstructed IR and THz results are good, such an approach can be applied to other frequencies, not only in THz range, for an efficient imaging implementation.

For the random sampling method, several interesting future plans can be imagined for this work. First, studying the effects of applying the proposed method to other types of multidimensional data. Second, extension to a CS regime and recovery from random projections. Furthermore, we applied classical K-SVD with OMP to learn the spatio-spectral dictionaries; however, we are going to study the effects of using MFOCUSS or MOMP for the dictionary learning stage of the proposed method. Basically, such an approach proposes a novel way to reconstruct a THz image without any physical modification to the current THz systems; and also to directly reduce the number of measurements and amount of storage required. In the future, we hope to further develop the joint recovery algorithms, and integrate them with the current THz systems to achieve an on-line CS-THz system.